

**UCLA**

**UCLA Electronic Theses and Dissertations**

**Title**

Study of Fundamental Plasma Properties in an Inductively Coupled Plasma Device

**Permalink**

<https://escholarship.org/uc/item/0gz1m9mh>

**Author**

Han, Jia

**Publication Date**

2020

Peer reviewed|Thesis/dissertation

UNIVERSITY OF CALIFORNIA  
Los Angeles

Study of Fundamental Plasma Properties in an Inductively Coupled Plasma Device

A dissertation submitted in partial satisfaction  
of the requirements for the degree  
Doctor of Philosophy in Physics

by

Jia Han

2020

© Copyright by  
Jia Han  
2020

## ABSTRACT OF THE DISSERTATION

Study of Fundamental Plasma Properties in an Inductively Coupled Plasma Device

by

Jia Han

Doctor of Philosophy in Physics

University of California, Los Angeles, 2020

Professor Walter Gekelman, Chair

Radio frequency inductively coupled plasma sources are widely used in low temperature industrial processing. Recent computer simulations and experiments indicate significant improvement in processing results with the use of pulsed plasmas. This thesis reports simultaneous measurements of nearly all plasma and electromagnetic properties of an ICP in three-dimensions under pulsed operation.

The plasma density profile is measured by rf compensated Langmuir probes, hairpin probes, and a 60 GHz microwave interferometer. Line integrated electron density measured from these three very distinct diagnostic techniques (interferometer, Langmuir probe, Hairpin resonator probe) shows agreement. Three-axis Bdot probes are used to measure the magnetic field. Inductive plasma current is calculated from measured magnetic field using Ampere's law. With the observed cylindrical symmetry, the electromagnetic electric field is derived from Bdot data using Faraday's law. The above field and current are used to calculate the inductive power and Poynting vector.

A side by side comparison in pulsed plasma operation is presented for two industry-relevant neutral pressures (5 mTorr, 25 mTorr). Distinct plasma evolution is observed with the two cases. The observations from the experiment are explained with the help of a simple lumped element circuit model.

The dissertation of Jia Han is approved.

Troy Carter

George Morales

Christopher Niemann

Walter Gekelman, Committee Chair

University of California, Los Angeles

2020

# TABLE OF CONTENTS

<b>List of Figures</b> . . . . .	<b>vi</b>
<b>List of Tables</b> . . . . .	<b>xiv</b>
<b>Acknowledgments</b> . . . . .	<b>xv</b>
<b>Curriculum Vitae</b> . . . . .	<b>xvi</b>
<b>1 Introduction</b> . . . . .	<b>1</b>
1.1 Inductively Coupled Plasmas . . . . .	3
1.2 Pulsed operation . . . . .	5
1.3 Motivation . . . . .	7
<b>2 Experimental setup and Diagnostics</b> . . . . .	<b>8</b>
2.1 Experimental chamber . . . . .	8
2.2 Langmuir probe . . . . .	11
2.2.1 Langmuir probe theory and analysis . . . . .	11
2.2.2 Langmuir probe in RF plasma . . . . .	15
2.2.3 Sheath and plasma perturbation . . . . .	18
2.2.4 surface contamination . . . . .	19
2.3 Emissive probe . . . . .	20
2.4 Hairpin resonator probe . . . . .	21
2.5 Microwave interferometer . . . . .	22
2.6 Magnetic probe (B-dot) . . . . .	24
2.7 Data acquisition . . . . .	27

<b>3</b>	<b>Results and Discussion</b>	<b>30</b>
3.1	Steady state Argon plasma	30
3.2	Pulsed Argon plasma	40
3.3	E-H transition	51
3.4	Lumped element model	55
<b>4</b>	<b>Conclusion</b>	<b>62</b>
<b>A</b>	<b>RF compensation circuit for Langmuir probe</b>	<b>66</b>
<b>B</b>	<b>Hairpin probe analysis</b>	<b>71</b>
<b>C</b>	<b>Bdot probe construction</b>	<b>74</b>
<b>D</b>	<b>Effect of feedstock gas flow rate</b>	<b>77</b>
	<b>References</b>	<b>80</b>

## LIST OF FIGURES

2.1	Schematic of the experimental chamber from (a) side view and (b) top view. Photo of (c) the 3D probe drive and (d) the chamber. The probe is capable of rotation and translation with the ball valve as the pivot point, allowing 3D measurement in the chamber. The wafer is electrostatically clamped to the top of the chuck assembly, where RF bias can be applied. Gas is exhausted through a gap between the chuck assembly and the chamber wall. . . . .	8
2.2	Langmuir probe IV characteristic with RF oscillation on sweep voltage $V_s$ . . . .	16
2.3	Langmuir probe electron current vs time measured at the center of the chamber. Plasma operating at Ar 25 mTorr. Probe biased at +25 V during on-time and -50 V during off-time. Positive bias results in collecting electrons, so the active glow phase is during the more negative sections. (a) Probe bias on for 7.5 ms and off for 900 ms. Plasma is pulsed at 1 kHz. The collected electron saturation current decreases over time. (b) Probe bias on for 1.5 ms. The delay intervals listed on the legend are between the re-application of the probe bias - too fast results in defective measurements. . . . .	17
2.4	(a) Schematic of the microwave circuit and beam passing the plasma (b) Photo of the single horn homodyne interferometer. The beam travels through the center of the plasma and reflects back to the horn from a corner reflector. . . . .	22
2.5	Example of (a) Input to the frequency swept Gunn Diode. (b) Original (blue) and Gaussian smoothed (orange) mixer output. . . . .	23
2.6	Examples of three components of $\vec{B}$ and $\vec{J}$ as a function of time at two heights under the antenna. Panel (c) is derived from (a) and its neighboring points by taking the curl using finite difference method. Similarly for panel (b) and (d). .	26

2.7	Current density versus time at two heights in the machine. The radial position is the same as Fig. 2.6. The solid lines are magnitudes $ \vec{J} $ computed using volumetric $B_x, B_y, B_z$ . The dashed lines are computed from $B_r$ and $B_z$ on the $\hat{z}$ line. . . . .	27
3.1	Time-averaged plasma potential (shown as flood contours) obtained with an emissive probe and the associated space charge electric field vectors. (a) RZ-plane where $r=0$ corresponds to the center of the wafer. (b). XY-plane parallel to the wafer at an intermediate height, $z = 8$ cm. The purple regions are missing data from probe movement limitation. . . . .	31
3.2	Measurements of electron density evaluated from ion saturation current calibrated with interferometer. a) Density as a function of height above the wafer at different radii. b) Density as a function of radius at different heights. c) Density on half of an RZ-plane. d) Three-dimensional density shown as nested isosurfaces. The wafer, antenna, and ceramic top are drawn to scale to guide the eye. . . . .	32
3.3	2D vector plot computed from Bdot data at maximum antenna current. (a) $\vec{B}$ on RZ-plane at the center of the machine. The fiducial arrow represents a magnitude of 1 G. (b) $\vec{J}$ corresponding to above $\vec{B}$ on XY-plane 8 cm above the wafer. . . . .	33
3.4	(a, b, c) $\tilde{J}_\phi$ and (d, e, f) $\tilde{E}_\phi$ calculated from induced magnetic field. The current on the antenna coils has a peak value of 35 A. The three rows from top to bottom correspond to $t/T_{RF} = 0, 0.125, 0.25$ , respectively. The red and blue colormap correspond to current flowing or electric field pointing into or out of the page. . . . .	34
3.5	(a) Electron neutral (e-n) collision frequency ( $f_{en} = \nu_{en}/2\pi$ ) and (b) mean free path vs electron temperature for pressures of interest. The dashed line on panel (a) is the driving frequency (2 MHz) drawn as reference. . . . .	36

3.6	Inductive power derived from the measured B field. The power shown here is time averaged over one RF cycle. (a) Line-out along z direction taken through the location of maximum power absorption for different pressures: 10 mT (blue), 50 mT (yellow), and 100 mT (green). As pressure increases, the power deposition gathers even closer around the antenna. (b) 2D contour of power density with the center of the wafer at $r = 0$ and $z = 0$ . (c) 3D iso-surface of power (red). This frame shows a snapshot at the time when power absorption is maximum. The vectors are electric field at three different height above the wafer ( $z = 6, 9, 14$ cm).	37
3.7	Contours of plasma density (red), shaded contours of inductive power, Poynting vector (white arrows) and the plasma current density (grey contours). Values are shown for an Ar pressure of 10 mTorr and generator power of 300 W.	39
3.8	Examples of the two types of density profile as 3D iso-surfaces. Although the two plots in particular are extracted from an $I_{isat}$ during the plasma breakdown, panel (a) can be acquired at low power and/or high pressure CW operation, and panel (b) at other CW conditions. The green and red iso-surface can therefore have any density value between $10^8 - 10^{12}cm^{-3}$ depending on the situation.	40
3.9	Antenna power, visible light and plasma density measured by the interferometer at (a) initial breakdown and (b) final shut off of the source. The blue curve corresponds to the vertical axis on the left and the red curve reads that on the right. The visible light signal is acquired with a diode.	42

3.10	Time evolution of plasma density (solid lines) for one pulse cycle measured by the interferometer, where blue corresponds to the 5 mTorr case, and orange corresponds to 25 mTorr. The fainter background shows the antenna current oscillating at 2 MHz for both pressures. The dashed lines are RF power input at the antenna. In this case, the antenna currents were set to be approximately equal for both pressures, which results in slight differences of RF voltage and power. Solid lines are $n_e$ measured by the interferometer normalized to unity at their maximum. The peak densities for 5 and 25 mTorr are $4.6 \times 10^{10} cm^{-3}$ and $2.85 \times 10^{11} cm^{-3}$ , respectively. . . . .	43
3.11	Electron density evolution for one plasma cycle from three different diagnostics. The plasma is pulsed at 1 kHz with 50% duty cycle, with 300 W peak power and sustained in 25 mTorr Argon. The probe results are line averaged through the center of the machine. . . . .	44
3.12	Langmuir probe measurement results at the center of the chamber for 25 mTorr. $n_e$ in panel (a) and $T_e$ in panel (b) are derived from the EEDF, and $V_p$ in panel (c) is defined as the maximum of $\frac{dI}{dV}$ . Noise in these signals is primarily due to uncertainties in determining the precise plasma potential in the stepped Langmuir probe characteristic. . . . .	45
3.13	First derivative of the Langmuir probe IV characteristic (proportional to EEDF) in center of the chamber at 25 mTorr. The traces are $8 \mu s$ apart. . . . .	46
3.14	Electron density in the afterglow measured by a hairpin probe. RF on the antenna begins to drop at $t = 500 \mu s$ . (a)-(d) are XY-plane ( $z = 12$ cm) contours taken at 5 mTorr. (e)-(f) are lineouts taken at 5 mTorr and 25 mTorr respectively. . . . .	47

3.15	Electron density in the active-glow measured by a hairpin probe at $z = 12$ cm with 5 mTorr (a, b) and 25 mTorr (c, d) fill pressure. The peak antenna power is 300 W for (a, c) and 100 W for (b, d). The data points are fitted to guide the eye. In panel (b) the $t = 0$ profile is missing because the hairpin probe was unable to resolve the density structure well. In panel (a, b), the line-out at $75 \mu s$ is at the time of the most hollow density profile, and in panel (c, d) $100 \mu s$ corresponds to the minimum density over the whole pulse (instead of $t = 0$ ). . .	48
3.16	Time evolution of the current density profile. Frames in the first column are taken at a local antenna current peak at the respective indicated times. Frames in the third column are taken at a phase $\pi/2$ later, i.e. when the antenna current is zero. At this time $dI/dt$ of the antenna current is maximum in the reverse direction, so the reverse current is just beginning to appear. The middle column of contours is at an intermediate time between. . . . .	50
3.17	(a) 2D contours (antenna located near $x = -22$ cm) of inductive power evolution over half of an RF cycle. The two rows correspond to two time stamps (25 and $45 \mu s$ ) in the early discharge. The columns from left to right are times, $t/T_{RF} = 0, 0.125, 0.25, 0.375,$ and $0.5,$ respectively. The first column correspond to maximum antenna current. Note that there is a small negative power (most pronounced in the second column). (b) Total inductive power integrated through the volume shown together with input power. The red dots correspond to the two times shown in panel (a). . . . .	52
3.18	A summary of different plasma parameter's evolution during pulsed discharge in Ar 1kHz 50% duty cycle with peak input power of 300 W. . . . .	53
3.19	A simple circuit representation of the ICP system. Capacitive coupling is represented as $C_{es}$ and $R_{es}$ ; inductive coupling is represented as $L_p, R_p,$ and $M_{ap}$ (mutual inductance between $L_{ant}$ and $L_p$ ). . . . .	55

3.20	Comparison between lumped element model (blue) and experimentally measured (orange) antenna current (solid) and power (dashed) with constant circuit elements. The fill pressure are 5 and 25 mTorr for panel (a) and (b) respectively. . . . .	58
3.21	Comparison between lumped element model (blue) and experimentally measured (pink) power. The fill pressure are (a) 25 and (b) 5 mTorr. The inductive, capacitive, and antenna loss power are calculated using $V_p^2/R_p$ , $V_{es}^2/R_{es}$ , and $I_{ant}^2 R_{ant}$ , respectively. . . . .	58
3.22	Simulation result of voltage and current in the circuit. The panels from top to bottom are antenna current, inductive plasma current, inductive plasma voltage, capacitive plasma voltage, and power. They are measured in the circuit at locations shown in Fig. 3.19. In the period of time designated in blue, $R_p$ is held constant at 20 $\Omega$ in (a) and 1000 $\Omega$ in (b). During the portion of the discharge designated in orange, $R_p$ linearly decreases from its initial value to 8 $\Omega$ in both panels. In the green section, $R_p = 8 \Omega$ in both panels. . . . .	60
A.1	Langmuir probe circuit simulated in SPICE (a) without rf compensation (b) compensated with resistors (three resistors to reduce parasitic capacitance) (c) compensated with inductors. Signal generators labeled VP simulate rf oscillation of the plasma potential. This is connected to the probe tip through "plasma R". The function generators labeled VS represent voltage ramp generators to sweep the probe. Voltage monitors VM1/3/5 measure the current in the circuit and VM2/4/6 measure voltage on the probe. Note that VM4 in panel (b) does not measure the voltage on the probe tip directly. The coax inside the probe shaft is terminated in 50 $\Omega$ so is frequency independent. In panel (b) and (c), an extra ring is placed inside the plasma to enhance the AC connection between probe tip and plasma. . . . .	67

A.2	(a) Measured impedance of the compensated probe as a function of frequency. (b) Bench setup using E5100A Network Analyzer for testing the probes. (c) Photo of the probe with compensation circuit. Note that the circuit board cannot be placed inside the probe shaft. d) Probe with AC coupling ring. . . . .	69
B.1	Vacuum (no plasma) frequency response of the hairpin probe. (a) Transmitted (S21) and reflected (S11) signal recorded on a Network Analyzer. (b) Mixer output signal from the hairpin probe circuit collected by a digital scope. (c) Blue solid line: amplitude of the mixer output signals. Orange solid line: Gaussian fit of the envelope. Blue dashed line: frequency sweep from the VCO. . . . .	72
C.1	A subset of Bdot probes constructed during the course of the thesis work. a) Single turn 3-axis probe painted with white epoxy. b) Probe constructed by winding around 6 sides of a ceramic cube. To protect the wires from plasma damage, the probe is painted with epoxy, as in panel (c). Panel (d), and (e) are larger versions of this type of probe used to test the degree of perturbation to the plasma. Panel (d) shows the 6 mm cube and (e) shows the 15 mm probe, constructed by adding a covering to the tip shown in (d). . . . .	74
C.2	Line-outs of azimuthal current density profiles at two pressures in steady state H-mode Ar plasma, illustrating the effects of different size Bdot pickups. The time corresponds to the current maximum on the rf antenna. (a) and (b) are radial profile at $z = 13$ cm; (c) and (d) are axial profile at $x = -16$ cm. The current profile is distorted when the coil diameter approaches the magnetic field gradient scale length; there is no apparent effect from local blocking of the current. . . . .	76

D.1	Flow rate effect on density profile in Argon steady state plasma. The blue curves are acquired with the gas at the top center of the chamber. The orange curves are acquired while gas is pumping in from the left side of the machine. Panels (a) and (b) correspond to 10 sccm flow rate; (c) and (d) correspond to 100 sccm. (a) and (c) are measured at less than 3 mTorr; (b) and (d) are measured at 25 mTorr. Note that at 100 sccm, 3 mTorr is the minimum pressure the chamber is able to achieve with its pump ability. Data are acquired using the hairpin probe moved along radial chords at 12 cm above the wafer. . . . .	77
D.2	Flow rate affect on (a, b, c) azimuthal current $J_\phi$ and (d, e, f) inductive power $P$ . Plasma operates in steady state Argon with 300 W input power. Pressure is maintained at 25 mTorr by changing the opening of the pendulum valve for pump out and varying the inflow mfc. $J_\phi$ is shown at time of maximum antenna current and $P$ is shown for average over an rf cycle. Note that $P$ is drawn on log scale to highlight the differences. . . . .	79

## LIST OF TABLES

1.1	Typical parameter space of weakly ionized low-pressure plasma discharges. . .	2
3.1	Power deposition computed as the volume integral of $\vec{J} \cdot \vec{E}$ with recalibration by the model to account for unobserved volumes of the reactor and coil resistive losses as a function of generator power for Argon plasmas at 10 mTorr. The renormalized power is the experimental power divided by fraction of power inside the view window. . . . .	38

## ACKNOWLEDGMENTS

I would like to thank Professor Walter Gekelman for being my advisor. I have learned many valuable lessons from him. I would like to thank Professors Troy Carter, George Morales, and Christopher Niemann for serving on my committee and educating me on plasma physics; thanks also to the NSF for paying my salary to do all the interesting experiments; and thanks to Lam Research Corp for donating the tool to perform these experiments on. I would like to thank several people in the field of low temperature plasma and their valuable discussions—professor Mark Kushner and his group at University of Michigan for the associate simulation collaboration; Dr. Hyo-Chang Lee, Professor Igor Kaganovich, Yevgeny Raitses and all the others who talked to me at conferences.

Secondly, I would like to thank all the people who helped me through my graduate career at the Basic Plasma Science Facility (BaPSf)—Tai Ly, Marvin Drandell, Zoltan Lucky, and Avdit Kohli for their support on construction and engineering part associate with the experiment. I would like to thank Drs. Shreekrishna Tripathi, Steve Vincena, Bart Comperolle, and Byonghoon Seo for their help on physics or non-physics related discussions in the lab. Thank all the grad and undergrad students that I had worked with at some point. Thanks to Meg Murphy for patiently making the necessary purchases. I am very happy with my various encounters at UCLA. It was a pleasure working with everybody at BaPSf and I hope they were having fun as well.

Last but not least, I would like to thank Dr. Patrick Pribyl, one of the most important person to my graduate career. I would not be able to accomplish what I have today without him. I have learned a lot from him in many perspectives (like if you are quick enough you can clean a soldering iron tip with your fingers). Some of these lessons I'm sure I'll remember for the rest of my life, and make sure I pass them on to the future generations.

## CURRICULUM VITAE

- 2013 – 2017            B.A. in Physics, University of Colorado, Boulder, CO.
- 2017 – 2020            Graduate student researcher, University of California, Los Angeles, CA.

## PUBLICATIONS

- J. Han**, P. Pribyl, W. Gekelman, and A. Paterson, “Three-dimensional measurements of fundamental plasma parameters in pulsed ICP operation”, *Physics of Plasmas* **27**(6), 063509 (2020).
- J. Han**, P. Pribyl, W. Gekelman, A. Paterson, S. J. Lanham, C. Qu, and M. J. Kushner, “Three-dimensional measurements of plasma parameters in an inductively coupled plasma processing chamber”, *Physics of Plasmas* **26**, 103503 (2019).
- X. Fan, Y. Wug, **J. Han**, P. Pribyl, T. Carter, “Electron Density Measurement using a Partially Covered Hairpin Resonator in an Inductively Coupled Plasma”, *Rev. Sci. Instrum.* **91** (11), 113502
- S. Razavian, **J. Han**, B. Jamali, P. Pribyl, M. Hosseini, Y. Mehta, M. Forghani, W. Gekelman, A. Babakhani, “Plasma Characterization using a Silicon-Based Terahertz Frequency Comb Radiator”, *IEEE Sensors Letters*, **4**(9), 1-4 (2020).
- W. Gekelman, P. Pribyl, Z. Lucky, S. W. Tang, **J. Han**, and Y. Qian, “Design, construction and utilization of a university undergraduate plasma lab”, *J. Plasma Phys.* **26**, 103503 (2020).

# CHAPTER 1

## Introduction

Low temperature plasma discharges are widely used in chemical processes which usually employ energetic ions to modify the surface properties of materials. This is critical for industries in the world such as automotive, aerospace, biomedical, electronics, steel, and toxic waste management. One of the biggest beneficiaries among these industries is the manufacturers for integrated circuits (ICs) used in electronics. IC fabrication consists of hundreds or thousands of steps. Typically one-third of these steps are plasma-based. This includes removing, depositing, or modifying selected materials on a typically silicon wafer. The removal process is done with plasma etching[1, 2, 3, 4], while deposition is done by ion implantation[5]. Plasma-based surface processes enable mass production of chips with complex structures on a scale size inaccessible to wet chemical processes. Research in low temperature plasmas strives to give a deeper understanding of the underlying fundamental principles, in order to control and improve plasma processing applications.

Etching uses plasmas with electronegative gases (ie. chlorine or fluorine) where the positively charged ions bombard the wafer to remove materials. The chemically reactive free radicals react with the etched material to form volatile or nonvolatile byproducts. The goal is to remove a precise amount of material from a selected area on the substrate. This is more and more challenging as the spacing between the features become smaller (nm scale). A stable and controllable plasma source that produces high etch efficiency is desirable. Although industry has been using plasma etch tools for decades, there are still gaps in the understanding of the fundamental physics and chemistry behind the operation of these machines.

density ( $n$ )	$10^8 - 10^{13} \text{ cm}^{-3}$
electron temperature ( $T_e$ )	1-10 eV
ion temperature ( $T_i$ )	$< 0.1 \text{ eV}$
pressure	0.1 mTorr - 1 Torr

Table 1.1: Typical parameter space of weakly ionized low-pressure plasma discharges.

Plasma discharges used in processing are weakly ionized[6]. This means the plasma represents a small fraction of the neutral gas density ( $\frac{n_i}{n_i+n_g} \ll 1$ ), and collisions between charged particles with neutral gas molecules are non-negligible[7]. The discharges are typically sustained electrically[8]. Reactants flow into the reactor as neutral gas. An applied field heats the electrons, and those with sufficiently high energy collide with neutrals and ionize the gases. The ions exchange energy by colliding with the background gas. The electrons are not in thermal equilibrium with the ions. Weakly ionized plasmas can be roughly set into two categories—low and high neutral gas pressure, characterized by the electron mean free path compared to the dimensions of the reactor. The experiment described in this thesis work will operate in the low pressure region with basic parameters shown in Table 1.1. The compact machine sizes makes boundary effects (surface losses) important. The main loss mechanisms of the plasma are diffusion and recombination into neutral gas, which is then pumped from the chamber, providing a continuous flow-through.

Most processing discharges use mixtures of electronegative molecular gases in order to achieve the desired etch/deposition profile. This involves physical processes (i.e. ion bombardment to activate local bonds in the wafer lattice), and chemical processes as the reactants combine with the material being etched. The removed remnants react with the gas and get pumped out from the chamber. Because the reactants are both molecular and electronegative the process can be complicated. Prior to studying the complicated cases, a fundamental baseline must be established so that plasma behavior due to ionization, diffusion, or the electric field can be separated from that due to dissociating molecules,

generate or destruct negative ions, and gas-phase chemical reactions[9, 10, 11]. This is why enormous studies have been done with Noble gases, especially Argon. In actual industry applications, processing discharges frequently use a mixture of Argon with electronegative gases. Argon is also used to initiate the plasma, as it is easier to breakdown.

## 1.1 Inductively Coupled Plasmas

This thesis work is conducted in an industrial inductively coupled plasma device (ICP) designed for plasma etching in microelectronics fabrication. The chamber is modified to allow diagnostic access. Plasma is sustained by an RF antenna coupled inductively across a dielectric window. In an ICP the antenna typically has a shape of a flat spiral (stovetop) coil sitting on top of the device, as in this work, or a solenoidal coil wound around a cylindrical vacuum chamber[12]. The electrical power is coupled mostly to electrons. Energy is then transferred from electrons to ions and neutrals through collisions.

In a typical semiconductor reactor, the silicon wafer substrate is placed on the electrode at the bottom of the machine. While the antenna coil generates and sustains the plasma, the bottom electrode, modulated by a separate RF controller, creates an RF sheath on the substrate which accelerate ions for bombardment. This separates plasma parameter control and ion energy control. A key advantage of ICP is a non-capacitive power transfer, which makes for a low voltage drop across plasma sheaths at wafer and wall surfaces. A desirable plasma etch tool has the following properties: (1) uniform plasma and reactant density across the wafer, (2) highly controllable ion energy at the wafer surface, and (3) is stable and repeatable. Although it is possible to use an ICP without knowing the specific details of plasma behavior, the pursuit of a finer etch profile across the entire wafer drives studies and measurements of fundamental plasma properties in these machines.

Previous work utilized a variety of diagnostics to measure plasma parameters. Scheubert *et al.*[13] investigated a Helium plasma in a stove-top coil configuration. Radial and ax-

ial profiles of electron density as well as the pressure dependence were determined by Langmuir probe measurements. Quantitative spectroscopic methods were used to determine electron density ( $n_e$ ), temperature ( $T_e$ ), energy distribution function (EEDF), and gas temperature ( $T_g$ ). The experimental results were compared with a model based on hydrodynamic balance equations and showed excellent agreement. The authors found that the power transferred into the plasma increases with increasing pressure and RF generator power.

Similar results were observed in a steady state Argon ICP discharge. Using Thompson and Rayleigh scattering, Hori *et al.*[14] found that  $n_e$  increased as pressure and power increased, and always peaked in the plasma center.  $T_e$  is insensitive to changes in power, but decreased when the pressure increased, and was uniform throughout the radial direction of the chamber at the height of the laser beam. The neutrals were strongly depleted from the plasma center due to heating by charged particle collisions.

Investigations of electromagnetic properties of ICPs have been performed over the past two decades. Two components of the magnetic field ( $B_r$  and  $B_z$ ) were measured along one radial and one vertical line by Godyak *et al.*[15] in an ICP sustained Ar plasma at pressures of 1-10 mTorr with a stovetop coil driven at 6.78 MHz. The magnitude and relative phase of the magnetic field were measured using a “vector voltmeter”. The authors assumed azimuthal symmetry based on having equally spaced concentric antennas. Using the measured two components of the magnetic field, the current density was calculated by taking derivatives along the radial line, assuming  $\frac{\partial}{\partial r}$  was uniform as a function of height[16]. The current density peaked within 1 cm of the dielectric window adjacent to the antenna, and reversed direction in a second layer 6-8 cm from the dielectric.

El-Fayoumi and Jones[17] measured one component of the magnetic field inside the volume of the chamber on a plane consisting of 608 locations. The radial magnetic field was deduced from the axial field measurement using  $\nabla \cdot \vec{B} = 0$ , and assuming the azimuthal magnetic field to be zero. The experimental data were then fitted to polynomial functions.  $\nabla \times \vec{B} = \mu_0 \vec{J}$  was then used to determine the plasma current. The current

formed a toroidal ring under the stovetop coil, and axially translated several cm away from the coil during a quarter RF cycle.

Hebner[18] measured ion and neutral temperatures using Laser-induced fluorescence in Argon plasma. He found that their temperatures are identical in the plasma center, whereas ions are hotter on the edge due to drifting in the radial electric field. He also noted that at RF power  $> 300W$ , neutrals can be hot enough to influence discharge kinetics and gas phase chemistry.

A two-dimensional simulation[19] in pulsed Ar/Cl<sub>2</sub> plasma shows the mixture having a lower electron density relative to the pure Argon plasma due to electron attachment to Cl<sub>2</sub>. In quasi steady state, with 20% Chlorine the plasma has an electronegative core and electropositive periphery. In a chamber with a similar coil geometry, experimental results in a pure Chlorine plasma has  $n_e$  peaking in the middle of the chamber between 1-20 mTorr[20, 21]. The negative ion density is very low at high power and low pressure, which is related to the high percentage of dissociated Cl<sub>2</sub>.

## 1.2 Pulsed operation

Having reached a limit in process improvement available with steady state plasmas (CW), the semiconductor industry is turning to temporal modulation of the RF input power in these reactors[4]. Pulsing provides additional parameter space for customizing fluxes to the wafer. The capability of changing ion energy, ion flux and radical flux provides the ability to vary etch rate, and to achieve higher selectivity[22, 23]. Pulsing can suppress certain classes of instabilities, and reduce charging damage to the devices being fabricated[24, 25]. At the same time, pulsed plasmas introduce other challenges.

Previous theoretical investigations of pulsed ICP operation includes a global model developed by Ashida *et al.*[26], who attempted to explain the plasma evolution while changing the duty cycle and applied power. Two and three dimensional simulations have been carried out to improve the understanding of pulsed operations[27, 28, 19, 25]. For

example, Subramonium and Kushner[28] investigated the consequence of varying pulse repetition frequency, duty cycle, power, and pressure in Argon plasma with a two dimensional model. Their result agrees with the one dimensional measurement performed on the GEC reference cell[29] by Hebner and Fleddermann[30].

Single point measurements of the time dependent  $n_e$  and  $T_e$  in various studies had been performed using Langmuir probes[26], electrostatic probes[31], hairpin resonator probes[32], and capacitive coupled probes[33] etc. Hebner *et al.*[30] reported on the time variation of line averaged  $n_e$  using a microwave interferometer with variation in pulse frequency and duty cycle.

Celik *et al.*[34] generalized a complete picture of several physical processes(ie. electron cooling, recombination) in the afterglow (RF power off portion of a pulse cycle). The diffusive cooling mechanism of electrons has been studied with models[35, 36, 37]. Maresca *et al.*[35] measured the depletion of energetic electrons leading to rapid cooling of electrons shown by the measured EEDF.

Park *et al.*[38, 39] measured temporal and spatial distribution of ion flux and electron temperature using a set of probes resting on the wafer with a phase delayed harmonic analysis method. They observed ion flux peaking in the middle of the wafer, and  $T_e$  peaking on the edge during the active-glow (RF power on portion of a pulse cycle).

ICPs don't always operate with inductive power. At low RF power and low density, power couples to the plasma capacitively via electrostatic fields, whereas at higher density the coupling becomes electromagnetic. This is first recognized by MacKinnon *et al.*[40] in 1929, where he described a "dim" discharge as being of electrostatic origin, and a "very bright" discharge as electromagnetic origin. In 1978, the two modes of operation were described again by Chandrakar[41]. In 1991, Amorim *et al.*[42] named the two modes "E discharge" and "H discharge". Subsequent references[12, 43] citing Amorim immediately began using the terms "E-mode" and "H-mode" for capacitively coupled and inductively coupled modes of operation in ICP. Note that about the same time, the "H-mode" (for high confinement) scaling law was being promoted as an advance in toka-

mak research. The two terms have nothing to do with each other. In fact, in low temperature plasmas, “H-mode” might more properly be called “B-mode”. However, “H-mode” and “E-mode” have a long history as terms of art in optics (i.e. gratings) and waveguides.

Explaining the underlying physics behind E-H mode transition has motivated numerous experimental and theoretical studies[44, 45]. Studying and controlling plasma going through mode transition during pulsed operation is useful for understanding the etch profile when such plasma pulsing is used in the future.

### 1.3 Motivation

Previous research on low pressure ICPs have provided keen insights into their operation, and established many of the fundamental operating principles. However, in most cases, only a subset of plasma properties have been reported, and rarely in multiple dimensions (space and time) due to limitations in diagnostics. This thesis undertakes simultaneous measurements of nearly all plasma and electromagnetic properties of an ICP in three-dimensions (3D). Some plasma parameters have been measured using multiple diagnostics. For example, electron density measurements from three very distinct diagnostic techniques (interferometer, Langmuir probe, Hairpin resonator probe) under the same condition are reported. This increases confidence in the measured results.

Understanding the fundamentals behind E-H transition has always been of key interest in the field over the past 20 years. This thesis studies E-H transition through measurement of various plasma parameters during pulsed operation. By varying pressure and power in pulsed operation, two types of density profile are measured in argon plasma. A simple lumped element circuit model was tested with experimental result. The model helps with interpreting the experiment observations, as well as explaining the physics behind E-H transition. Understanding the plasma behavior are useful for controlling the tool to operate under various conditions. This will help with the future design of ICP etch tools.

## CHAPTER 2

### Experimental setup and Diagnostics

#### 2.1 Experimental chamber

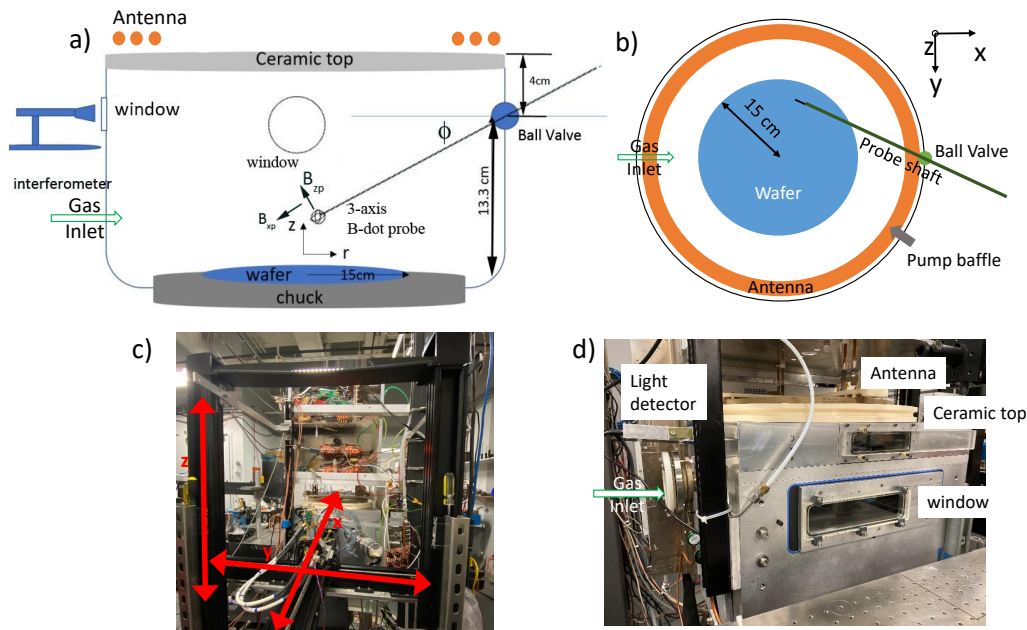


Figure 2.1: Schematic of the experimental chamber from (a) side view and (b) top view. Photo of (c) the 3D probe drive and (d) the chamber. The probe is capable of rotation and translation with the ball valve as the pivot point, allowing 3D measurement in the chamber. The wafer is electrostatically clamped to the top of the chuck assembly, where RF bias can be applied. Gas is exhausted through a gap between the chuck assembly and the chamber wall.

The experiment[46, 47] is conducted in a cylindrical chamber (height = 17.2 cm, radius = 26 cm) that operates between 0.5 – 300 mTorr. A double-wound 1.5-turn circular

stovetop antenna, mounted on top of a 2.8 cm thick alumina window, was connected to an RF generator operating at 2 MHz delivering power up to 1 kW. The RF generator can be pulsed at arbitrary repetition rates and duty cycles. A schematic of the experimental apparatus is shown in Fig. 2.1. Bias can be applied to an electrode with a Si wafer ( $r = 15$  cm) electrostatically clamped on the RF chuck assembly ( $r = 22.75$  cm), and cooled with backside helium flow. Feedstock gas flows through an inlet on the side wall (shown in the schematic about 2 cm above the wafer, and exhausts through an annular gap between the chuck and the chamber wall (note that this is in contrast to the unmodified industrial tool where more attention has been given to symmetric gas flow). A pendulum valve connects the chamber to a turbo pump, and pressure is controlled by varying its setpoint. The wafer is defined as  $z = 0$ , with its center at  $x = 0, y = 0$ . Positive  $\hat{x}$  points toward the probe insert location.

RF power from the generator was calculated by measuring current and voltage at its terminals. These values are substantially in phase, although an exact multiplication over many cycles was performed prior to computing the average value. Power lost in the antenna and the RF delivery system between the generator and plasma is a few percent. To validate these measurements, we placed a 1-turn loop just above the RF antenna, with a resistor in series, while making no other changes to the system. Dissipation in the inductively coupled test circuit is measured by computing  $I^2R$  in the absence of plasma, measured at a typical operating antenna current, with the same “match” settings as when there is plasma. The power dissipated in the dummy load arrangement was within a few percent of the reported generator power at all relevant powers. Accounting for heating in the RF conductors (determined by measuring their temperature rise and estimating convective cooling), the measured inductively coupled power is within 1% of the reported power. These cross-checks provide confidence in the accuracy of the power being delivered to the plasma.

In principle, the pulse waveform for the RF source can be programmed to any shape. In practice, a square wave modulation of the input voltage does not necessarily produce

a square wave modulation of the power. A feedback scheme programmed the ICP RF generator with the goal of driving a constant power waveform through the pulse. This is not always achievable, depending on the plasma conditions. The maximum rate of change, for instance during the current rise phase, is established by the  $Q$  of the  $LC$  circuit formed by the antenna inductance and the equivalent capacitance of the matching circuit, together with the maximum programmable output voltage. The time constant to dissipate the circulating energy is typically  $30 \mu s$ , which is the minimum antenna circuit response time for a rapidly changing plasma load. In cases where the power control circuit can't keep up with changes in plasma load, spikes in antenna power at the beginning of the pulses can occur. We have determined that the evolution in plasma density is not strongly affected by this overshoot. This was done in plasma conditions where power could be programmed as a function of time with and without overshoot; both cases had essentially identical spatial and temporal distributions of  $n_e$ .

Probes are inserted into the chamber from a side mounted flange utilizing a ball valve feedthrough[48]. The probe shaft can translate in and out through the ball valve, as well as rotate with the ball as a pivot point, allowing free rotation of the probe shaft through  $\theta$  and  $\phi$  in spherical coordinates. The probe motion is driven by a 3D drive shown in Fig. 2.1 (c). The stepping motors have embedded controllers and interface to a computer, and can position the attachment point of the probe with a linear precision of 10 microns along each drive. The probe tip can be located on a grid within the chamber precise to within about 50 microns, although there is up to a 0.5 cm difference between this grid position and chamber coordinates over the full extent of the 3D volume. The rotational limit on the ball valve and position of the port prevent the probe from reaching a region immediately adjacent to its mounting point. This is indicated by missing data in figures showing 2D planes of 3D data. Data were acquired using a multi-channel 12 bit oscilloscope. The probe motion and data acquisition systems were controlled by a Python program communicating with both motors and scope through Ethernet protocols. Probe data are typically on a 2D or 3D grid having 1 cm separation between points. A detailed description of the

data acquisition system is in section 2.7.

A visible light detector consisting of a silicon photodiode with an op-amp current-to-voltage converter circuit is located outside a window (Fig. 2.1 d). A collimating lens gives a field of view of about 4 degrees.

## 2.2 Langmuir probe

The simplest way to diagnose a plasma is to insert a metal probe and bias it positively or negatively to draw electron or ion current or on its sweep. This is the *Langmuir probe* introduced by Irving Langmuir about a century ago[49]. Because they are cheap and easy to build, Langmuir probes are still a very popular diagnostic tool in low-temperature plasmas.

Interpretation of Langmuir probe data relies heavily on the theory and assumptions used in the process. We choose to use ion saturation current ( $I_{isat}$ ) from a cylindrical probe (tungsten wire,  $l = 1.43$  mm,  $d = 0.28$  mm) in steady state and  $dI/dV$  from a planer probe (tungsten plate,  $2 \times 2 \times 0.2$  mm) in pulsed plasma to measure  $n_e$  and  $T_e$ . Langmuir probe density can be calibrated with the interferometer and hairpin probe. The following subsections address the problems encountered while using Langmuir probes and justify our choices for analysis.

### 2.2.1 Langmuir probe theory and analysis

Three analysis schemes are described below. Two of which are used on planer probes, and one for cylindrical probes. All three methods are used in this thesis, depending on plasma conditions.

The easiest way to find plasma density from Langmuir probes is using Orbit Limited Motion (OML) theory. OML works best with cylindrical probes under the assumption that the sheath is a circular cylinder concentric with the collector[49].

According to OML, the ion current to a cylindrical probe in a Maxwellian plasma is

$$I_i = Aj_r \left[ \frac{2}{\sqrt{\pi}} \chi^{1/2} + e^\chi (1 - \text{erf}(\chi^{1/2})) \right] \quad (2.1)$$

where  $A$  is the area of the probe,  $j_r$  is the random current density of ions crossing a unit area in one direction in the plasma,  $\chi \equiv \frac{e(V_b - V_p)}{kT_i}$  with  $V_b$  being the bias voltage and  $V_p$  the plasma potential. In the thin sheath approximation, the above equation reduces to

$$I_i \approx Aj_r \approx \alpha n e A \nu_B \quad (2.2)$$

assuming the ions enter the sheath with Bohm velocity

$$\nu_B = \sqrt{\frac{kT_e}{M}} \quad (2.3)$$

Here the ion density  $n_i$  is represented as  $\alpha n$ , where  $\alpha$  is a general calibration factor that must be obtained from a more accurate diagnostic (ie. microwave interferometer). Equation 2.2 describes a linear rise of ion saturation current with bias voltage through the arbitrary factor  $\alpha$ , with slope depending on the sheath/presheath condition[50, 51]. If the electron temperature is known, the ion density can be deduced from ion saturation current. Equation 2.2 works for a cylindrical probe with a thin sheath in a Maxwellian plasma. There are other ion theories (i.e. Allen-Boyd-Reynolds[52] or Bernstein-Rabinowitz-Laframboise[53, 54]), but none of them match perfectly with non-intrusive measurement techniques at all situations[55]. The relation  $n_i \propto I_i$  works as long as the probe sheath condition stays relatively the same wherever the probe is located. This is true for steady state or quasi-steady state Argon ICP. The use of a more complicated theory in such cases is not usually warranted as it does not improve the accuracy of the final result in a big way.

For a non-drifting Maxwellian plasma where the probe sheath is small compared to the probe dimension, a planer probe measures an electron current of

$$I_e(V_b) = An_e e \sqrt{\frac{kT_e}{2\pi m_e}} e^{-\frac{e(V_p - V_b)}{kT_e}} \quad (2.4)$$

where  $V_b$  is the voltage bias on the tip and  $V_p$  is the plasma potential[49, 56, 57].  $T_e$ ,  $n_e$ , and  $V_p$  can be derived from the swept IV curve, if the plasma is Maxwellian. This corresponds to steady state or quasi-steady state in Argon ICP.

A different route of analysis focus on finding the distribution function from IV curves. This is crucial for non-Maxwellian plasmas. Druyvesteyn[58] showed that the second derivative of the probe current with respect to the sweep voltage  $d^2I/dV^2$  is proportional to the energy distribution function  $f(\epsilon)$ . Note that this is only valid for a cylindrical probe if the distribution is isotropic.

Finding the distribution function from  $d^2I/dV^2$  is a widely used method in process plasmas[59]. After implementing this scheme in experiment, we experienced very poor signal to noise ratio. Noise can be reduced by applying either an analog or digital filter to the measured current, but any small distortion of the IV curve by filtering will reflect on  $d^2I/dV^2$  and has the potential to be misinterpreted as an actual physical “feature”. In the non-Maxwellian plasma scenarios that we were measuring, we determined that distribution functions extracted from  $d^2I/dV^2$  are unreliable, particularly in pulsed mode where the frequency response must be sufficiently high that it can track plasma changes on the time scale over tens of microseconds.

In order to monitor the beginning of a pulsed plasma discharge with non-Maxwellian and fast growing  $T_e$ , we made a slight modification to the above approach. A double-sided planer Langmuir probe made from a thin tungsten plate with the tip’s width (2 mm) much larger than the thickness (0.2 mm) was used. A one dimensional assumption was made, where the 1D EEDF perpendicular to the probe face is proportional to the first derivative of the characteristic[60],

$$f_{1D}(V) = \frac{m}{q^2 A} \frac{dI}{dV} \quad (2.5)$$

Here  $I$  is the current collected by the probe,  $V$  is the bias voltage with respect to the chamber wall, and  $A$  is the probe area.  $n_e$  is found by integrating the distribution function:

$$n_e = \frac{2m}{qA} \int \frac{dI/dV}{\sqrt{2mV}} dV \quad (2.6)$$

EEDF in ICPs are frequently Non-Maxwellian, so in the present work the electron temperature is defined as the mean kinetic energy of the electrons:

$$T_e = \int v^2 f(v) dv \quad (2.7)$$

To find the velocity distribution function  $f(v)$ , one needs a well defined plasma potential. One definition is the maximum of the first derivative  $dI/dV$ , although this is only valid for non-drifting plasmas. The chosen value of  $V_p$  significantly affects the shape of  $f(v)$ , and can make a Maxwellian distribution appear non-Maxwellian and vice versa. This will also result in an under/over estimate in computed density, which is more significant when the plasma is very cold. Even though a separate measurement of  $V_p$  is recommended for better accuracy, to the author's knowledge no published work has actually done so. During the course of the thesis work, such attempts were made to deduce  $f(v)$  by applying  $V_p$  measured using an emissive probe to the Langmuir probe IV curve. The attempt was not successful as the emissive probe failed to work in the region of interest (see sec 2.3).

Using  $dI/dV$  instead of  $d^2I/dV^2$  enhances the signal to noise ratio by 1 to 2 orders of magnitude. However, equation 2.5 assumes the probe only collects particles flying towards the surface from the direction perpendicular to the probe surface. This is somewhat troublesome if the probe sheath expands out to a blob surrounding the probe. This also neglects  $f(v)$  from the direction parallel to the plane of the probe surface.

Time evolution of the EEDF is measured using a stepped sweep method where the probe voltage is scanned between -5 V to +20 V with a resolution of 200 steps. This method has been used by others [35, 59] to measure EEDF in the afterglow using steps that are essentially DC compared to the pulse period.

To study the anisotropy of  $f(v)$ , a single sided Langmuir probe is constructed by painting one side of the double sided probe with high temperature epoxy. At each location

inside the chamber, data was acquired with the probe tip pointing in four cardinal directions relative to the probe shaft. Note that with an anisotropic distribution, Druyvesteyn's calculation of  $d^2I/dV^2$  also cannot be implemented to cylindrical probes in this case.

### 2.2.2 Langmuir probe in RF plasma

Plasma potential is the potential difference between a point inside the plasma relative to the chamber wall. In an ICP, the RF from the antenna couples to the plasma, making  $V_p$  oscillate at the RF generator frequency. This is significant when plasma oscillates with electrostatic field. The probe current can be written as[56]

$$I_e = (I^* + \tilde{I}) \exp \left[ \frac{-e(V_p + \tilde{V}_p - V_B)}{T_e + \tilde{T}_e} \right] \quad (2.8)$$

where  $\tilde{I}$ ,  $\tilde{V}_p$ , and  $\tilde{T}_e$  are the fluctuating RF components. To simplify the analysis we assume  $\tilde{T}_e = 0$  and  $\tilde{I} = 0$ , the time averaged current can be written as

$$\langle I_e \rangle = I^* \exp \left[ \frac{-e(V_p - V_b)}{T_e} \right] \left\langle \exp \left[ \frac{-e\tilde{V}_p}{T_e} \right] \right\rangle \quad (2.9)$$

A simple averaging over the probe current will distort the IV curve as shown in Fig. 2.2. In panel (a), an averaging over two curves with  $\tilde{V}_p = \pm 5V$  distorts the original curve. Panel (b) shows IV curve under sinusoidal  $\tilde{V}_p$  of different amplitudes. The shift in current can be described by the modified Bessel function of the first kind  $I_0 \left( \frac{e\tilde{V}_p}{T_e} \right)$ [56]. For  $e\tilde{V}_p < T_e$ , the distortion to the IV curve can be neglected. Otherwise without proper compensation to eliminate RF, the measured  $V_p$  will appear lower,  $T_e$  will appear higher, and the electron saturation current ( $I_{esat}$ ) will appear up to a factor of 2 lower than their true values. Note that this effect does not distort the ion saturation current. This means that when there is no electrostatic RF field or measurements are made far away from the antenna, an uncompensated probe will be enough.

In order to make measurements where  $e\tilde{V}_p > T_e$ , the Langmuir probe is compensated by an RF choke filter located near the probe tip. Details of the compensation circuit and its application is described in Appendix A.

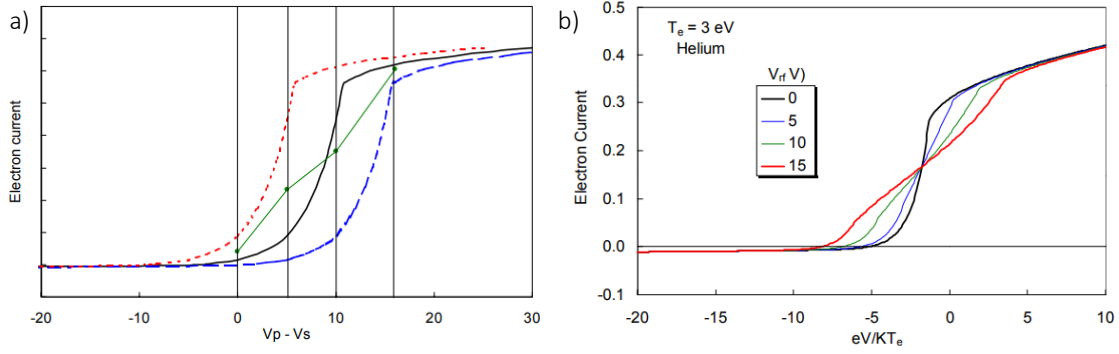


Figure 2.2: Langmuir probe IV characteristic with RF oscillation on sweep voltage  $V_s$ . (a) Blue and red dashed curves are a result of  $\pm 5$  V fluctuation in  $V_s$  on the solid black curve in the middle. Green solid line is average of blue and red curve, which differs from the black center curve. (b) IV characteristic as a result of sinusoidal oscillations at various amplitudes. Figures from F. F. Chen[61].

When “step sweeping” the probe in plasma, we observed a saturation in electron current if the probe is continuously biased. Depending on plasma conditions and probe position, the shortest time to observe a saturation only takes about  $50 \mu s$ . This phenomenon has not been described anywhere in previous literature. Fig. 2.3 shows an example of such a situation. A 300 W argon plasma at 10 mTorr is running with a 1 kHz rep rate (on for 0.5 ms and off for 0.5 ms). Panel (a) shows the current on the probe by biasing the tip to +25 V for 7.5 ms. The delay between each voltage burst is 900 ms and probe is biased into  $I_{isat}$  during those intervening times. We can see that the quasi-steady state current measured at  $t = 6$  ms is 30% lower than that at  $t = 0$  with the same probe at the same bias voltage under the same plasma pulse. This means that  $I_{esat}$  derived from a curve at  $t = 6$  ms is distorted. The distortion is more significant at higher density ( $> 10^{11} cm^{-3}$ ). To avoid this distortion, we limit the bias voltage burst to  $50 \mu s$ , and shift to the time of interest during the pulsed cycle. The IV curve is successfully reproduced since all RF compensation circuit elements’ charging currents decay to zero within  $25 \mu s$ , allowing  $25 \mu s$  of observation time. Note that for the situation shown in Fig. A.1 (a), a 1.5 ms probe

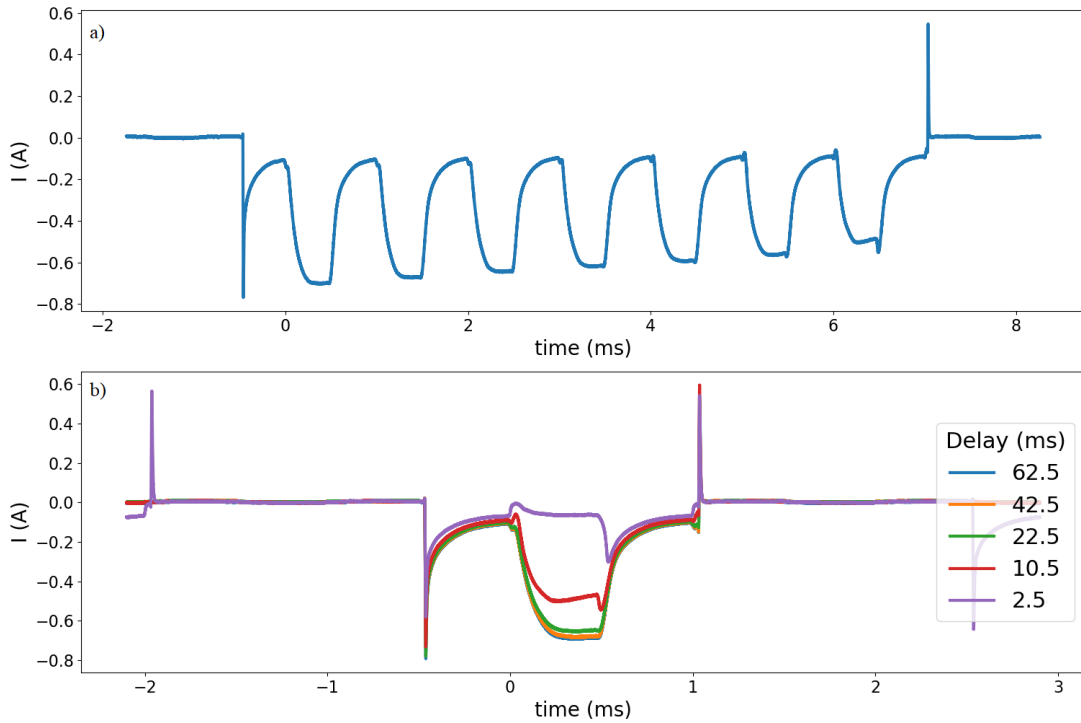


Figure 2.3: Langmuir probe electron current vs time measured at the center of the chamber. Plasma operating at Ar 25 mTorr. Probe biased at +25 V during on-time and -50 V during off-time. Positive bias results in collecting electrons, so the active glow phase is during the more negative sections. (a) Probe bias on for 7.5 ms and off for 900 ms. Plasma is pulsed at 1 kHz. The collected electron saturation current decreases over time. (b) Probe bias on for 1.5 ms. The delay intervals listed on the legend are between the re-application of the probe bias - too fast results in defective measurements.

bias time is feasible. Another important aspect is having a sufficient delay between each voltage pulse; having them too close together replicates the same issue. This is shown in Fig. 2.3 (b). A 1.5 ms +25 V pulse was applied to the probe with the same condition and probe position as panel (a). We see that the delays between measurement pulses on the probe shorter than 50 ms results in consecutive measured current being distorted.

The above phenomenon happens regardless of probe shape, size, material, and occurs

with either compensated or uncompensated probes. This reveals a problem unmentioned by previous researchers—the IV curve sweep time must be short (such that probe current does not decay for a given bias), but also not too short ( $\geq 1\mu s$ ) such that ions cannot participate in establishing the sheath. We are not sure in what sense short is defined – it seems to possibly be related to wall conditions. The only way to determine “short enough” is by a sequence of tests like those described above. We note that a similar observation was reported during the early afterglow by Liu *et al.*[62], who measured their defect as purely a circuit effect due to the charging of the capacitor connected to the auxiliary electrode. This is not true in our case, because the capacitance of the auxiliary electrode is carefully controlled to keep its time response on the  $10\mu s$  scale.

### 2.2.3 Sheath and plasma perturbation

Any object immersed in plasma forms a sheath surrounding it. The sheath voltage increases until the flow of positive and negative charge carriers to the surface becomes balanced. When a Langmuir probe is placed inside the plasma, it is actually measuring the particles entering the sheath surrounding the probe. This means that if the sheath expands to a sphere surrounding the probe, the theories in sec 2.2.1 will no longer hold. For plasmas described in this thesis, this is a worry when the plasma density is smaller than  $< 10^{10}cm^{-3}$ .

The presence of any object in the plasma depletes plasma locally. This makes any probe measured plasma density lower than non-intrusive methods. If plasma sheath is expanded, it will deplete more plasma. We conducted tests with three cylindrical probes of  $l = 1.43, 2.35, 8.68$  mm for determining this perturbation. Under the same condition, the resulting IV curve is different only for the longest tip.

The presence of the probe shaft across the entire chamber diameter has the potential of perturbing the plasma globally. A separate test was conducted using two probes simultaneously, with shafts of  $3/8$  and  $1/4$  of a inch in diameter. The IV curve measured by the  $3/8''$  probe remains unchanged as the  $1/4''$  probe moved close to it ( $\sim 1$  cm) or very

far away from it. In contrast, the current saturates by 80% when measured the other way around. Note that the test is conducted at the center of the plasma and the shaft partially intercepts the plasma, so the result can be a mixture of global and local affect.

The problem associated with sheath impedance has been discussed in section 2.2.2 with respect to RF fluctuations. Note that the circuit is not only measuring the sheath impedance surrounding the probe, but also that of the chamber wall (ground)[59]. This makes measurements almost impossible when the density around the chamber wall is few orders of magnitude lower than the core—the probe tip does not have a good connection to ground. One solution is by locating a new ground closer to the probe tip. This can be a large metal piece inside the plasma, provided that it does not get contaminated and become an insulator, and also does not perturb the plasma globally.

A different quantity to consider when choosing probe dimensions is neutral collisions. Probes used in this thesis work have dimensions much smaller than the electron-neutral (e-n) or ion-neutral (i-n) collision mean free path. This roughly limits the probes to operate below 30 mTorr. We expect the measured EEDF to be Maxwellian at high pressure and steady state conditions. If it is observed to be non-Maxwellian at high pressures, it is possible and even likely due to the probe perturbing the plasma[63]. The largest pressure we investigated with a Langmuir probe is 25 mTorr.

#### 2.2.4 surface contamination

A separate issue related to Langmuir probes is surface contamination. This includes contamination of the probe surface and the wall of the chamber containing the plasma. For example, we have found that a probe immersed in Argon plasma for 12 hours does not reach the nominal electron saturation current without cleaning at the end of that time period. For Oxygen containing plasmas, the contamination time can be as short as 10 minutes. After careful testing in Argon, we settled on a cleaning scheme of heating the probe tip to an orange glow using electron current, together with 30 minutes of ion sputtering at  $-100$  V before each data run. The probe is also biased into  $I_{isat}$  when not in use. We

do not report probe measurement in Oxygen containing plasmas, although probes with non-oxidizing tips (e.g. Platinum) are under investigation. Unfortunately, contamination on the chamber wall cannot be removed by heating. This may be caused by sputtering of the wafer (or the probe materials) and often occurs with  $O_2$ . We tried cleaning the chamber by running  $SF_6$  or Hydrogen plasma. The latter seems more sufficient, as it re-assembles the plasma behavior prior to contamination and is the scheme we used during the experiment.

Probe tip cleaning limits the material to use for a probe tip. Metals with a lower melting point such as copper cannot be used. Tantalum suffers from sputtering onto nearby insulators, resulting in significant decrease of its effective area. A planar Ta probe placed in the plasma for 2 weeks was thinner and smaller by 20% after taken out. Tungsten is good for probe tips but cannot be soldered to any metal. Tungsten was our tip of choice, but wires had to be twisted for electrical contact around some part of the tungsten piece the formed the tip.

### 2.3 Emissive probe

An Emissive Langmuir probe[64] directly measures the plasma potential. The probe typically consists of a thoriated tungsten filament heated by an isolated power supply with a low capacitance to ground[65]. The probe is heated to a temperature ( $T_w$ ) such that the electron collection current balances the sum of the emission current and ion saturation current[56]. At this stage the floating potential is roughly  $V_p + kT_e/e$ . The same probe emission level is used across the chamber during a data run. This might cause over-emission near the edge of the plasma in steady state, which has a small effect on the measured floating potential. The error is less than  $T_e/3$ .

The above method only works if  $T_e \gg T_w$ . Marek *et al.*[66] found that the plasma potential determined by the above method can be markedly overestimated if the filament temperature is comparable to the electron temperature. Moreover, when  $T_w \simeq T_e$ , the

probe can cause perturbation by heating the plasma locally. This makes the Emissive probe unable to be used in pulsed operation.  $T_e$  is changing one or two orders of magnitude within 50  $\mu s$ , but the probe tip can only be heated to a defined temperature. The probe over-emits in the low density phase of the pulse, and/or underemits in the high density portion.

The emissive probe is capable of tracking changes in plasma potential below a frequency of 20 MHz. This was verified using a signal generator and an external resistor to simulate the connection resistance to the plasma. The value of the resistor matched  $(dI/dV)^{-1}$  at the floating potential, obtained by sweeping the probe in its emissive state. During the steady state, the RF component of the plasma potential ranges from a few volts to a few tenths of a volt depending on antenna power and probe position.

$V_p$  measured by the Emissive probe is used to calculate the space charge electric field by taking its gradient. Note that this is different from the inductive electric field from the RF coil measured by a magnetic probe (see section 2.6).

## 2.4 Hairpin resonator probe

A hairpin resonator probe was used for spatial and temporal measurement of electron density [67, 68, 69, 70]. This type of probe consists a (typically) quarter-wave resonator immersed in the plasma; its resonance frequency shifts with the plasma dielectric. For an unmagnetized plasma, the permittivity is

$$\frac{\epsilon}{\epsilon_0} = 1 - \frac{f_p^2}{f^2} \quad (2.10)$$

where the plasma frequency  $f_p = \frac{1}{2\pi} \sqrt{\frac{ne^2}{m\epsilon_0}}$ .

When immersed in plasma, the ideal relationship between the probe resonance frequency  $f_r$  and  $f_p$  can be written as

$$f_r^2 = f_0^2 + f_p^2 \quad (2.11)$$

where  $f_0$  is the resonance frequency in vacuum [67].

The hairpin resonator is excited using microwave signals that are coupled using a small loop placed next to the hairpin. A second loop detects the resonant response of the hairpin. The loops are indirectly coupled to the hairpin, so that the entire microwave circuit is isolated from the plasma. The structure is glued together using epoxy. Details about the construction and pictures of the hairpin probe can be found in [70].

The choice of  $f_0$  is closely related to the density range of interest. Propagation of an electromagnetic wave traveling through a non-magnetized plasma is cutoff at a critical density[71]

$$n = m\epsilon_0\omega^2/e^2 \quad (2.12)$$

A larger  $f_0$  is needed to measure a larger  $n$ . However, if  $f_0 \gg f_p$ , then  $f_r \simeq f_0$ . The sensitivity of the probe is limited by the electronics' resolution in this case.

For cheaper and easier use of the hairpin probe, a home made circuit has been developed by Wug *et al.*[72] to replace a Network Analyzer. Details about the analysis and performance of the hairpin probe is included in Appendix B.

## 2.5 Microwave interferometer

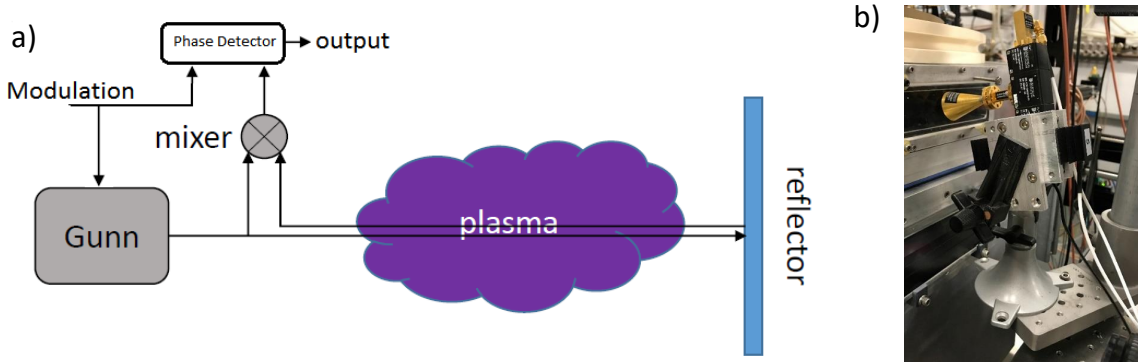


Figure 2.4: (a) Schematic of the microwave circuit and beam passing the plasma (b) Photo of the single horn homodyne interferometer. The beam travels through the center of the plasma and reflects back to the horn from a corner reflector.

Microwave interferometers were used during the course of the experiment as a calibration standard for Langmuir and hairpin probes. We use a homodyne single horn microwave interferometer operating at 60 GHz. Fig. 2.4 (a) shows the schematic and (b) photo of the device pointing towards a window on the chamber. The beam travels through the center of the plasma and reflects back to the horn from a corner reflector. The incident and reflected signal goes to a mixer. The phase shift of the beam inside the plasma is related to electron density by

$$\theta(t) = \frac{\omega}{c} \int_0^L \left( 1 - \sqrt{1 - \frac{n_e(x, t)e^2}{\epsilon_0 m_e \omega^2}} \right) dx \quad (2.13)$$

where  $\omega = 60GHz$  is the frequency of the microwave. In practice, the corner reflector was the wafer platen and the rear wall of the chamber.

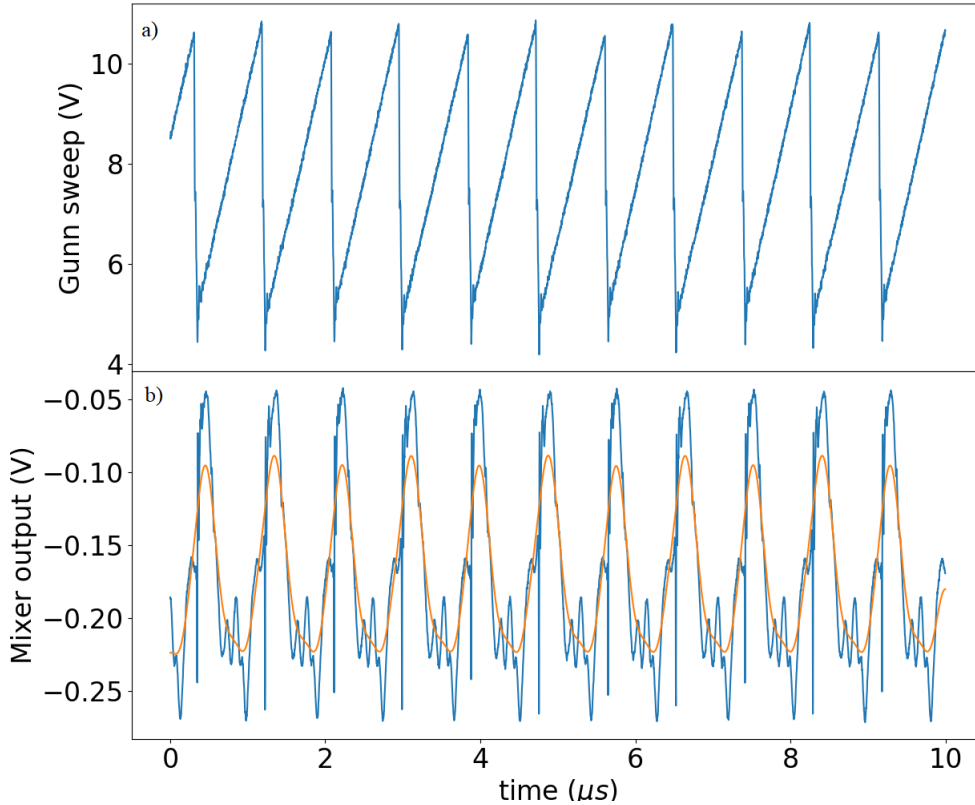


Figure 2.5: Example of (a) Input to the frequency swept Gunn Diode. (b) Original (blue) and Gaussian smoothed (orange) mixer output.

The mixer output contains both phase and amplitude information. To avoid ambiguity caused by this, the Gunn Diode is frequency modulated by  $\sim 1$  MHz. The phase difference between the input frequency scan shown in fig. 2.5 (a) and the mixer output (b) is equivalent to the phase difference of the microwave beam passing the plasma. For a given time series,  $\theta(t)$  can be found by computing the difference between the peak of (a) and (b). Alternatively, one can also integrate the frequency of the orange curve in (b) to get the phase, although this turns out to be fairly inaccurate. The time resolution ( $1 \mu s$ ) of the interferometer is limited by the modulation frequency. A third technique that seems to perform quite well is to compute the phase of the cross spectral density in a sequence of 10-20  $\mu s$  time intervals.

Amplitude of the frequency modulation needs to be calibrated first in vacuum once placed on the machine. The receiving horn and mixer were mounted on a moveable base. When the beam sweep through a  $2\pi$  phase shift (with no plasma), the mixer output should look like a sine wave. For easier use, the Gunn Diode modulator signal and the mixer signal (Fig. 2.5) are passed through a 1 MHz bandpass filters to form the inputs to a RF/IF Gain and Phase detector chip (AD8302). This outputs a voltage which is converted to  $\theta(t)$  using the traces. Note that to get the absolute plasma density, one needs to record a complete rise or decay from plasma to vacuum.

## 2.6 Magnetic probe (B-dot)

Three-axis magnetic probes (Bdot) are used to measure the RF magnetic field[73]. The probe consists three shielded loops orthogonal to each other. By Faraday's law, a changing magnetic field will induce a voltage in the loop:

$$\oint \vec{E} \cdot d\vec{l} = - \int \frac{\partial \vec{B}}{\partial t} \cdot d\vec{A} \quad (2.14)$$

The magnetic field can be found by integrating the signal in time

$$\vec{B} = \int \frac{\partial \vec{B}}{\partial t} dt \quad (2.15)$$

B-dot probe response was calibrated using a Helmholtz coil and a network analyzer. In order to measure signal at 1-15 MHz range, the probe only consists one or two loops for each axis.

As shown in Fig. 2.1, the probe is inserted 13.3 cm above the wafer, 4 cm below the ceramic top lid. For further analysis with computing the plasma current, a coordinate transformation is necessary to convert magnetic field measured by the probe ( $\vec{B}_p$ ) to Cartesian chamber coordinates using the following equations:

$$\begin{aligned} B_x &= -B_{yp}\sin(\phi) + B_{xp}\cos(\theta)\cos(\phi) - B_{zp}\sin(\theta)\cos(\phi) \\ B_y &= B_{yp}\cos(\phi) + B_{xp}\cos(\theta)\sin(\phi) - B_{zp}\sin(\theta)\sin(\phi) \\ B_z &= B_{xp}\sin(\theta) + B_{zp}\cos(\theta) \end{aligned}$$

Here  $\phi = \tan^{-1}(y/x)$  is the azimuthal angle and  $\theta = \tan^{-1}(z/\sqrt{x^2 + y^2})$  is the polar angle. Note that this is the same as converting from Spherical to Cartesian coordinates.

In an ICP, the RF magnetic field induces an electric field which drives an RF current through the plasma. The measured time varying magnetic field reflects this RF current by Ampere's law

$$\nabla \times \vec{B} = \mu_0 \vec{J} \quad (2.16)$$

The fields can have sharp gradients under the antenna. In practice, this means that if a loop pickup 10% of the signal from another direction, a fake current can be inferred, and may be large enough to surpass the real signal. Different construction schemes were implemented in order to optimize the individual Bdot probes against pickup from a second direction. Ideally we also want the smallest plasma perturbation. Details about the probe construction and testing is included in Appendix C.

Fig. 2.6 shows examples of the magnetic field and current computed from Bdot data in steady state plasma at two locations in the chamber. The gradient is calculated using either first or second order finite differences. Note that it is very hard to learn about the current density by studying the time series of magnetic field (or  $dB/dt$ ) at one location

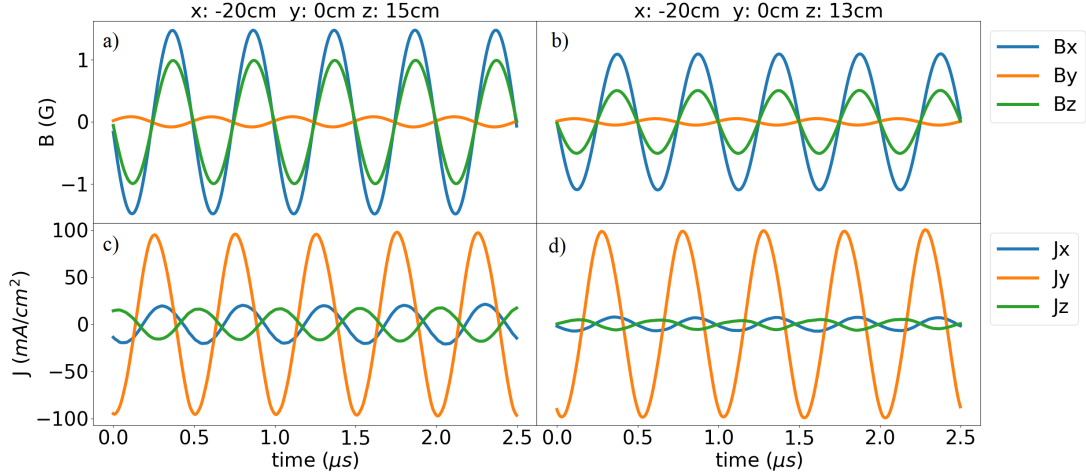


Figure 2.6: Examples of three components of  $\vec{B}$  and  $\vec{J}$  as a function of time at two heights under the antenna. Panel (c) is derived from (a) and its neighboring points by taking the curl using finite difference method. Similarly for panel (b) and (d).

only. In panel (a) and (b),  $B_x$  and  $B_z$  both decreased when the probe moved 2 cm away from the antenna in  $z$  direction. However, the azimuthal current  $J_y$  did not change.

As mentioned in the introduction, previous literature commonly uses two components of the magnetic field ( $B_r$  and  $B_z$ ) to infer the RF electric field and current density [16, 15, 74]. Axial symmetry is of necessity assumed to be true without a volumetric measurement in stove-top ICPs as a confirmation. With a two-loop probe, measurements are frequently only taken at two lines ( $\hat{r}$  and  $\hat{z}$ ) somewhere in the chamber.  $J_\phi$  is calculated on that line correspondingly. This does not produce an accurate  $J_\phi$ . We can see this by comparing  $J_\phi$  calculated from volumetric data to that using a line data of  $B_r$  and  $B_z$  in Fig. 2.7. The offset in the solid lines are a result of non-ideal probe construction (discussed in Appendix C). Nevertheless, neither the magnitude or phase of the signal obtained from sparse data agree with the more accurate volumetric measurement. Furthermore, as shown in the next chapter, the current penetration pattern in an ICP is best to be presented as a 2D contour. It is very hard to study the plasma current with only line measurements.

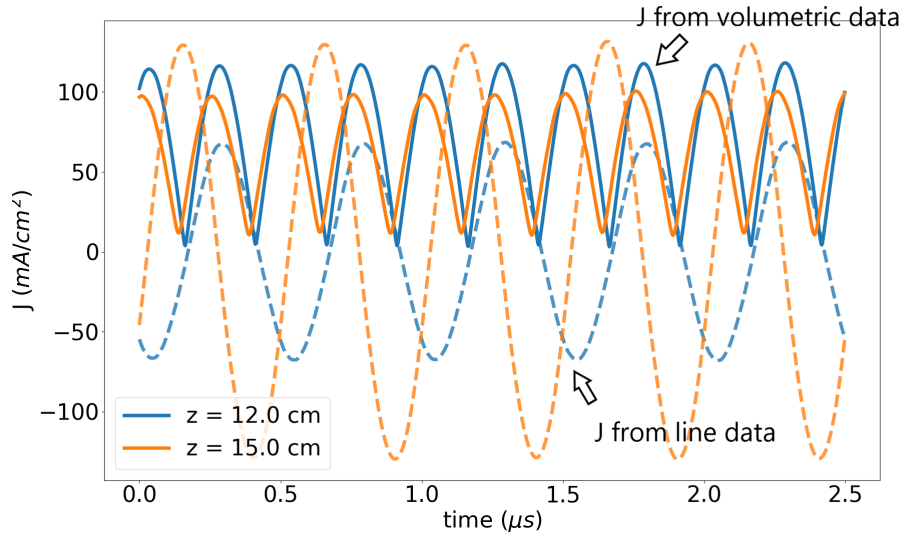


Figure 2.7: Current density versus time at two heights in the machine. The radial position is the same as Fig. 2.6. The solid lines are magnitudes  $|\vec{J}|$  computed using volumetric  $B_x, B_y, B_z$ . The dashed lines are computed from  $B_r$  and  $B_z$  on the  $\hat{z}$  line.

## 2.7 Data acquisition

The data acquisition system (DAQ) utilizes Ethernet communication with different hardware via TCP/IP socket protocol. The DAQ program on the host computer is written in Python. The 3D probe drive consists three EtherNet/IP stepping motor from Applied Motion. The host computer initiates communication by sending a command packet, and the motor responds to that command (if necessary) by sending a response packet back to the host[75]. The linear distance on the probe drive is converted to probe locations inside

the chamber via

$$\begin{aligned}
 r &= \sqrt{x^2 + y^2} \\
 r^* &= \sqrt{x^2 + y^2 + z^2} \\
 x_m &= r^* - x_0 \\
 y_m &= d_0 \frac{y}{x} \\
 z_m &= \pm h_0 \left( 1 - \frac{r}{r^*} - \frac{z^2}{rr^*} \right) + z \frac{\sqrt{d_0^2 + y_m^2}}{r}
 \end{aligned}$$

Here  $x, y, z$  are probe location inside the chamber,  $x_m, y_m, z_m$  are motor linear distance,  $x_0$  is the distance from chamber wall pivot to chamber center,  $d_0$  is the arm length of probe shaft from pivot to end, and  $h_0$  is the height of probe shaft above ground. Uncertainties in measurement of  $d_0, h_0$  and  $x_0$  give rise to the uncertainties in probe locations. In order for the probe tip to move on a straight line, all three motors' speeds are controlled so that for every programmed probe movement, the drives will stop at the same time. This is necessary to avoid the probe tip from scraping nearby chamber walls while passing by. The motors are disabled while recording data to minimize electrostatic noise due to probe holding currents that is otherwise picked up by the signal processing electronics.

An Agilent (now Keysight) waveform generator is used to generate voltage ramps for Langmuir or hairpin probe circuits. The host computer communicates through Ethernet with the function generator, using a set of protocols known as SCPI (Standard Commands for Programmable Instruments)[76]. The output range of the function generator is  $\pm 10$  V into  $1 \text{ M}\Omega$ , which is adequate to directly program the voltage controlled oscillator (VCO) in the hairpin probe circuit. For Langmuir probes, we used an additional  $\times 20$  amplifier on the output for sweeping.

Data is digitized by a Teledyne LeCroy multi-channel oscilloscope (HDO4000A). The host computer communicates with the scope through Ethernet and utilizes National Instrument driver NI-VISA. Data can be saved directly from the scope as binary or ASCII format. In a computer controlled data run, digitized data is saved in HDF5 format. Data sampling rate is chosen with respect to the frequency of interest. For a Langmuir probe,

we allow at least 50 points during the exponential part of the IV curve. For a hairpin probe, output from the I/Q mixer should not be distorted. For a B-dot probe, the sampling rate needs to be at least 500 MS/s for 2 MHz RF. For the interferometer cross-spectral density technique, the sampling rate should be sufficient to accurately resolve the 1 MHz signals.

When the plasma is running in steady state, measurement triggers on the zero-crossing of the antenna current rising edge. Langmuir or hairpin probe sweep voltage ramps are phase locked to the antenna current by the “Qualified Trigger” option on the oscilloscope. A qualified trigger arms on the “A” event, in this case a particular level of the voltage ramp, then triggers on the “B” event which is a zero-crossing of the antenna current. For pulsed operation, the measurement trigger utilized a Stanford delay generator (DG535), which is triggered by the antenna current envelope. Because the RF frequency is feedback controlled, each plasma pulse doesn’t necessarily contain the same number of RF cycles. To construct a data plane with averaging over multiple shots, measurements have to be performed within  $\pm 100\mu s$  of the trigger. If data is taken at times earlier or later than  $100\mu s$ , temporal jitter of a few RF periods will show up. Consequently if we must resolve intra-cycle information, such as  $J_\phi(r, z, t)$ , we segment the data runs by focusing on the time range of interest during one pulse by changing the time interval to the triggered-on cycle using the delay generator.

## CHAPTER 3

### Results and Discussion

Previous studies of ICPs have provided insight into their operation, and established many of the fundamental operating principles. However, in most cases, only a subset of plasma properties have been reported, and rarely in multiple dimensions due to limitations in diagnostics. Advances in diagnostics now enable simultaneous measurements of nearly all plasma and electromagnetic properties of such ICPs in time and space.

With the use of instruments described in the previous chapter, time-resolved and volumetric results of fundamental plasma parameters in an stove-top ICP are presented in this chapter. The goal is to provide new or refined insights to operation of ICPs with a self-consistent set of measurements for electron temperature, ion density, magnetic field and electric field components, Poynting vector flux and power deposition.

#### 3.1 Steady state Argon plasma

Investigations were performed in steady state plasma to develop a fundamental base line for further research as well as test probe performance. The following presented results are measured in pure argon plasma at 10 mTorr with a steady state input power of 300 W. The feedstock gas flow rate is 100 sccm.

Fig. 3.1 shows the time-averaged plasma potential measured with an emissive probe on two orthogonal planes, one perpendicular to the wafer and one parallel to the wafer at a height of 8 cm. The 2 MHz coil frequency was observed on the plasma potential as a 10% ripple, which is produced in part by capacitive coupling and in part by oscillation in

the electron temperature during the RF cycle. The 2D vectors in the plot are the ambipolar electrostatic field computed from  $\vec{E} = -\nabla V_p$ .

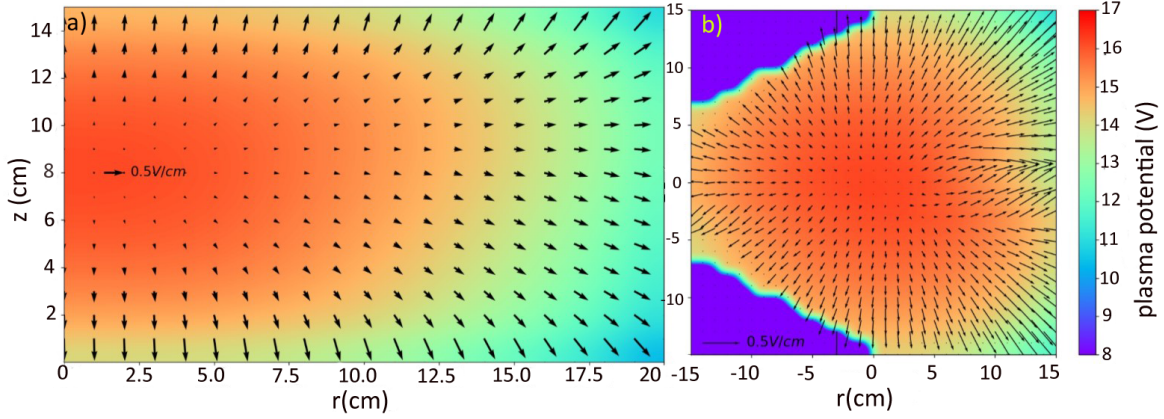


Figure 3.1: Time-averaged plasma potential (shown as flood contours) obtained with an emissive probe and the associated space charge electric field vectors. (a) RZ-plane where  $r=0$  corresponds to the center of the wafer. (b). XY-plane parallel to the wafer at an intermediate height,  $z = 8$  cm. The purple regions are missing data from probe movement limitation.

RF oscillations in  $V_p$  are confined to a region within a few centimeters below the antenna due to plasma shielding. This indicates that IV curves measured from an uncompensated Langmuir probe will not be greatly distorted. We found that  $T_e$  varies  $\pm 0.2$  eV throughout the measurement volume, with an average of 3.0 eV. There was no overall  $T_e$  trend in the spatial profile, which agrees with previous measurements in similar devices using Thompson Scattering[14].

Since  $T_e$  is uniform,  $I_{isat}$  can be used as a fairly accurate representation of density in the chamber when it is calibrated with interferometry. Fig. 3.2 shows  $n_e$ , which peaks in the center of the reactor both radially and vertically. This is contrary to our initial expectation that plasma density would be largest towards the top of the device and under the RF antenna where the inductive field is the strongest, and where most of the power

is deposited in the plasma. Density increases with input power linearly, but the position of peak density is nearly independent of power. Note that unlike plasma potential or electron temperature, density is assumed to be essentially constant over the 2 MHz RF period.

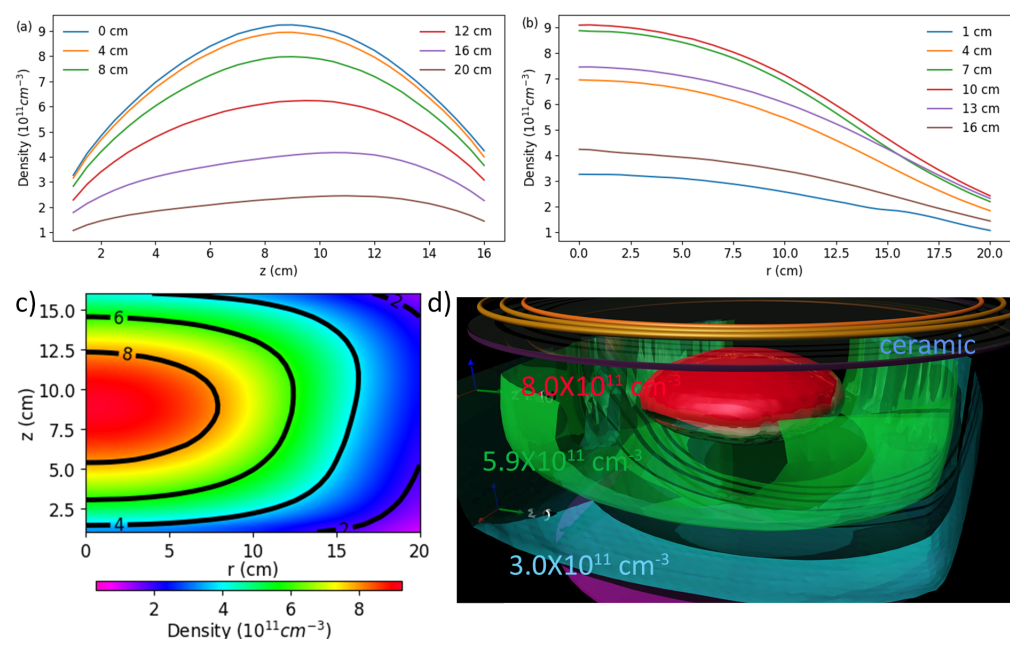


Figure 3.2: Measurements of electron density evaluated from ion saturation current calibrated with interferometer. a) Density as a function of height above the wafer at different radii. b) Density as a function of radius at different heights. c) Density on half of an RZ-plane. d) Three-dimensional density shown as nested isosurfaces. The wafer, antenna, and ceramic top are drawn to scale to guide the eye.

Normal operation of an ICP involves the antenna inductively driving current in the plasma. Fig. 3.3 shows the magnetic field and current computed from that magnetic field at the time of maximum antenna current. Generally the field concentrates a few centimeters below the antenna. The azimuthal currents ( $\tilde{J}_\phi$ ), reversing sign every half-cycle of the 500 ns RF period, are measured to be approximately ten times larger than the radial or axial currents.  $\tilde{J}$  is also  $180^\circ$  out of phase with the antenna current directly under the antenna, as expected from Lenz' law in a good conductor. The missing vectors

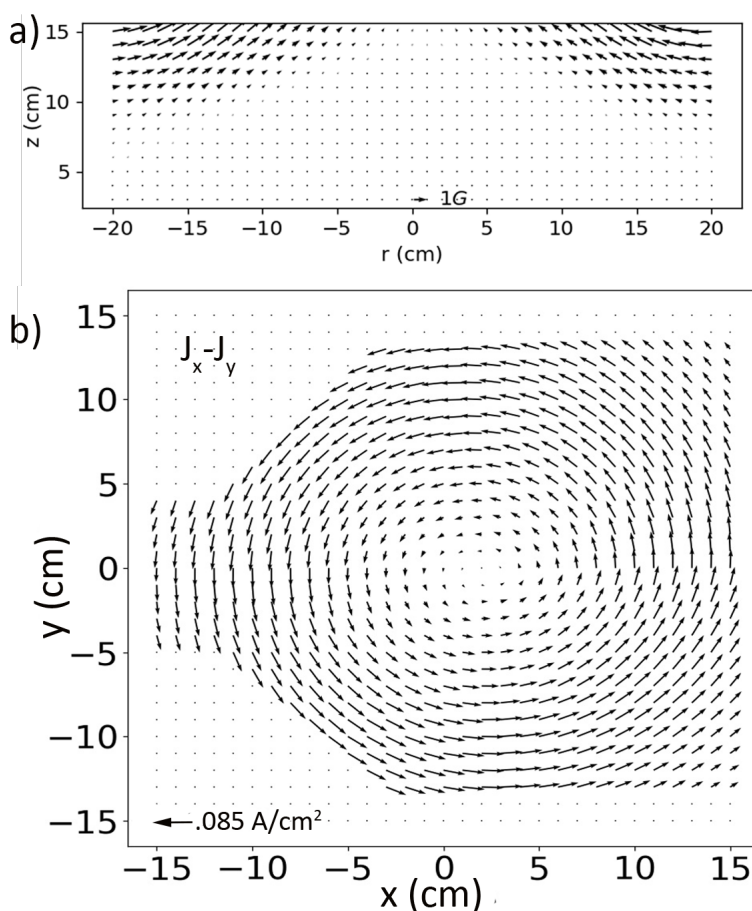


Figure 3.3: 2D vector plot computed from Bdot data at maximum antenna current. (a)  $\vec{B}$  on RZ-plane at the center of the machine. The fiducial arrow represents a magnitude of 1 G. (b)  $\vec{J}$  corresponding to above  $\vec{B}$  on XY-plane 8 cm above the wafer.

on the left hand side of panel (b) reflect spatial positions that cannot be reached by the probe which penetrates the chamber from that side. Note that save for the missing data points the plasma current density is symmetric about the origin – the radial center of the chamber. To overcome the missing data on the left side of Fig. 3.3 (b), data from  $x = 0$  to 15 cm is used, assuming left-right symmetry. This symmetrized data is used to derive the Poynting flux and power dissipation discussed later in this section.

Exploiting cylindrical symmetry, a 2D contour plot of  $\tilde{J}_\phi$  sampling at 3 times during a quarter-cycle of an RF period is shown in Fig. 3.4 on a vertical plane. Panel (a) starts at

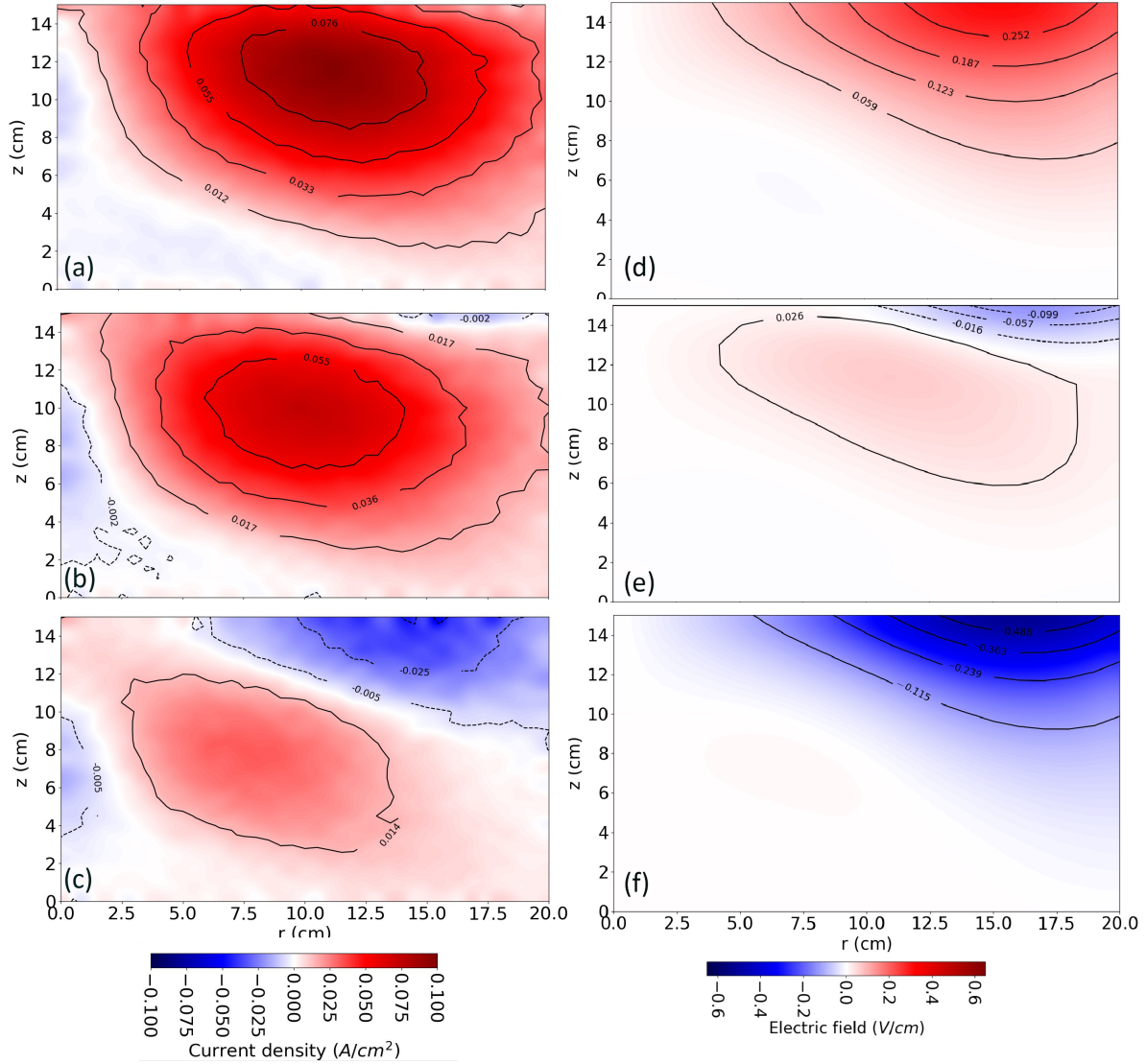


Figure 3.4: (a, b, c)  $\tilde{J}_\phi$  and (d, e, f)  $\tilde{E}_\phi$  calculated from induced magnetic field. The current on the antenna coils has a peak value of 35 A. The three rows from top to bottom correspond to  $t/T_{RF} = 0, 0.125, 0.25$ , respectively. The red and blue colormap correspond to current flowing or electric field pointing into or out of the page.

maximum antenna current with (b) and (c) each 62.5 ns afterwards. The plots illustrate the dynamics of the current penetration into the plasma. The dynamics resemble eddy current penetration into a conductor from an external driving current. Since the internal electric field that drives the current changes sign every half cycle, the plasma current

directly under the coil reverses and gains strength as the previous current maximum decays and moves downwards. This current diffusion pattern was seen by Fayoumi[17] and described as “the Ohmic response of the plasma due to an external driving current”.

The electromagnetic component of the internal electric field ( $\vec{E}_{ind}$ ) is a superposition of the field generated from the alternating antenna current, plasma current, and image currents in the walls. This is separate from the ambipolar electric field (Fig. 3.1). Since there are no appreciable radial or vertical currents,  $\vec{E}_{ind} \simeq \tilde{E}_\phi \hat{\phi}$ .  $E_\phi$  is calculated using Faraday’s law,  $\int \tilde{E}_\phi dr = -\frac{\partial}{\partial t} \int B_z dS$ ,  $E_\phi$  on the vertical plane shown in Fig. 3.4 during a half RF cycle. In contrast to  $J_\phi$ , the peak of which forms below the antenna and moves down and towards the center of the tool, the majority of  $\tilde{E}_\phi$  accumulates under the antenna. The induced electric field in the bulk of the plasma is diminished because of plasma shielding.

For  $T_e \gg T_i$ , the conduction current is driven by electron motion only.

$$\tilde{J} = i\omega\epsilon_0 \left[ 1 - \frac{\omega_{pe}^2}{\omega(\omega - i\nu_{en})} \right] \tilde{E} = (\sigma_p + i\omega\epsilon_0)\tilde{E} \quad (3.1)$$

where  $\omega$  is the driving frequency, and plasma conductivity is given by

$$\sigma_p = \frac{\epsilon_0\omega_{pe}^2}{i\omega + \nu_{en}} = \frac{\epsilon_0\omega_{pe}^2\nu_{en}}{\omega^2 + \nu_{en}^2}(1 - i\omega/\nu_{en}) \quad (3.2)$$

The reactive or inertial component of the plasma conductivity, which is proportional to  $\omega/\nu_{en}$ , introduces a phase delay between the velocity of the electrons (which dominate the current density) and that of the incident electric field. This is observed as a phase difference between  $\tilde{J}_\phi$  and  $\tilde{E}_\phi$ . The finite response time of the electrons to reversals in the electric field can then lead to regions in which the current density actually opposes the incident electric field. This is visible as simultaneous regions of positive and negative current density in Fig. 3.4 (c).

In the limit that  $\omega \gg \nu_{en}$ , the plasma conductivity is dominated by reactance, and electron velocities are 90° out of phase with the incident electric field. In the limit that  $\omega \ll \nu_{en}$ , the plasma conductivity is dominated by resistance, and electron velocities are in phase with the incident field. Fig. 3.5 (a) shows  $\nu_{en}$ <sup>1</sup> as a function of  $T_e$ [77]. For a

---

<sup>1</sup>Collision cross section data from COP database, www.lxcat.net

electron temperature between 3-5 eV, the conductivity has both non-negligible real and imaginary component in the pressure of interest.

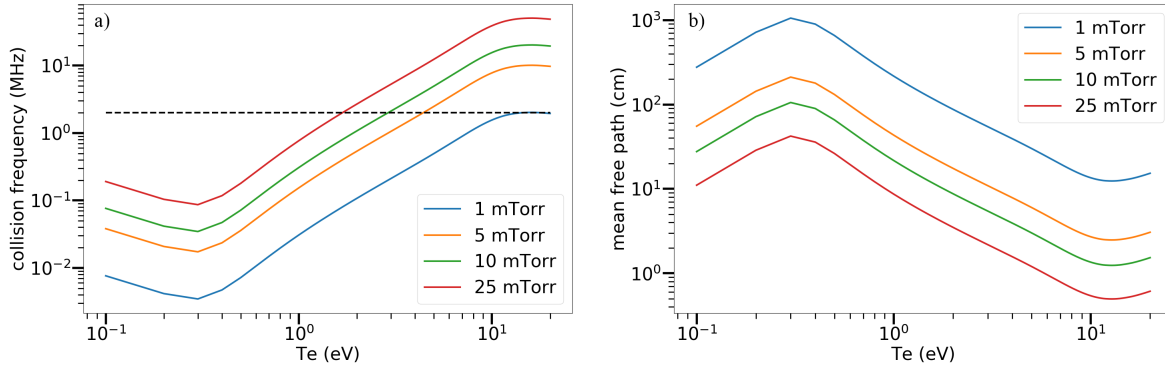


Figure 3.5: (a) Electron neutral (e-n) collision frequency ( $f_{en} = \nu_{en}/2\pi$ ) and (b) mean free path vs electron temperature for pressures of interest. The dashed line on panel (a) is the driving frequency (2 MHz) drawn as reference.

The bulk of the inductive power ( $P = \vec{J} \cdot \vec{E} = \tilde{J}_\phi \tilde{E}_\phi$ ) is localized almost directly under the coil as this is where the image current from the coil is largest. The time averaged power density inside the plasma is shown in Fig. 3.6 (calculated from data shown in Fig. 3.4). The power is deposited closer and closer to the antenna as the neutral pressure is increased. This is related to the shorter mean free path for fast electrons as shown in Fig. 3.5 (b).

The computed volumetric power density is integrated over the volume to estimate the total inductive power dissipated in the plasma. Separately, resistive losses due to currents flowing in the various conductors were estimated by measuring the generator power required to drive corresponding equivalent coil currents with the chamber evacuated (that is, no plasma). The resistive losses are manifested primarily in coil heating and account for 10-13% of the generator power. Limited by the probe drive system, the measurable volume of the ohmic power in the experiment does not cover the entire plasma volume. To estimate the total power, we rescaled the measured volume by examining a model of the plasma described in [46]. The fraction of power inside the experiment view-window is about 70% of the total inductive power.

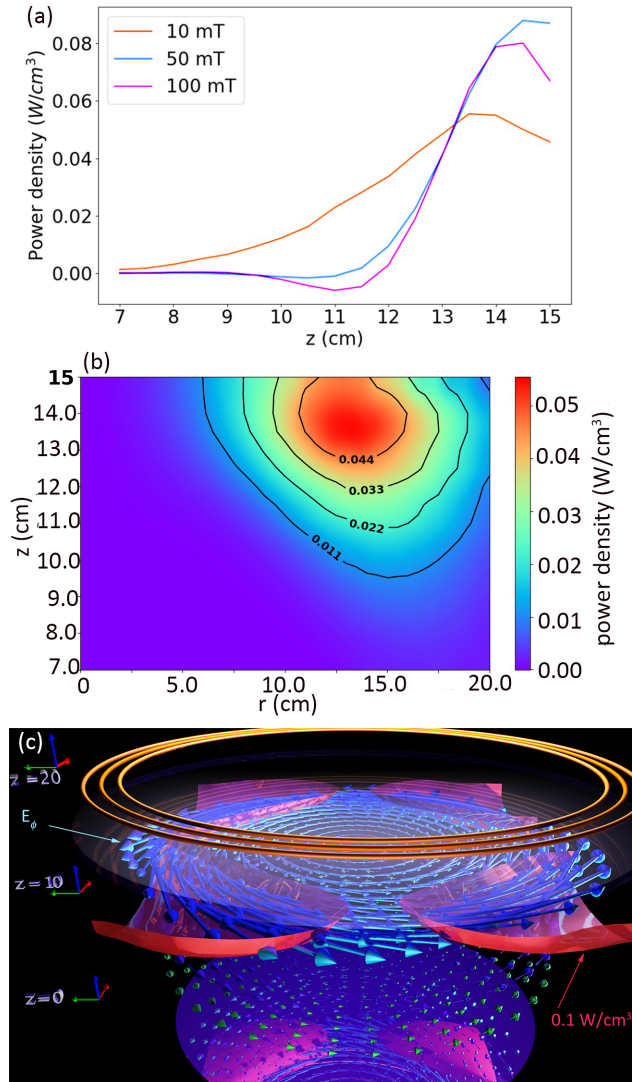


Figure 3.6: Inductive power derived from the measured B field. The power shown here is time averaged over one RF cycle. (a) Line-out along z direction taken through the location of maximum power absorption for different pressures: 10 mT (blue), 50 mT (yellow), and 100 mT (green). As pressure increases, the power deposition gathers even closer around the antenna. (b) 2D contour of power density with the center of the wafer at  $r = 0$  and  $z = 0$ . (c) 3D iso-surface of power (red). This frame shows a snapshot at the time when power absorption is maximum. The vectors are electric field at three different height above the wafer ( $z = 6, 9, 14$  cm).

Generator power (W)	80	300	500	800
Antenna resistive loss (W)	35.1	42.1	70.2	96.5
Experimental $J_\phi E_\phi$ (W)	24.6	138.5	194.7	291.2
Fraction of power inside view-window	0.782	0.710	0.657	0.619
Renormalized power (W)	31.4	195.1	296.4	470.5
10% Capacitive (W)	8	30	50	80
Total renormalized power (W)	74.5	267.2	416.6	647.0
Power accounted for (%)	93.1	89.1	83.3	80.9

Table 3.1: Power deposition computed as the volume integral of  $\vec{J} \cdot \vec{E}$  with recalibration by the model to account for unobserved volumes of the reactor and coil resistive losses as a function of generator power for Argon plasmas at 10 mTorr. The renormalized power is the experimental power divided by fraction of power inside the view window.

As shown in Table 3.1, an input power of 300 W on the antenna contributes roughly 40 W of resistive loss. The total power integrated from the measured volume is 140 W. Accounting for the volume not covered by probe measurement, the total inductive power is roughly 200 W. There is an unaccounted for power deposition of 100 W or about 30 %. We expect that some fraction of the missing power is absorbed by the plasma through capacitive coupling. As stated above, oscillations in plasma potential were measured using an emissive probe. We estimate the power density from capacitive coupling in the volume of the plasma by  $P = \sigma_p \tilde{E}^2$ , where  $\tilde{E}$  is calculated from the RF fluctuation in  $V_p$ . This is estimated to be about 10 W. Measurements could not be performed in the sheath directly under the coil, which accounts for additional power dissipation by ion acceleration by capacitive electric fields from the coil. Based on results from simulation[46], we estimate the loss due to ion acceleration under the coil to be about 20 W, which produces a total of about 30 W. For the rest of the entries in the table, we estimated capacitive losses as 10% of the generator power. With the uncertainty in the measurements of about 5%–10%, the majority of power deposition can be accounted for.

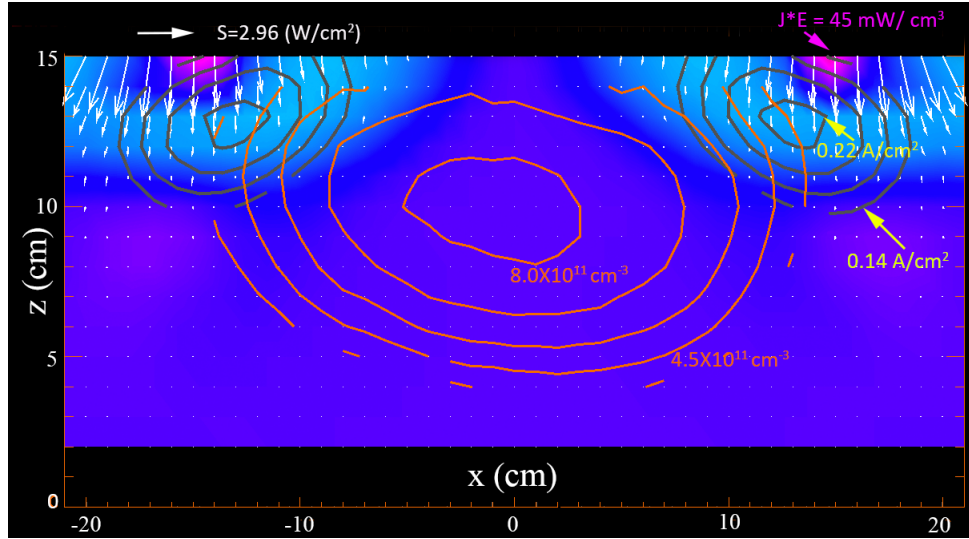


Figure 3.7: Contours of plasma density (red), shaded contours of inductive power, Poynting vector (white arrows) and the plasma current density (grey contours). Values are shown for an Ar pressure of 10 mTorr and generator power of 300 W.

The magnetic and electric field data can be combined to compute the Poynting flux,  $\vec{S} = 1/\mu_0 \vec{E} \times \vec{B}$ . Fig. 3.7 is a composite of the experimentally measured plasma density, current density, Poynting flux and inductive power during steady state operation. Except for the current density which is shown as a peak value, these quantities are averaged over an RF cycle. The Poynting flux originates at the coils and points towards the power deposition region. The plasma density is largest in the center of the chamber and does not coincide with the plasma current density (grey contours above the red density contours), or the peak power deposition.

One would expect the maximum plasma density to be localized closer to the region of power deposition, as this would represent a plasma source region. The measurement results suggest either convective non-collisional transport of electrons in the tail of the distribution or rapid thermal conduction, both of which will more uniformly distribute ionization throughout the reactor. Given a uniform volumetric ionization source, a density profile peaked in the middle of the chamber solves the diffusion equation with a plasma sink at the chamber wall[78].

The space charge field derived from  $V_p$  points away from the center where density is a maximum. From the momentum transfer equation, the divergence of the pressure gives the change of momentum flux due to spatial inhomogeneities. Since  $T_e$  is nearly spatially uniform, this inhomogeneity arises from gradients in charge density. The uniformity of  $T_e$  indicates a high electron thermal conductivity, since measured power deposition is highly non-uniform.

Volumetric measurements demonstrate and confirm azimuthal symmetry in a cylindrical stove top ICP, symmetries that previously were assumed to apply. Plasma current peaks slightly inwards underneath the antenna, and the peak current density propagates downwards. The fact that the current does not penetrate vertically downward in a straight line is due to a non-uniform plasma conductivity.

### 3.2 Pulsed Argon plasma

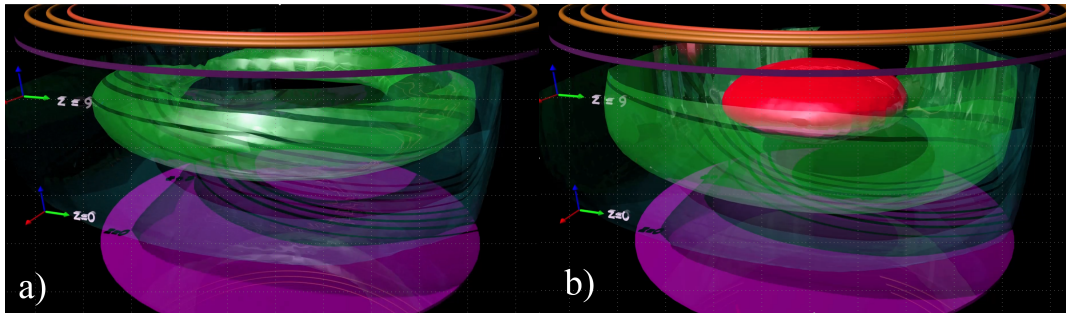


Figure 3.8: Examples of the two types of density profile as 3D iso-surfaces. Although the two plots in particular are extracted from an  $I_{isat}$  during the plasma breakdown, panel (a) can be acquired at low power and/or high pressure CW operation, and panel (b) at other CW conditions. The green and red iso-surface can therefore have any density value between  $10^8 - 10^{12} cm^{-3}$  depending on the situation.

In pure Argon (steady state or pulsed), the plasma density profile can be generalized into two types: a “ring” shape profile under the ceramic top, and a “bun” shape profile that peaks in the center of the chamber both radially and vertically. Fig. 3.8 shows ex-

amples of each profile as 3D iso-surfaces. There are two situations in steady state where the density forms a “ring” under the antenna: (1). at very low power (< 50 W) or when the plasma is breaking down (2). at very high pressure (> 50 mTorr). In the first case, the inductive field looks very similar to that in vacuum, since there are not many particles. Because an inductive current is unable to form, power is coupled to the plasma capacitively. The field is highly concentrated near the antenna, plasma is also concentrated near the top of the chamber. In the second case, small electron-neutral collision mean free path associate with high neutral pressure causes fast electrons to be localized near where they originated. On the contrary, for the density to peak in the middle of the chamber, ionization needs to be relatively uniform (or proportional to  $n_e$ ).

Fig. 3.8 is derived from an  $I_{isat}$  time evolution of the initial plasma break down from neutral gas. This matches the density evolution in general as shown later in the section. During pulsed operation, evolution close to Fig. 3.8 can occur at the beginning of each plasma shot. However, certain pulsed conditions can skip the stage in Fig. 3.8 (a). The following results are presented to illustrate and explain various processes in a pulsed plasma, especially during the E-H transition at the beginning of a repeating pulse. Unless otherwise noted, data is taken in Argon with 1 kHz repetition rate and 50% duty cycle. The fill pressure is either 5 or 25 mTorr.

Fig. 3.9 shows the initial breakdown and final shut off of the 1 kHz plasma source at 25 mTorr. Panel (a) shows that it takes about 7 pulses for the plasma to reach a quasi-steady state. This is partially limited by the rise time of antenna power itself, and partially by the ionization balancing diffusion. The overshoot in visible light signal and antenna power on the first shot, is identified as a signature for E-H transition by previous researchers[40, 79, 80] (Discussion on E-H transition is included in section 3.3).

Panel (b) shows the development after the plasma is completely shut off. The visible light signal is created by neutral argon excited states generated by electron bombardment at certain atomic energy levels. The rapid decay in light is coupled to the rapid disappearance of warm electrons. The diffusion coefficient  $D_\alpha = kT_\alpha/m_\alpha\nu_\alpha$  decreases with

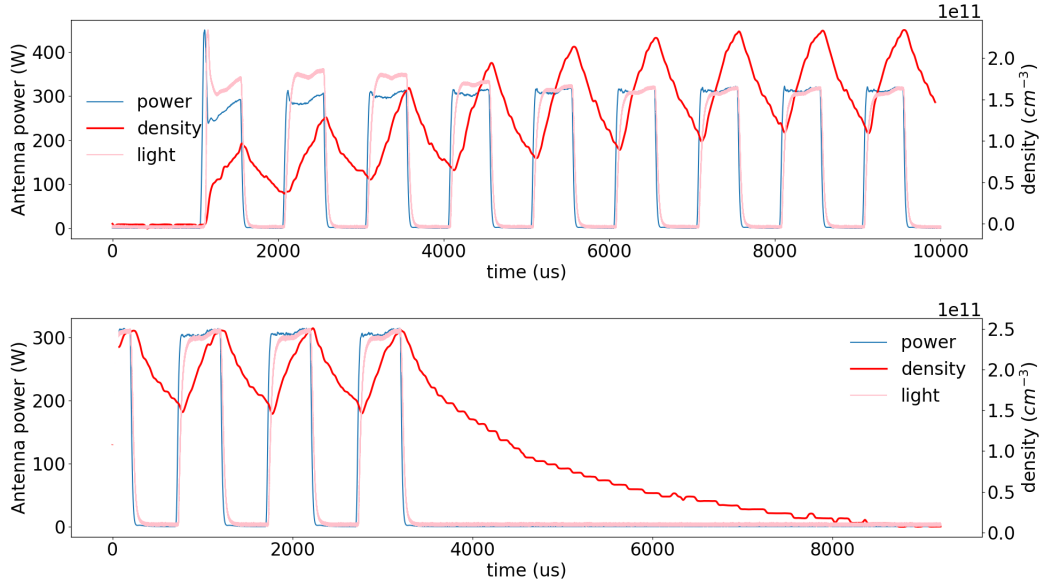


Figure 3.9: Antenna power, visible light and plasma density measured by the interferometer at (a) initial breakdown and (b) final shut off of the source. The blue curve corresponds to the vertical axis on the left and the red curve reads that on the right. The visible light signal is acquired with a diode.

temperature, making the plasma density decay slower than  $T_e$  in the afterglow. Note that in the 5 mTorr case the density will decay faster than 25 mTorr (as well as reach steady state faster) from the difference in the collision frequency.

Fig. 3.10 shows the electron density for one pulse cycle superimposed on antenna current and RF power input.  $n_e$  rises faster in the 5 mTorr case and is observed to saturate within the 0.5 ms active glow period, whereas at 25 mTorr it does not. Note that the 25 mTorr case eventually saturates if we increase the active-glow time to longer than 2 ms. When the density stops changing in these pulsed plasmas, the spatial distribution looks the same as in steady state. Note that from the antenna current in Fig. 3.10, one might assume that the input RF power is non-zero even later in the afterglow. However, the generator voltage is close to  $90^\circ$  out of phase with the current at that time resulting in negligible RF power.

After the RF is turned on in the beginning of the active glow, an interesting phe-

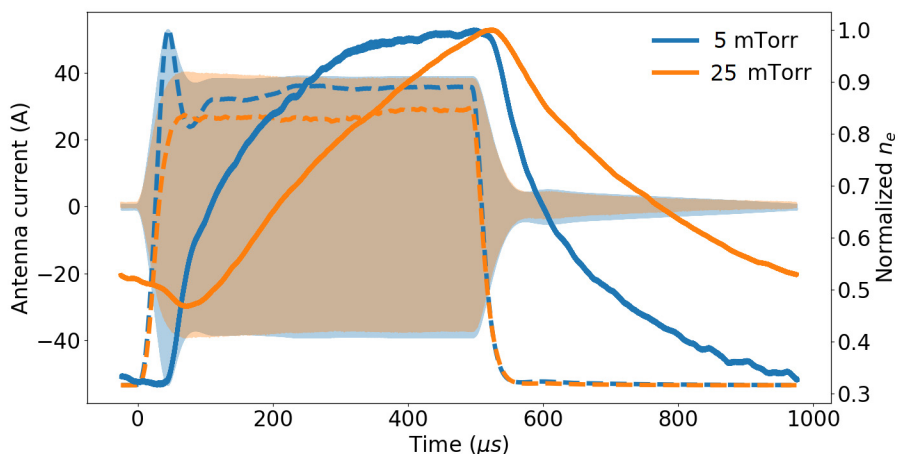


Figure 3.10: Time evolution of plasma density (solid lines) for one pulse cycle measured by the interferometer, where blue corresponds to the 5 mTorr case, and orange corresponds to 25 mTorr. The fainter background shows the antenna current oscillating at 2 MHz for both pressures. The dashed lines are RF power input at the antenna. In this case, the antenna currents were set to be approximately equal for both pressures, which results in slight differences of RF voltage and power. Solid lines are  $n_e$  measured by the interferometer normalized to unity at their maximum. The peak densities for 5 and 25 mTorr are  $4.6 \times 10^{10} \text{ cm}^{-3}$  and  $2.85 \times 10^{11} \text{ cm}^{-3}$ , respectively.

phenomenon is that  $n_e$  continues to drop. In fact, the density decay rate *increases* (at 25 mTorr) despite this being the powered phase of the pulse. We observed this phenomenon on three separate density diagnostics (Fig. 3.11). We explain it as follows: when RF is turned on initially, residual plasma from the previous pulse is heated up by the input power to the plasma. Based on Langmuir probe measurements,  $T_e$  rises before there is significant ionization. The  $T_e$  increase in turn results in increased ambipolar diffusion and consequently increased flux to the wall. This is consistent with emissive probe measurements—the drop in  $n_e$  occurs simultaneously with a rise in  $V_p$ . A similar density decay is described by Lee *et al.*[81] and Sobolewski *et al.*[82] for a step turn-on of the RF *bias* power on the chuck during steady state inductively coupled plasma operation. They explained this respectively with power balance arguments and a hypothesis about impurities on the wafer.

We propose that their results are due to a similar mechanism when total power input to the system is increased.

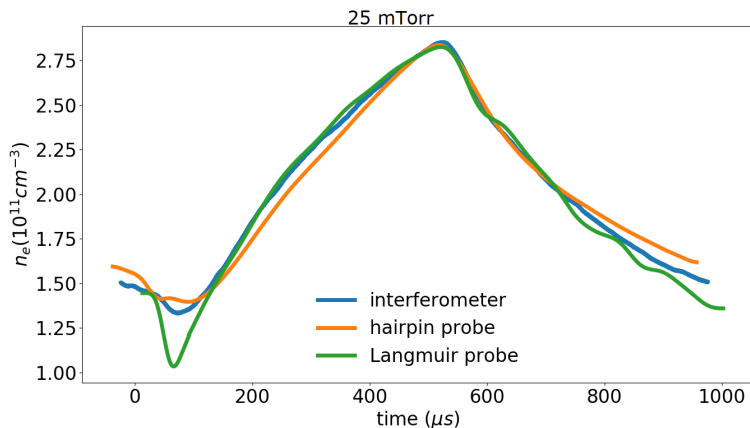


Figure 3.11: Electron density evolution for one plasma cycle from three different diagnostics. The plasma is pulsed at 1 kHz with 50% duty cycle, with 300 W peak power and sustained in 25 mTorr Argon. The probe results are line averaged through the center of the machine.

Fig. 3.11 shows a comparison between three diagnostics for  $n_e$ . The hairpin and Langmuir traces are derived by moving the probe along the diameter of the chamber and averaging a sequence of 26 measurements to get line-averaged values. The density derived from the hairpin probe has been corrected based on the method described in Appendix B. The Langmuir probe value is multiplied by a factor of 2.9. Of the three diagnostics, the Langmuir probe has the worst signal to noise ratio; this becomes more apparent as it deviates from the others in the late afterglow.

In the beginning of the pulse, the Langmuir probe shows a bigger dip compared to the other two diagnostics. This is a combined affect from a bigger plasma sheath depleting local plasma, and possibly insufficient probe compensation[59].

Fig. 3.12 shows a Langmuir probe measurement at the center of the chamber for 25 mTorr. In the afterglow, the RF power takes about 50  $\mu s$  to decay to zero, which contributes to some delay to the temperature drop. If RF power was shut off instantaneously,

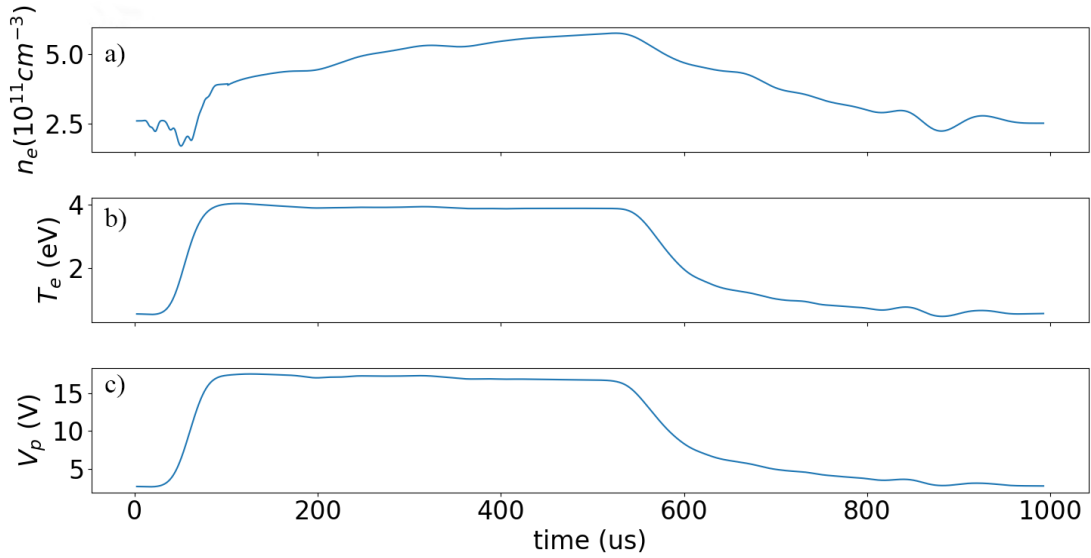


Figure 3.12: Langmuir probe measurement results at the center of the chamber for 25 mTorr.  $n_e$  in panel (a) and  $T_e$  in panel (b) are derived from the EEDF, and  $V_p$  in panel (c) is defined as the maximum of  $\frac{dI}{dV}$ . Noise in these signals is primarily due to uncertainties in determining the precise plasma potential in the stepped Langmuir probe characteristic.

we expect the  $T_e$  decay rate to more closely follow a solution to a diffusion equation with no sources, i.e. with a much shorter time constant ( $\leq 10\mu s$ ). The  $n_e$  decay rate is always much slower than  $T_e$  decay rate. During the active glow period,  $T_e$  time evolution is similar for different spatial locations.  $T_e$  for 5 mTorr is roughly 1 eV higher than 25 mTorr, as a consequence of the same power input being distributed among fewer particles. This has been predicted by Subramonium and Kushner[28]. They further state that phenomenologically it is “a consequence of the need of larger ionization rates to balance larger diffusion loss”.

Prior to the start of the next shot, there is some residual plasma from the previously powered portion. Examining the EEDF (acquired from a planer Langmuir probe), each plasma pulse cycle begins with the heating of these electrons as soon as RF power is applied. Fig. 3.13 illustrates this process. We identify the maximum of the first derivative of the IV curve ( $dI/dV$ ) as the plasma potential  $V_p$ , and the corresponding voltage increases

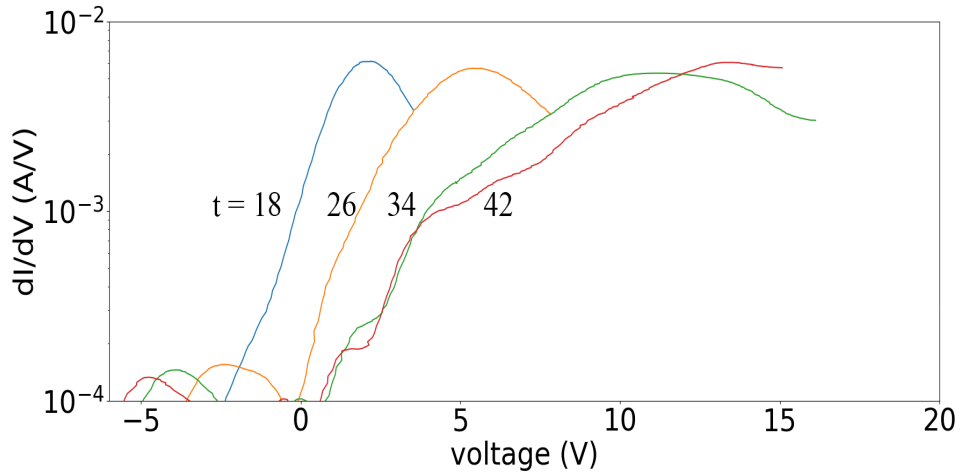


Figure 3.13: First derivative of the Langmuir probe IV characteristic (proportional to EEDF) in center of the chamber at 25 mTorr. The traces are  $8 \mu s$  apart.

with time after the turn-on. From equation 2.5, the 1D EEDF from a planer probe is proportional to  $dI/dV$  up to  $V_p$ . During this earliest part of the powered phase, low energy electrons shift to higher energies in velocity space as they are heated. At the same time, the area under the curve stays nearly constant, indicating no net density increase.

The plasma behavior in the afterglow at both 5 and 25 mTorr follows classical ambipolar diffusion. EEDF evolution in the afterglow looks like a time reversed version of the active-glow evolution. Immediately after the active-glow ends, electrons begin to cool and the peak of the EEDF increases as electrons migrate to lower energies in velocity space. This happens faster at lower neutral pressure. This EEDF evolution matches descriptions in the literature[35, 34] and is not shown here.

Electron density evolution is shown in Fig. 3.14. Lieberman[78] has modeled the plasma decay with a simple 1D diffusion equation; this accurately reproduces the observed profile at later times. In Lieberman's analysis,  $n_e \propto e^{-t/\tau}$  with  $\tau \propto 1/T_e$ . In the first  $50 \mu s$  of the afterglow, electrons are still hot.  $T_e$  decays spatially non-uniformly and redistributes the density. At later times, the electrons are cold ( $T_e \leq 0.2$  eV) and  $\tau$  becomes a constant, and  $n_e$  decays without changing the spatial dependence of the profile. In the

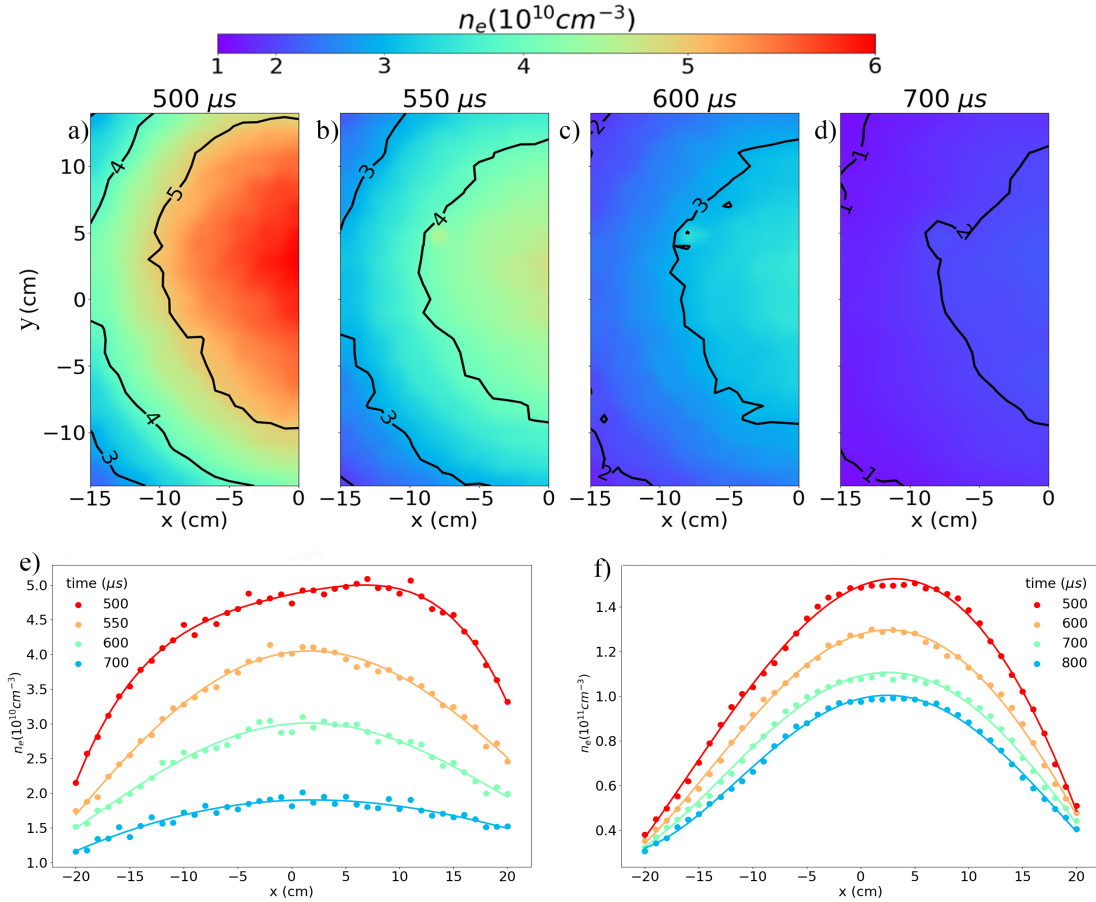


Figure 3.14: Electron density in the afterglow measured by a hairpin probe. RF on the antenna begins to drop at  $t = 500 \mu\text{s}$ . (a)-(d) are XY-plane ( $z = 12 \text{ cm}$ ) contours taken at 5 mTorr. (e)-(f) are lineouts taken at 5 mTorr and 25 mTorr respectively.

late afterglow just before the beginning of the next RF power pulse,  $n_e$  at 5 mTorr is 10 times lower than that of the 25 mTorr case. The difference in plasma density plays an important role in the initial behavior of the next active-glow phase.

Electron density evolution in the active-glow is shown in Fig. 3.15. After the RF turns on at  $t = 0$ ,  $n_e$  continues to drop for  $30 \mu\text{s}$ . It then starts to grow into a “ring” shape for 5 mTorr (panel a, b). The ring shape profile is most pronounced between 75 and 125  $\mu\text{s}$ . Density fills in and evolves towards peaking in the middle after 125  $\mu\text{s}$ . The evolution of 100 W peak input power vs 300 W is almost identical, with the peak profile more uniform in the higher power case.

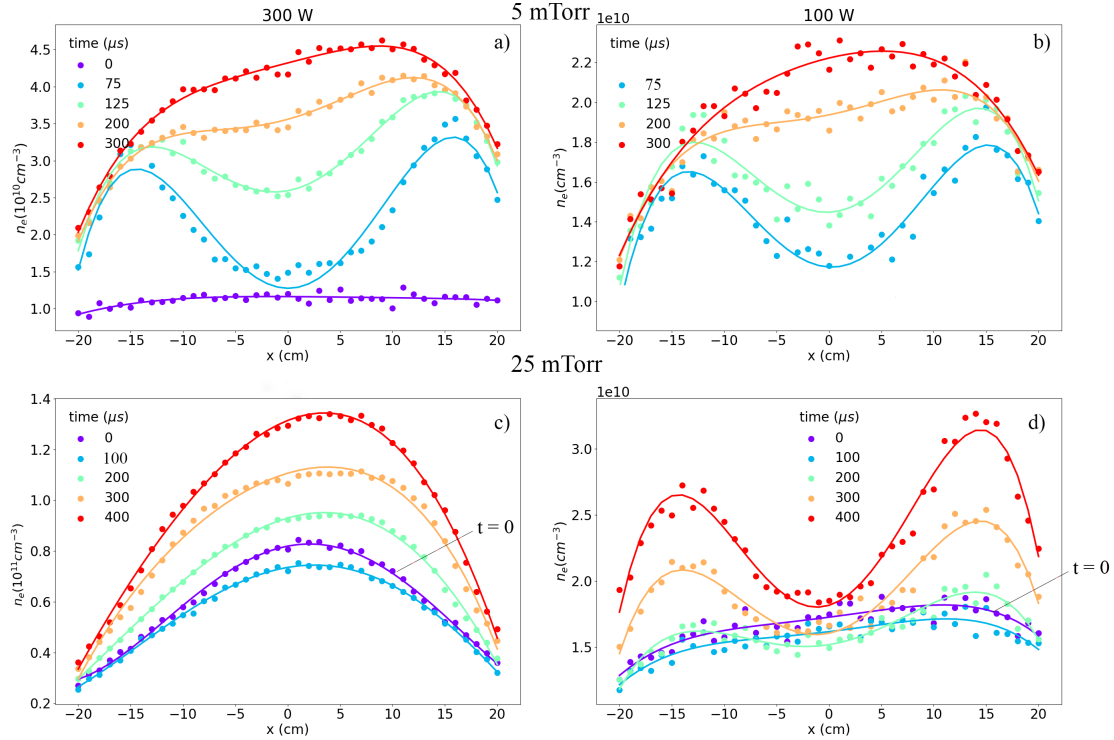


Figure 3.15: Electron density in the active-glow measured by a hairpin probe at  $z = 12$  cm with 5 mTorr (a, b) and 25 mTorr (c, d) fill pressure. The peak antenna power is 300 W for (a, c) and 100 W for (b, d). The data points are fitted to guide the eye. In panel (b) the  $t = 0$  profile is missing because the hairpin probe was unable to resolve the density structure well. In panel (a, b), the line-out at  $75 \mu s$  is at the time of the most hollow density profile, and in panel (c, d)  $100 \mu s$  corresponds to the minimum density over the whole pulse (instead of  $t = 0$ ).

The spatial distribution of  $n_e$  at 25 mTorr is very different. For a input power of 300 W, density always peaks in the middle of the chamber (Fig. 3.15 c). Between 0 to  $100 \mu s$ , there exists a drop in  $n_e$  as discussed above. We attribute the density pump-out to increased ambipolar diffusion due to increased  $T_e$  at the beginning of the powered phase of the plasma. Compared to the 5 mTorr 300 W case (Fig. 3.15 a), the left-over density from the previous shot is lower; as a consequence power is distributed among fewer particles. With a higher ionization rate, the generation of new particles balanced the loss faster in

the 5 mTorr case.

The 25 mTorr profile for 100W input power always forms a “ring” shape throughout the active-glow (Fig. 3.15 d). Similar to 25 mTorr 300 W (Fig. 3.15 c), there is a density drop from 0 to 100  $\mu s$ . However, with a lower starting density, the ionization is localized under the antenna instead of following the electron density (provided the loss mechanism is similar in both cases). Compare this to 5 mTorr 100 W (Fig. 3.15 b) where  $n_e$  peaks in the middle after 200  $\mu s$ , the profile of 25 mTorr remains as a ring shape until the end of the discharge (Fig. 3.15 d). As discussed in the beginning of this section, there are two cause for density to form a “ring” shape under the antenna—low power or small mean free path. At 5 mTorr, density localized under the antenna is unlikely due to small mean free path. For the 25 mTorr 100 W case, the “ring” profiles at 200, 300, and 400  $\mu s$  are likely a result of both. With the same amount of neutral particles, the collision mean free path stays the same for energetic electrons, yet 25 mTorr 100 W and 300 W produce different profiles during the discharge.

Another observation from Fig. 3.15 is an asymmetry in the transverse (radial) direction. We suspect this is a combination of two different effects: 1. Asymmetric gas flow in the chamber—noting that the gas inlet is located on the side of the chamber, at  $x = -25$  cm,  $y = 0$  cm,  $z = 2$  cm. 2. Probe perturbation. The spatial asymmetry of  $n_e$  is more pronounced than that of  $V_p$ . The effect of gas flow on asymmetry is discussed in Appendix D. The asymmetry in  $n_e$  leads to an asymmetry in plasma conductivity, which results in asymmetric power deposition as well.

For each 2 MHz RF cycle, an induced current channel is generated closer to the ceramic top and propagates downward and inward. Fig. 3.16 shows the time evolution of  $J_\phi$  as half RF cycles during different times of the pulsed discharge at 25 mTorr.

From 0 to 50  $\mu s$ , the envelope of the 2 MHz RF drive on the antenna ramps up. During this time,  $J_\phi$  concentrates near the antenna first, then broadens and fills more of the volume. Simultaneously,  $n_e$  is relatively constant in time with a profile that peaks in the middle (Fig. 3.15).  $T_e$  rises rapidly (0.1  $\rightarrow$  3.5 eV) throughout the chamber. According to

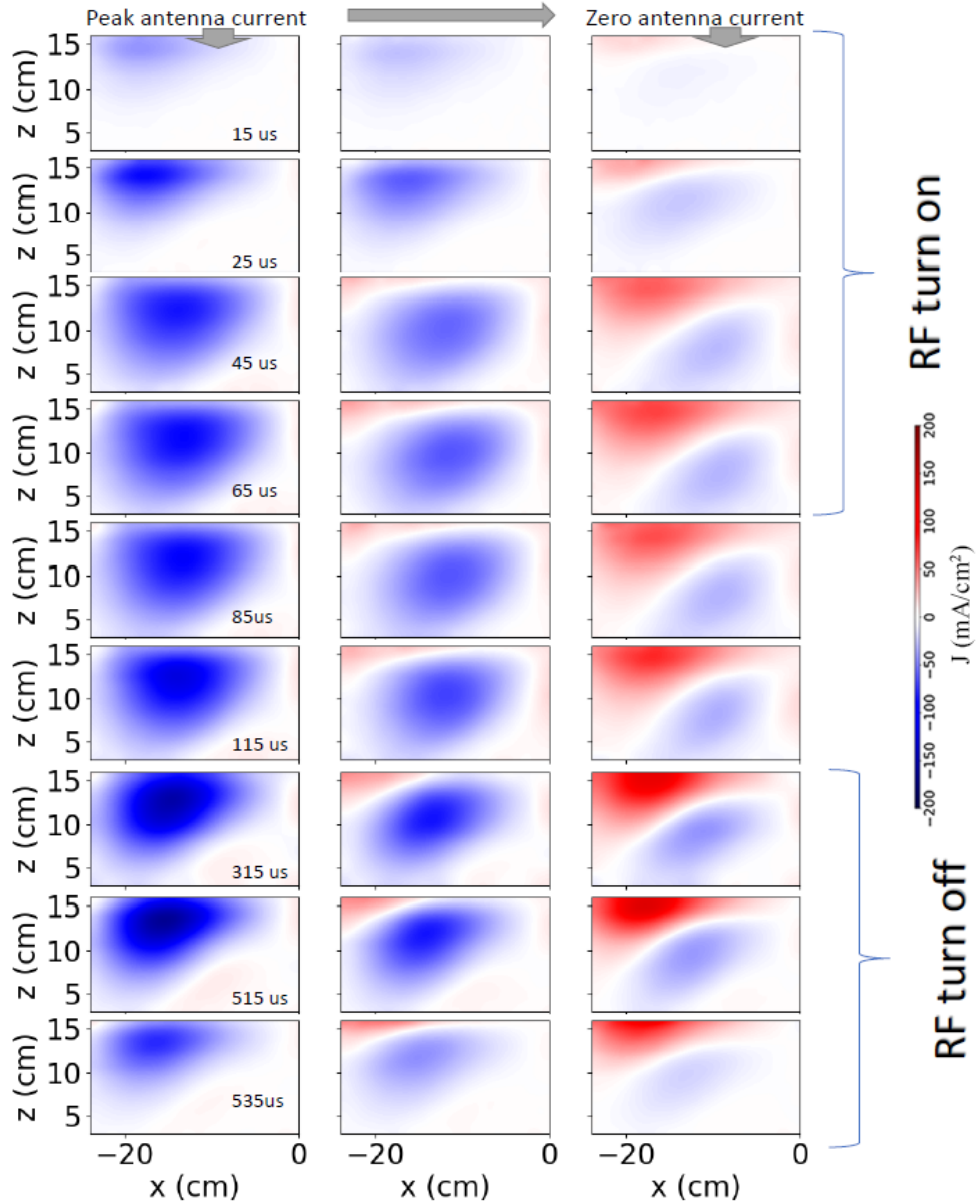


Figure 3.16: Time evolution of the current density profile. Frames in the first column are taken at a local antenna current peak at the respective indicated times. Frames in the third column are taken at a phase  $\pi/2$  later, i.e. when the antenna current is zero. At this time  $dI/dt$  of the antenna current is maximum in the reverse direction, so the reverse current is just beginning to appear. The middle column of contours is at an intermediate time between.

equation 3.2, the plasma conductivity depends on  $\omega/\nu_{en}$ . At 25 mTorr, the rise in  $T_e$  shifts the plasma from reactance dominated ( $\omega > \nu_{en}$ ) to resistance dominated ( $\omega < \nu_{en}$ ). Note that the spatial profile of conductivity matches that of  $n_e$ , which peaks in the middle of the chamber.

Between 50 and 100  $\mu s$ ,  $T_e$  and  $n_e$  are relatively constant. The  $J_\phi$  profile remains the same as a result of no significant change in conductivity. After 100  $\mu s$ ,  $n_e$  begins to increase and  $T_e$  stops changing.  $J_\phi$  propagates a shorter distance into the plasma as a result of higher conductivity. After 500  $\mu s$ , the reverse happens with  $J_\phi$  as a result of rapid cooling in  $T_e$ , until there is no more current on the antenna.

### 3.3 E-H transition

“Inductively coupled plasmas” are not driven by inductively coupled power alone. At low RF input power and low electron density, electron heating and ionization are dominated by the electrostatic field produced below the high side electrical connections and windings of the antenna. This discharge mode is termed “E-mode”. As density increases, electrostatic fields cannot easily penetrate the plasma, and the dominant coupling of antenna power to the electrons occurs more through currents induced by the changing magnetic field instead. At this point, the plasma is said to be in “H-mode”.

As described in section 3.1, with Bdot data and a symmetry argument, we are able to identify the amount of power coupled inductively  $P_{ind} = \int J_\phi E_\phi dV$  and capacitively  $P_{cap} = P_{tot} - P_{ind} - P_{loss}$ , where  $P_{tot}$  is the input power and  $P_{loss}$  is power loss on the antenna and other circuit elements. The evolution of inductive power over half of an RF cycle during pulsed operation is shown for 25 mTorr in Fig. 3.17 (a) at 25 and 45  $\mu s$ . The power is deposited a few centimeters lower at 45  $\mu s$ . The power deposition retains approximately the same spatial distribution from 50  $\mu s$  until the end of the discharge (which is essentially identical to the steady state profile). Panel (b) shows the total power deposited inductively in the volume. When the antenna current just begins to rise at  $t=0$ ,

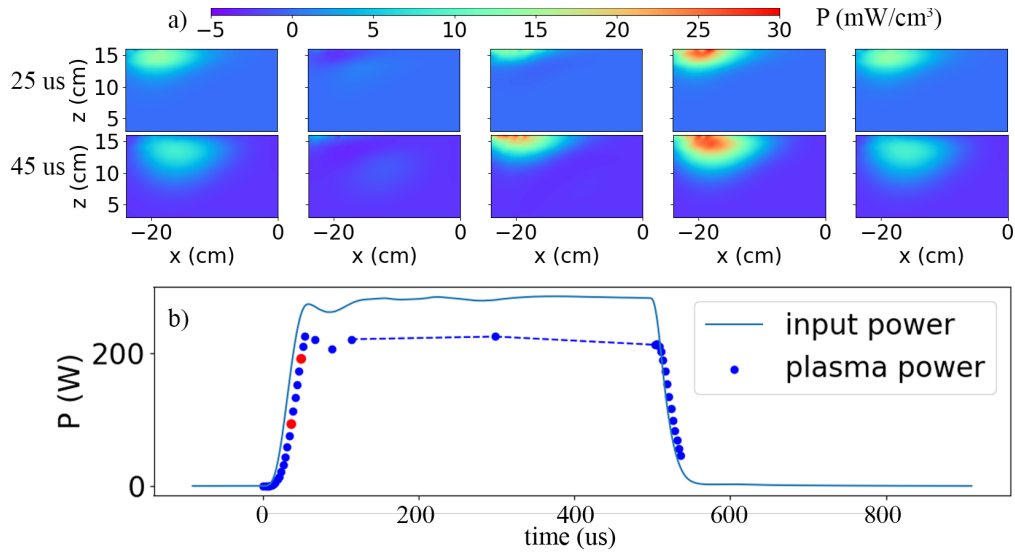


Figure 3.17: (a) 2D contours (antenna located near  $x = -22$  cm) of inductive power evolution over half of an RF cycle. The two rows correspond to two time stamps (25 and 45  $\mu s$ ) in the early discharge. The columns from left to right are times,  $t/T_{RF} = 0, 0.125, 0.25, 0.375,$  and  $0.5,$  respectively. The first column correspond to maximum antenna current. Note that there is a small negative power (most pronounced in the second column). (b) Total inductive power integrated through the volume shown together with input power. The red dots correspond to the two times shown in panel (a).

$P_{ind}/P_{tot} \simeq 0.1.$  We infer that the rest of the power is coupled capacitively. The plasma is identified as in E-mode at this time. Between  $0-50 \mu s,$  current on the antenna rises,  $P_{ind}/P_{tot}$  rises from  $0.1$  to  $0.8$  at  $50 \mu s.$  A simultaneous decrease in capacitive power marks the E-H transition<sup>2</sup>. From  $50 \mu s$  on, the plasma stays in H-mode with  $P_{ind}/P_{tot} \simeq 0.8.$

At 5 mTorr, the lower e-n collision frequency resulted in a higher conductivity, with a correspondingly shorter magnetic skin depth. This results in the induced field being concentrated closer to the antenna compared with 25 mTorr. The sharp gradients of the field contribute more noise to the derivative terms in the calculation  $\mu_0 \mathbf{J} = \nabla \times \mathbf{B}.$  At 5 mTorr, the power deposition profile at  $50 \mu s$  looks very similar to that at  $25 \mu s$  for the 25 mTorr case, with  $P_{ind}/P_{tot} \simeq 0.1.$  At the lower pressure the change in power deposition

<sup>2</sup>Personal communication with M. Kushner, 2019

profile also happens over a longer period of time. At  $100 \mu s$ , plasma is in H-mode with  $P_{ind}/P_{tot} \simeq 0.85$ .

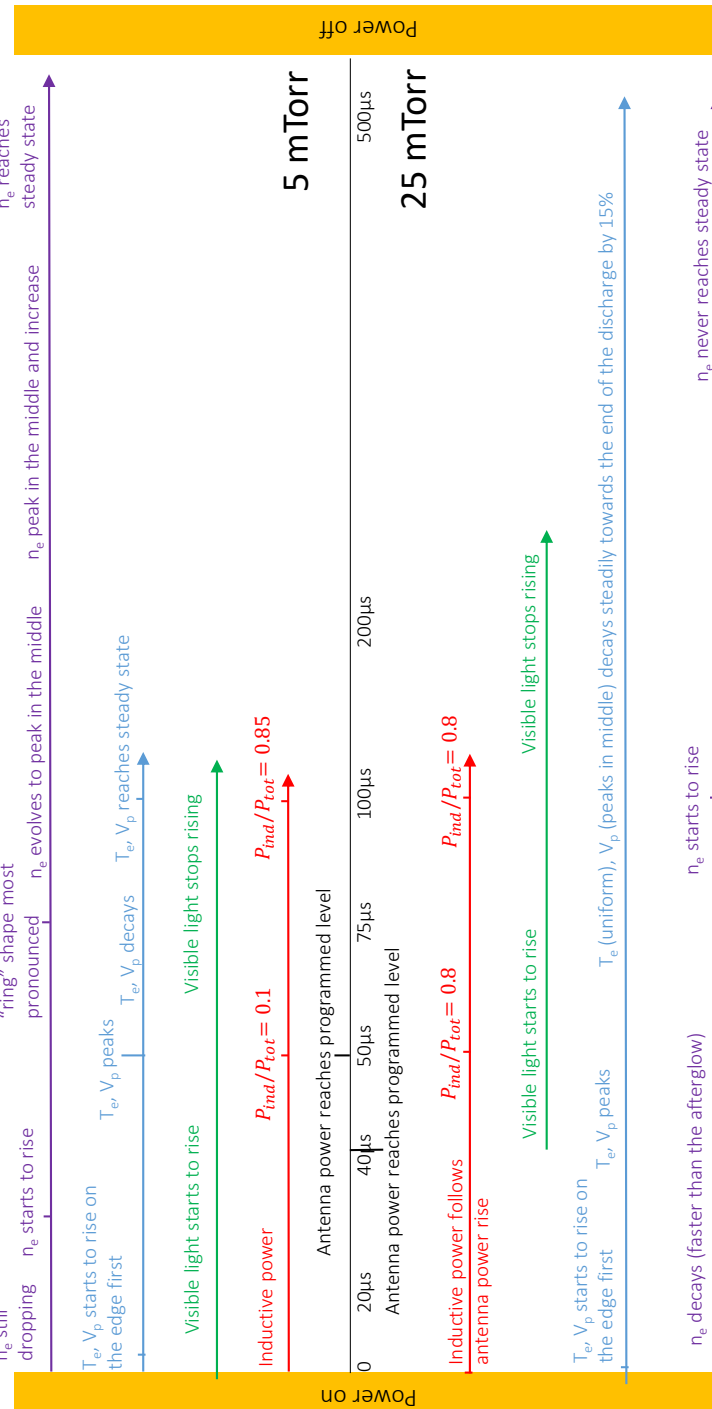


Figure 3.18: A summary of different plasma parameter's evolution during pulsed discharge in Ar 1kHz 50% duty cycle with peak input power of 300 W.

Previous authors describe a variety of signatures of the E-H transition. E-mode is frequently recognized as a “relatively dim (glow) mode” and an H-mode as an “intense bright mode”[40]. While ramping up RF power, an abrupt light intensity change is observed[83], as well as a jump in plasma density[84]. Amorim *et al.*[42] reported an increase in density from  $10^{10}$  to  $10^{12} \text{ cm}^{-3}$  at 64 mTorr argon. Kortshagen *et al.*[44] recognized a two orders of magnitude increase in light emission. Another noticeable feature in E-H transition is said to be a drop in antenna current[85]. Since there was very little direct volumetric measurement of plasma inductive or capacitive power deposition prior to this work, definitions based on  $P_{ind}/P_{tot}$  and  $P_{cap}/P_{tot}$  do not exist in the literature.

A timeline of the evolution of various plasma parameters is presented in Fig. 3.18 for the pulsed operation described in section 3.2. None of the plasma parameters’ evolution can be described as a “sudden change”. If we put the probe (Langmuir or hairpin) at where the “ring” shape profile is most pronounced, we will observe a “density jump” as described by Yamashita[84] and others. However, if we place the probe in the middle of the chamber, we will see a different time dependence. Even if density is measured on a chord across the chamber, it is still easy to draw different conclusions depending on which chord one chooses to measure. Note that the evolution of the density is uncorrelated with the evolution in power deposition.

At 5 mTorr, the plasma potential  $V_p$  experiences an overshoot in the DC component. The drop in  $V_p$  after  $50 \mu\text{s}$  and sudden increase in visible light has also been described as a signature of the E-H transition, by Seo *et al.*[79] and Lee[80]. At 25 mTorr, this is not observed.  $V_p$  starts to rise at  $20 \mu\text{s}$  but the light starts to rise at  $40 \mu\text{s}$ . Using the visible light signal as a proxy, the plasma seems to be in E-mode prior to  $40 \mu\text{s}$ . The rise and fall in  $V_p$  is smooth without an overshoot during the transition. Based on observation,  $V_p$  rises at 25 mTorr, but falls at 5 mTorr during the E-H transition.

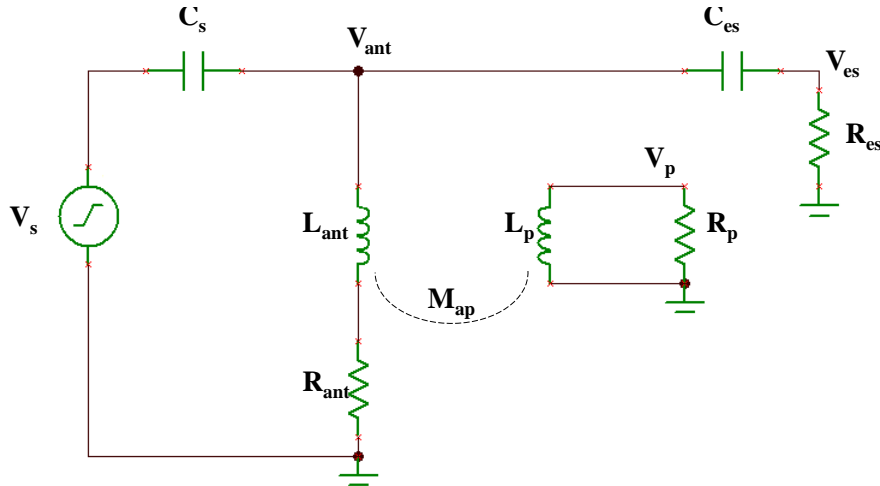


Figure 3.19: A simple circuit representation of the ICP system. Capacitive coupling is represented as  $C_{es}$  and  $R_{es}$ ; inductive coupling is represented as  $L_p$ ,  $R_p$ , and  $M_{ap}$  (mutual inductance between  $L_{ant}$  and  $L_p$ ).

### 3.4 Lumped element model

At any given instant, power is coupled both capacitively and inductively from the RF coil to the plasma. We are able to accurately measure total power from the RF generator, and to approximate the power dissipated inductively in the plasma as discussed above. To shed light on the balance between inductive and capacitive power coupling, we model the electrical operation of the entire ICP system as the circuit shown in Fig. 3.19. Ultimately we find that the system behaves as a driven damped harmonic oscillator with time varying damping. Features that others have identified as characterizing the E-H transition are probably unrelated, or at best only related tangentially.

In E-mode, the high voltage on the antenna creates an RF sheath near the ceramic top. The RF displacement currents flowing through this sheath and the bulk plasma to ground leads to heating and ionization. The equivalent circuit element is a capacitor  $C_{es}$  connected from the antenna high-voltage lead to a resistor  $R_{es}$  where the power is dissipated. In H-mode, plasma is mostly sustained by induction current. The plasma current channel has inductance  $L_p$ , with current driven by the mutual inductance to the

antenna winding, and power dissipated in the equivalent resistor  $R_p$ .

For a given input voltage  $V_{ant}$ ,  $V_p$  and  $V_{es}$  can be calculated by solving a system of differential equations associated with the circuit. This requires an understanding of the plasma circuit elements— $R_p$ ,  $L_p$ ,  $C_{es}$ , and  $R_{es}$ . These values depends on electron density, temperature, neutral pressure, dimensions of the chamber, location of the coils etc. Based on experimentally measured data, we estimated these values as follows:

$C_{es}$  is estimated using  $\epsilon A/d$  where  $A$  is the surface area of the antenna,  $d$  is the thickness of the ceramic top (made of alumina), and  $\epsilon/\epsilon_0 = 10$  is the permittivity of alumina (thin sheath assumption).  $L_p$  is estimated by approximating the plasma as a torus carrying uniform current. The self-inductance of a torus with major radius  $a$  and minor radius  $r$  is given approximately by [86]

$$L \simeq \mu_0 a \left[ \left( 1 + \frac{r^2}{8a^2} \right) \ln\left(\frac{8a}{r}\right) + \frac{r^2}{24a^2} - 2 + \frac{1}{4} \right] \quad (3.3)$$

We define  $r$  as the full width half max (FWHM) of  $J_\phi$  at the instance of maximum antenna current, and  $a$  is the radial distance from the chamber centerline to the maximum of  $J_\phi$ . The evolution of the current profile during a plasma pulse (Fig. 2.7) reveals that  $r^2$  varies by at most a factor of 2, and  $a$  varies by less than 0.3. This is not enough variation to change  $L_p$  by a significant amount, because of the logarithmic dependence on  $a/r$  and  $r^2/a^2$  in Equation 3.3. The coupling between the antenna and the plasma is also affected by a mutual inductance  $M_{ap} = m_c \sqrt{L_{ant} L_p}$  where  $m_c$  is the coupling efficiency between the two inductors.  $m_c$  is then estimated by matching the time dependence of  $I_{ant}$  to the measurement (Pearson current monitor) with the same input voltage from the supply.

Assuming the plasma obeys Ohm's law, we pick  $R_p = 2P_{ind}/I_0^2$ , where  $I_0$  is  $J_\phi$  integrated within the FWHM. Another method to estimate  $R_p$  is by calculating the resistivity  $\rho = 1/\sigma_p$  using Equation 3.2 for the plasma conductivity. The collision frequency is extracted from Fig. 3.5 with  $T_e$  from Langmuir probe data and  $n_e$  from hairpin probe data. The resistance  $R_{p,\sigma} = \rho l/A$  is estimated with  $l = 2\pi a$  and  $A = \pi r^2$ , where  $a$  and  $r$  are the same quantities used in the inductance calculation. The second approach gives a resistance of 5 times smaller than the first, which is also too small for reasonable ap-

proximation for the circuit model. The errors in estimating the resistivity are subject to uncertainties in  $T_e$  and  $n_e$  (10 – 20% for each). The length and area approximated for  $R_p$  can also be off by 10 – 20% or more. Moreover, in cases where stochastic or non-local heating is non-negligible[87, 88, 89, 90], Ohm’s law could fail.

The E-mode resistance is difficult to estimate *a priori*, because it is not clear which path the displacement current travels through the plasma in this geometry. In general,  $R_{es}$  should be much bigger than  $R_p$ , because the displacement current is concentrated near the top and does not reach the bulk. For results shown below,  $R_{es}/R_p$  is chosen to give a 10% capacitive power in steady state H-mode.

The circuit response in Fig. 3.19 can be solved with the following system of differential equations:

$$V_{ant} - L_{ant}\dot{I}_{ant} - M_{ap}\dot{I}_p - I_{ant}R_{ant} = 0 \quad (3.4)$$

$$V_p - M_{ap}\dot{I}_{ant} - L_p\dot{I}_p = 0 \quad (3.5)$$

$$I_{ant} + (C_s + C_{es})\dot{V}_{ant} - C_{es}\dot{V}_{es} - C_s\dot{V}_s = 0 \quad (3.6)$$

$$C_{es}(\dot{V}_{es} - \dot{V}_{ant}) + V_{es}/R_{es} = 0 \quad (3.7)$$

$$I_p - V_p/R_p = 0 \quad (3.8)$$

$$C_s(\dot{V}_s - \dot{V}_{ant}) + I_s = 0 \quad (3.9)$$

In the above equations,  $L_p$ ,  $M_{ap}$ ,  $R_p$ , and  $R_{es}$  are all functions of time. Their time dependence is taken to be much slower than that of the voltages and currents, with second-order terms neglected to solve the equations in a WKB sense. In pulsed operation, a voltage waveform oscillating at 2 MHz is applied to  $V_s$ . The differential equation is solved numerically using the first order forward finite difference method.  $V_s$  is incremented with a time step of 0.125 ns (each RF cycle contains 4000 points). As a start, we apply the source voltage measured in the experiment for  $V_s$  using fixed values of  $R_p$ ,  $L_p$ ,  $M_{ap}$ ,  $C_{es}$ , and  $R_{es}$  to the differential equations. This aligns with operation of the pulsed Argon plasma described in section 3.2.

Fig. 3.20 shows the antenna current and source power comparing solution from the

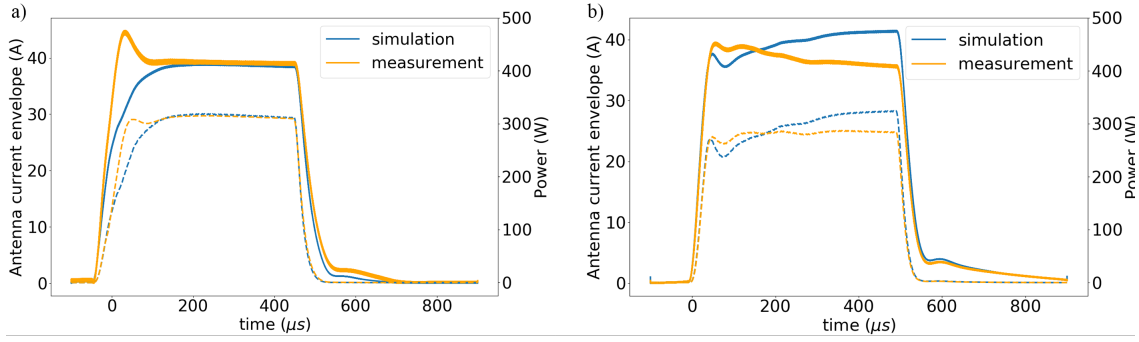


Figure 3.20: Comparison between lumped element model (blue) and experimentally measured (orange) antenna current (solid) and power (dashed) with constant circuit elements. The fill pressure are 5 and 25 mTorr for panel (a) and (b) respectively.

differential equations with constant circuit elements to measurement. At 5 mTorr (panel a),  $I_{ant}$  and  $P_{tot}$  deviates at the beginning of the discharge. This is because a much smaller  $n_e$  at this time corresponds to a larger  $R_p$  than during the rest of the active-glow.  $I_{ant}$  or  $P_{tot}$  at 25 mTorr (panel b) deviates from experiment after 200  $\mu s$ , primarily because  $R_p = 8 \Omega$  is too big compared to the plasma resistance. With the increase in  $n_e$  throughout the active-glow (Fig. 3.10), we expect  $R_p$  to decrease, since the plasma conductivity is proportional to  $n_e$ .

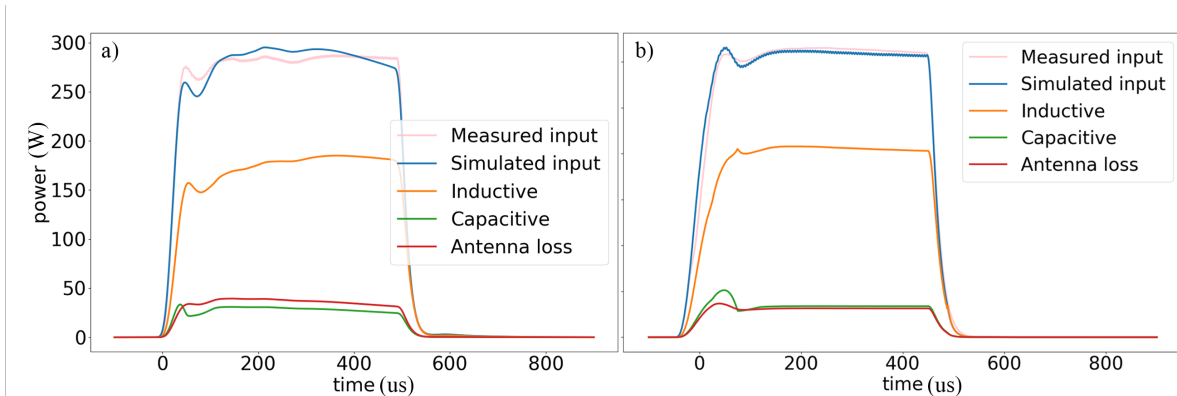


Figure 3.21: Comparison between lumped element model (blue) and experimentally measured (pink) power. The fill pressure are (a) 25 and (b) 5 mTorr. The inductive, capacitive, and antenna loss power are calculated using  $V_p^2/R_p$ ,  $V_{es}^2/R_{es}$ , and  $I_{ant}^2 R_{ant}$ , respectively.

With fixed circuit elements estimated based on steady state probe measurements as described above, Fig. 3.20 shows a fairly accurate match in antenna current and power between the lumped element model and experiment. We can take a further step by adjusting the circuit elements based on experimentally measured  $J_\phi$ . Fig. 3.21 shows different power deposition as a function of time. The total simulated power input follows the measured antenna power closely. Because we are applying the measured experimental RF source voltage, this accuracy in tracking the power also indicates  $I_{ant}$  matches the experiment.  $P_{ind}$  increase slower at 5 mTorr compare to 25 mTorr, consistent with Bdot probe measurement. Surprisingly for both cases,  $P_{cap}$  never exceeds  $P_{ind}$ . This is not an obvious result based solely on experimental results described above, since we are unable to directly measure capacitive power. From experimental data (Fig. 3.17), we observed a linear increase in  $P_{ind}/P_{tot}$  at the beginning that matches the model result. The sudden “jump” in parameter space (i.e.  $V_p, T_e, n_e$ ) at the E to H mode transition were observed for the 5 mTorr case. However, based on the simple circuit model we infer that the inductive power is always bigger than the capacitive power.

To understand the “overshoot” behavior during initiation, we analyze the circuit model by keeping  $C_{es}, L_p$  constant and varying  $R_p$  and  $R_{es}$  only. This choice is made because changes in  $L$  and  $C$  are less significant since they are mostly related to the geometry of the system, which does not change very much. In contrast, the change in  $R$  is significant (few orders of magnitude) as it’s closely related to the plasma density and temperature. While varying  $R_p$  and  $R_{es}$  in the circuit simulation, we note that changing the ratio  $R_{es}/R_p$  changes  $dP_{cap}/dt$ , but affects  $dP_{ind}/dt$  by less than 1%. For simplicity, the following analysis uses a fixed value of  $R_{es}/R_p$  for all scenarios.

A 2 MHz input voltage with a ramp-up time of  $40 \mu s$  is applied to the input of the circuit. This corresponds to the fastest ramp time available from the RF generator used in the experiment. When current on the antenna is first increasing, plasma density doesn’t start to increase immediately because enough electrons need to be accelerated to ionization energy. We represent this by holding  $R_p$  constant for the first  $20 \mu s$ . As  $n_e$  increases,

we program  $R_p$  to decrease. We chose a linear decrease in  $R_p$  during the period from 20 to 75  $\mu s$ . For simplicity, we assumed  $R_p$  stopped changing after 75  $\mu s$ .  $R_{es}/R_p = 100$  throughout the pulse.

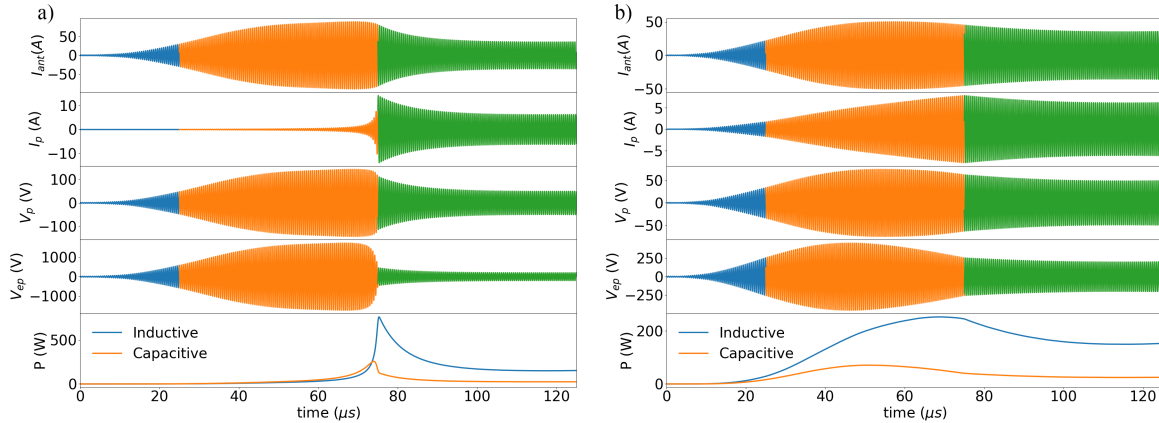


Figure 3.22: Simulation result of voltage and current in the circuit. The panels from top to bottom are antenna current, inductive plasma current, inductive plasma voltage, capacitive plasma voltage, and power. They are measured in the circuit at locations shown in Fig. 3.19. In the period of time designated in blue,  $R_p$  is held constant at 20  $\Omega$  in (a) and 1000  $\Omega$  in (b). During the portion of the discharge designated in orange,  $R_p$  linearly decreases from its initial value to 8  $\Omega$  in both panels. In the green section,  $R_p = 8 \Omega$  in both panels.

Fig. 3.22 shows the effect of changing  $R_p$  in two scenarios. Panel (a) represents the case of breakdown from vacuum. The behavior can be understood as a series RLC circuit connected driven by an AC voltage source. In an RLC circuit, the resistance acts as a “damping” term to the oscillation. Between 0 to 50  $\mu s$ ,  $R_p$  is sufficiently large that it acts like an open circuit, and there is very little damping. During this time, energy builds up in the LC tank circuit without appreciable damping – i.e. the antenna current rises. When  $R_p$  decreases past a certain threshold, damping increases (if  $R_p \rightarrow 0$ , damping also disappears, but the plasma conductivity never gets this high). If  $R_p$  decreases rapidly, the power into the plasma overshoots its steady state value due to residual stored en-

ergy in the reactive elements of the match network and antenna (here represented by the tank circuit  $C_s$  and  $L_{ant}$  in Fig. 3.19). With a linearly decreasing  $R_p$ ,  $I_p$  increases with approximately a  $1/R_p$  dependence. When  $R_p$  stops changing ( $t=75 \mu s$ ), the system gradually reaches steady state with RF input power from the voltage source dissipated in the resistor.

This sheds light on the behavior observed in the experiment. There has to be enough plasma inside the chamber to sustain an inductive current. Capacitive coupling is necessary to reach this critical density. For situations where the plasma density is too low such that  $R_p$  reassembles an overdamped response, a bigger “overshoot” or “jump” is observed in the antenna or inductive current. The inductive current and plasma resistance affects each other— $I_p$  increase with decrease in  $R_p$ ; increase in  $I_p$  creates more plasma, pushing  $R_p$  to decrease even more. The system eventually reaches an equilibrium where the damping factor no longer changes.

Figure 3.22 (b) addresses re-ionization of a repetitively pulsed plasma. Similar to panel (a),  $I_p$  in panel (b) also follows  $1/R_p$ . In reality, different settings (gas species, pressure, RF voltage program...etc) provides different time rate of change in  $n_e$  and  $T_e$ , which in turn changes  $R_p$  on different time scales. If  $I_p$  happens to be passing the fast growing or decaying region on the  $1/R_p$  curve in a very short time, an “abrupt” change will be observed. Note that this is unrelated to transitioning from capacitive-power-dominated to inductive-power-dominated. As mentioned above, changing  $R_{es}/R_p$  changes  $dP_{cap}/dt$ , but doesn’t change  $dP_{ind}/dt$ . The intersection of  $P_{cap}$  and  $P_{ind}$  in (a) can be shifted ( $\pm 5 \mu s$ ) by changing  $R_{es}/R_p$ , while  $I_p \propto 1/R_p$  remains the same. On the other hand,  $P_{cap}$  and  $P_{ind}$  never intersects in panel (b).

Among the five graphed quantities, the antenna current is the only solid measurable quantity.  $I_p$  and  $P_{ind}$  can be estimated from Bdot probe data. The others are not measurable. The drop in antenna current, although previously identified by researchers as a signature of E-H transition, shows up on both (a) and (b). The drop is related to the change in damping in the RLC circuit picture.

## CHAPTER 4

### Conclusion

This thesis describes time-resolved fully three-dimensional measurement of fundamental plasma parameters in an industrial etch tool. Results are reported in steady state and pulsed operation with argon. A simple 0D model was presented and shown to capture the essential behavior of the system. The experimental result and model serves as a baseline and points direction to investigations in the future. The research will hopefully provide insight into the current operation of and the future design of plasma processing machines.

Three-axis Bdot probes were used to measure the magnetic field. Plasma current derived from  $\vec{B}$  dominates in the azimuthal direction and is typically about  $180^\circ$  out of phase with the antenna current. The dynamics resemble eddy current penetration into a conductor from an external driving source. For each RF half-cycle, the current channel initially forms slightly inward and downward from the antenna. As the antenna current reverses, a new current with reverse sign forms under the coil and gains strength while the previous current maximum decays and moves downwards. The 3D current profile shows cylindrical symmetry (current flowing in the azimuthal direction) is a good assumption and can be used in analysis for ICPs of this geometry. Based on this work, we conclude that a 2D RZ-plane of magnetic field data with accurate measurement of two components ( $B_r$  and  $B_z$ ) is the minimum requirement to study the behavior of the inductive current.

With the observed cylindrical symmetry, the electromagnetic electric field is derived from Bdot data using Faraday's law. This electric field and the computed current are used to calculate the inductive power, which deposits almost directly under the coil. This is where the image current from the coil is largest. It is also where the inductively generated

electric field is large, since the image current shields the field from the bulk of the plasma. The power is deposited closer and closer to the antenna with increasing neutral pressure. This is due to increasing electron density at higher pressure (for a given power), which results in increasing conductivity and consequently shorter skin depth. With computed volumetric power density, we integrate over the measured volume to estimate the total inductive power dissipated in the plasma. The inductive power comprises more than 80% of the total power from the generator in steady state.

Measurements of the EEDF,  $n_e$ ,  $T_e$ ,  $V_p$ ,  $J_\phi$  and  $P$  are presented for two industry-relevant neutral pressures (5 mTorr, 25 mTorr) with plasma pulsing at 1 kHz repetition rate, 50% duty cycle and a peak power of 300 W. For each shot, the plasma density decays during the unpowered after-glow phase, but remains in the chamber with a peaked profile. As RF powered-on, the field from the antenna accelerates electrons and heats the residual plasma from the previous shot. This heating results in increased ambipolar diffusion, and we observed an associated density pump-out before new ionization begins to dominate.

When the antenna current begins to rise, the plasma initiates in a “ring” shaped density profile near the top of the chamber with a peak a few centimeters under the ceramic lid. Radially it peaks slightly inward from the antenna. As plasma reaches steady state, the density profile transforms to being peaked in the middle of the chamber at 5 mTorr. In contrast, the density profile in pulsed 25 mTorr plasma always peaks in the middle of the chamber. With a large enough leftover density from the previous shot, ionization is always proportional to  $n_e$ .

Interestingly, the maximum plasma density does not co-locate with the region of peak power deposition. Given a uniform temperature profile (confirmed by Langmuir probe measurement), the peaked density profile solves a simple diffusion equation model with ionization uniformly distributed throughout the reactor. Plasma potential measured by the emissive probe follows the spatial profile of density. The space charge field derived from  $V_p$  points away from the center where density is a maximum, reproducing the Maxwell-Boltzman relation.

Density profiles do not always peak in the center of the chamber. At sufficiently high pressure, the density peaks as a “ring” shape near the antenna due to the e-n collision mean free path becoming much shorter than the chamber dimension. This also holds for pulsed operation when the active glow period is long enough for the plasma to approach a quasi-steady state equilibrium value. At high pressure, measured inductive field and power concentrates closer to the ceramic top as well.

Based on the timeline of various plasma parameter evolution, the two cases (5 and 25 mTorr) revealed distinct behaviors at the beginning of the active-glow. Previous researchers have identified the E-H transition with an abrupt increase in light, and abrupt drop in  $V_p$ . This is observed at 5 mTorr but not at 25 mTorr. Measurement results allude that a plasma may never experience E-H transition at 25 mTorr. Furthermore, the evolution of plasma density is uncorrelated with the evolution in power deposition. Neither of the signatures of E to H transition, which are rapid change in the light or plasma potential, or variations in the EEDF, are clearly connected to the evolution in inductive power deposition.

A lumped element circuit model was derived to help explain the experimental observation in pulsed plasma, especially the E-H transition. The system of differential equations is solved numerically with circuit elements estimated from experimental data. Based on model and experiment, we derived that the ICP runs as a superposition of a capacitively coupled current (with dissipation modeled by a simple resistor  $R_{es}$ ) and an inductively coupled current (dissipated in  $R_p$ ). The match network and antenna are modeled by a simple capacitor in series with the antenna inductor to form an LC tank circuit. When plasma density is very low, energy builds up in the tank circuit with negligible damping. Power is either coupled to the plasma capacitively, depending on the sheath resistance and capacitance, or dissipated in the electronics. As electron density builds up in the plasma via E-mode, the plasma resistance  $R_p$  decreases, increasing dissipation via this channel. Eventually the damping via  $R_p$  begins to dominate, and the plasma is sustained inductively. The capacitive power coupling does not affect and is not affected by

the inductive power coupling. From this picture, the observed characteristics of the E-H transition is a result of the rapid decrease in  $R_p$ , as opposed to previously hypothesized changes in the ratio of capacitive to inductive power. A key result is that operating the ICP in pulsed mode under the proper conditions is capable of keeping the plasma always dominated by inductively coupled power while the power on the antenna turns on and off.

The pursuit of a stable and controllable plasma source producing high etch efficiency motivates research in ICPs. By studying the plasma behavior during pulsed and steady state operation, we identified the plasma resistance  $R_p$  being the most deterministic factor in control. Unfortunately, due to the complexity of plasmas, it is difficult to derive  $R_p$  from first principles. For investigations in this thesis using argon, an estimate based on plasma conductivity did not provide a reasonable answer. Deriving a value for  $R_p$  will be even harder for electronegative gases. However, from an application point of view, it is not necessary to derive  $R_p$ . For example, we are able to program the voltage waveform to eliminate some “overshoot” type behavior in antenna current, which reflects directly in plasma current. Using the lumped element model, one can test and adjust the voltage waveform to achieve the desired outcome. Another possibility to control the plasma is by adding an external resistor in series with  $R_p$ . This will ensure a damping term to always exist, and prevent energy build up in the LC tank circuit.

Future work involves extending the experimental investigation to electronegative gases, as well as testing the validity of the lumped element model in these plasmas. It is also important to measure plasma properties with the RF bias applied to the wafer. For example, one interesting aspect is measuring the ion velocity using Laser Induced Fluorescence with interleaved plasma and bias pulsing.

## APPENDIX A

### RF compensation circuit for Langmuir probe

Consider a probe immersed in plasma. The resistance between probe tip and ground (chamber wall) can be approximated by  $R_{pl-pr} \approx \frac{dV}{dI_{pr}}|_{V_{float}}$ . The probe circuit has an impedance  $Z_{pr} = R_{pr} + jX_{pr}$ , i.e. a resistive part  $R_{pr}$  and reactive part  $X_{pr}$ . The goal of rf compensation in a Langmuir probe circuit is to allow the tip to track RF fluctuations in the local plasma potential, while still providing a net DC offset to the probe tip relative to that fluctuating potential.

Several probe circuits are illustrated in Fig. A.1. Panel (a) shows a probe without compensation. This can have two possible problems in a plasma with rf. The first, which occurs if the frequency is high, is an rf sheath being created around the probe. This sheath can cause the probe tip voltage to be offset by an amount that may change with applied bias. The second problem is distortion due to averaging over the rf fluctuated potential, as described in section 2.2.2 and illustrated in Fig. 2.2. This is more relevant for the 2 MHz case we consider.

The solution to both problems is to let the probe tip float with the local AC voltage fluctuation, while biasing it at a DC offset relative to the plasma potential in order to sweep out the probe characteristic. This can be accomplished by using a large enough impedance between the DC probe biasing circuit and the plasma. In particular  $|Z_{pr}| \gg |R_{pl-pr}|$ . This large impedance can be achieved using resistors (Fig. A.1 b) or inductors (Fig. A.1 c). The large impedance must be placed close to the probe tip, as even 1 m of coaxial cable has a capacitance to ground of about 100 pF, which is about 800  $\Omega$  at 2 MHz. A large enough probe circuit impedance is hard to achieve at all times during pulsed

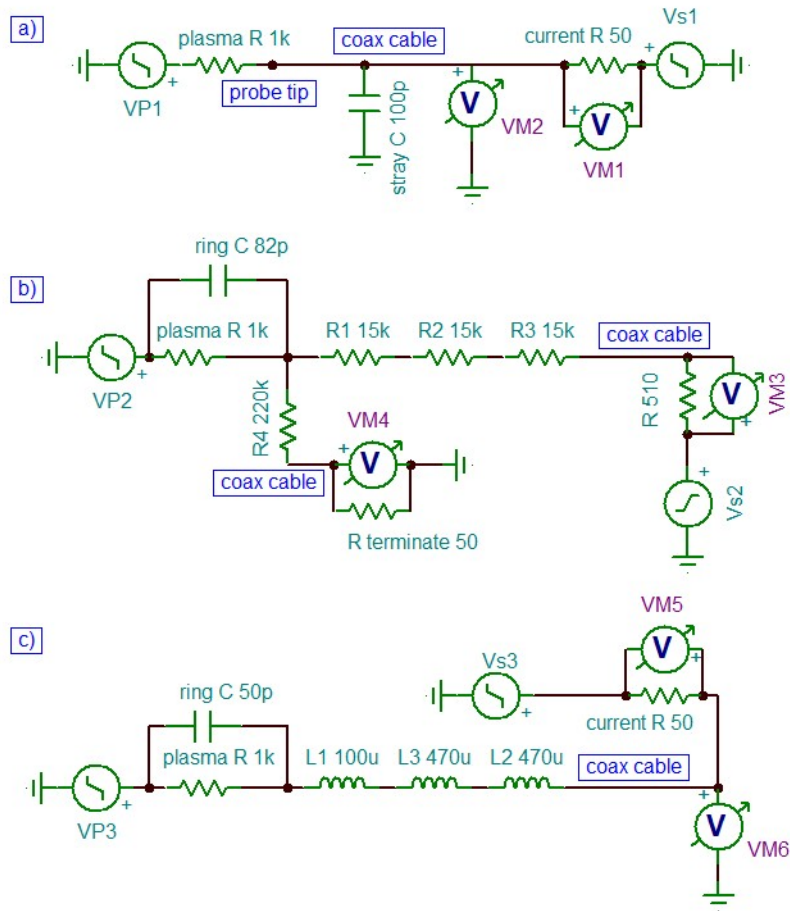


Figure A.1: Langmuir probe circuit simulated in SPICE (a) without rf compensation (b) compensated with resistors (three resistors to reduce parasitic capacitance) (c) compensated with inductors. Signal generators labeled VP simulate rf oscillation of the plasma potential. This is connected to the probe tip through "plasma R". The function generators labeled VS represent voltage ramp generators to sweep the probe. Voltage monitors VM1/3/5 measure the current in the circuit and VM2/4/6 measure voltage on the probe. Note that VM4 in panel (b) does not measure the voltage on the probe tip directly. The coax inside the probe shaft is terminated in  $50\ \Omega$  so is frequency independent. In panel (b) and (c), an extra ring is placed inside the plasma to enhance the AC connection between probe tip and plasma.

plasma operation (also at all spatial locations), since at low density the probe has a much higher  $R_{pl-pr}$ . To reduce the AC impedance to the local plasma, an auxiliary electrode is connected to the probe tip through a small capacitor. At the rf frequency the impedance of this connection shunts  $R_{pl-pr}$ , helping the tip to track the local plasma potential more accurately.

A limitation of the resistor circuit in Fig. A.1 (b) is that it is relatively difficult to change the voltage on the probe tip to sweep out a probe characteristic. The probe tip is biased to a voltage  $V_b = V_s - I_{pr}R_{pr}$ , where  $V_s$  is the output voltage from the supply. Since  $R_{pr} \gg R_{pl-pr}$ , most voltage will drop across the circuit elements with little bias appearing on the probe tip. This was overcome by using a high voltage sweeper. Note that the current measuring resistor is also part of  $R_{pr}$ , which is chosen according to the size of the current. For the circuit elements shown in Fig. A.1 (b), the probe current  $I_e = \frac{VM3}{510} - \frac{VM4}{50}$ . The biggest problem with this circuit is that the probe tip—the resistors in the circuit will melt before the probe tip glows red hot.

The circuit shown in Fig. A.1 (c) does not have a large DC impedance. This probe is shown in detail in Fig. A.2. The circuit is identical to panel (a) with DC voltage, and suppress AC fluctuations. However, it is hard to get high enough  $Z_{pr}$  with available components. At 2 MHz, the measured impedance of the probe circuit with elements shown in panel (c) is approximately 12 k $\Omega$ . If the rf source operates at a fixed frequency, with the right combination of inductors and capacitors, the choke filter can be designed to resonate at the fundamental (and second and third if necessary) frequency such that  $|Z_{pr}| \gg |R_{pl-pr}|$ [91]. Unfortunately, the "frequency agile" design of our rf source prevents it from operating at a fixed frequency.

The choke filter plus the AC coupling ring has to compensate for 2 MHz rf, but at the same time maintain a response time faster than 50 kHz, such that the time evolution during pulsed plasma operation is not distorted. This is achieved by picking suitable values of capacitor and inductors in the probe circuit. Even so, the stray capacitance of the circuit distorts the voltage with a ramp period shorter than 25  $\mu$ s. Therefore, we

implemented a stepped sweep method where the probe voltage is scanned between -5 V to +20 V with a resolution of 200 steps. Because of the distortion in  $I_{esat}$  from biasing the probe for too long (see section 2.2.2), the step duration was held at 50  $\mu s$ . This allowed 25  $\mu s$  for the voltage to settle on the various components, and 25  $\mu s$  for the measurement.

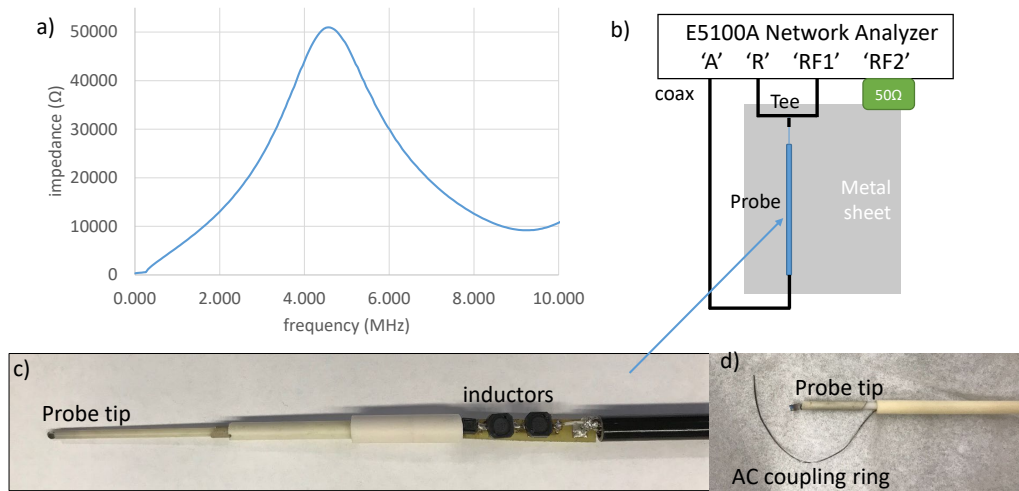


Figure A.2: (a) Measured impedance of the compensated probe as a function of frequency. (b) Bench setup using E5100A Network Analyzer for testing the probes. (c) Photo of the probe with compensation circuit. Note that the circuit board cannot be placed inside the probe shaft. d) Probe with AC coupling ring.

A bench test of the compensation scheme shown in Fig. A.1 (c) was conducted using a Network Analyzer. The Network Analyzer output “RF1” sends a signal to the probe tip through a BNC tee, the amplitude of which is monitored at input “R”. A response is measured at the end of the probe (A). The network analyzer generates the ratio  $A/R$ , which is used to infer the impedance of the compensation network as a function of frequency as shown on Fig. A.2 (a). At 2 MHz (the operating frequency of the ICP), the impedance from the probe tip is about 12 kΩ—large compared to the approximately 1 kΩ plasma connection resistance near the center of the plasma. The impedance is even higher at the 2d, 3d, and 4th harmonics. The connection resistance increases to 10 kΩ at the edge, but significantly

less rf in those regions (except under the antenna) ensure measurement results to be accurate. Fig. A.2 (b) is a schematic of the test setup. The metal sheet forms a well-defined ground plane, which is also connected to the outer conductor of the coax—representing the chamber wall as ground. Fig. A.2 (c) shows a photo of the probe before covering up the circuit board with epoxy resin. The circuit board with surface mount inductors cannot be placed inside the stainless probe shaft because that reduced the AC impedance below that in Fig. A.2 (a). The epoxy resin does not affect the frequency response. Fig. A.2 d) shows the probe with the extra AC coupling ring.

## APPENDIX B

### Hairpin probe analysis

Multiple hairpin probes were constructed during the course of the experiment. Fig. B.1 shows an example of one of such probe tested in vacuum. Panel (a) is the frequency response recorded from a Network Analyzer (Agilent N5230(c)). The blue trace (S11) is reflected signal—using the same loop to detect the resonance. The grey trace (S12) is transmitted signal—using a second loop to detect the resonance. The reflection technique is very noisy potentially due to standing wave modes in the coax. We used the transmission mode which reveals a resonance at 9.87 GHz with a quality factor  $Q = 17$ .

For cheaper and easier use of hairpin probe, the Network Analyzer was replaced by home made circuit consisting mixer, directional coupler, amplifier, and voltage controlled oscillator (VCO) developed by Wug *et al.*[72]. A 0-10 V ramp serves as the control voltage, providing an output frequency scan of 2-4, 6-10, or 8-12 GHz depending on the specific circuit board. The hairpin resonant frequency can be accurately determined with the ramp sweep time as short as 5-10  $\mu s$ , giving very good time resolution of the density. A combination of attenuators and amplifiers are used as a variable gain stage for the hairpin probe to optimize the signal to noise ratio. The mixer output signals are oscillating waveforms with phase information encoded in it. These traces measured in vacuum are shown in Fig. B.1 (b). The following steps are used to find the resonant frequency:

1. Add the square of the two output signals (from b). The result is shown as the blue solid line on (c).
2. Fit an offset-Gaussian function to this envelope and select the center of the Gaussian as the resonant frequency (orange line on panel c).

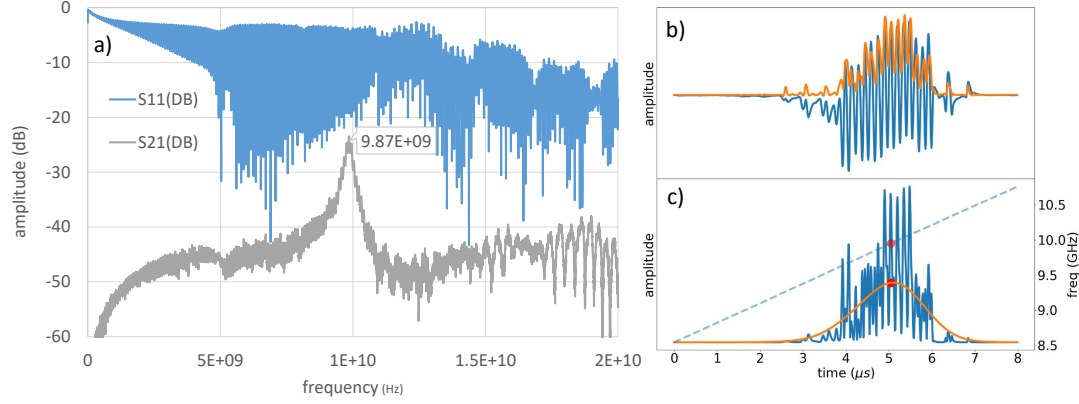


Figure B.1: Vacuum (no plasma) frequency response of the hairpin probe. (a) Transmitted (S21) and reflected (S11) signal recorded on a Network Analyzer. (b) Mixer output signal from the hairpin probe circuit collected by a digital scope. (c) Blue solid line: amplitude of the mixer output signals. Orange solid line: Gaussian fit of the envelope. Blue dashed line: frequency sweep from the VCO.

3. Determine the frequency from the measured ramp voltage (blue dashed line). Note that the sweep data are recorded in volts and needs to convert to frequency. We determined the voltage-to-frequency function by static testing on the bench; this frequently deviated a few percent from VCO spec sheet.

The measured vacuum frequency from the home made circuit is in close agreement with the resonance measured from the Network Analyzer. The sweep time of the hairpin probe resonance is 200 kHz, allowing  $5 \mu s$  time resolution. When immersed in plasma, this resonance peak will shift to higher frequencies depending on local electron density  $n_e$ .

Due to its construction, the hairpin probe is partially covered with epoxy. This makes equation 2.11 inaccurate for deriving  $f_p$ . A transmission line model used to describe this situation is implemented to derive the plasma frequency[70]. The relationship between  $f_r$  and  $f_p$  becomes

$$\sqrt{\frac{f_r^2}{f_r^2 - f_p^2}} - \sqrt{\frac{1}{\epsilon_e}} \tan\left[\frac{2\pi l_2 \sqrt{f_r^2 - f_p^2}}{c}\right] \times \tan\left[\frac{2\pi f_r l_1 \sqrt{\epsilon_e}}{c}\right] = 0 \quad (\text{B.1})$$

where  $\epsilon_e = 3.17$  is the relative permittivity of the epoxy,  $l_1$  is the length of hairpin covered in epoxy,  $l_2$  is the length of hairpin exposed in plasma, and  $c$  is the speed of light. Here the permittivity of epoxy was previously determined by comparing a hairpin's resonant frequency fully covered with epoxy  $f_0^*$  to its resonant frequency in vacuum ( $\epsilon_e = (f_0/f_0^*)^2$ ).

The length of the hairpin  $l_1$  and  $l_2$  are "effective" lengths rather than actual length of the wire. For example, when the hairpin probe is positioned differently between the measuring loops at the end of the coax, the resonance frequency shifts slightly even while physical dimensions  $l_1$  and  $l_2$  are unchanged. We therefore add a correction factor to the ratio of  $l_1/l_2$  and calibrate the hairpin probe by matching the line averaged density measured by the probe to interferometer measurements. The resulting line averaged time behavior of  $n_e$  turns out to be in excellent agreement with the interferometer (see Fig. [3.11](#)).

## APPENDIX C

### Bdot probe construction

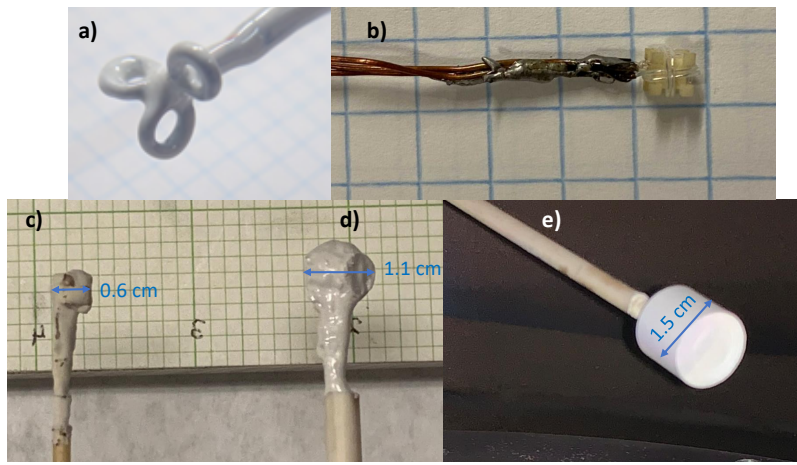


Figure C.1: A subset of Bdot probes constructed during the course of the thesis work. a) Single turn 3-axis probe painted with white epoxy. b) Probe constructed by winding around 6 sides of a ceramic cube. To protect the wires from plasma damage, the probe is painted with epoxy, as in panel (c). Panel (d), and (e) are larger versions of this type of probe used to test the degree of perturbation to the plasma. Panel (d) shows the 6 mm cube and (e) shows the 15 mm probe, constructed by adding a covering to the tip shown in (d).

Fig. C.1 (a) shows a single turn probe ( $d=3.4$  mm) with sufficiently small area. The loops have an offset of 5mm with respect to each other, with the result that the measured components of  $B$  are slightly offset from each other. This can be fixed by accounting the offset in the data analysis procedure. However, this adds complexity to the analysis. In this construction it is also hard to maintain the orthogonality between the loops.

Fig. C.1 (b) shows the probe constructed by winding around 6 sides of a ceramic cube

to assist in keeping the axes orthogonal with respect to each other. Each axis has two turns, boosting the signal to noise ratio. The result is improved comparing to the case in panel (a). However, Godyak[15] suggested that a “large” obstacle like Fig. C.1 (b) will perturb local current elements and symmetry near the probe, which causes inaccuracy in the measured results.

To test Godyak’s assertion, we constructed three probes of different sizes shown in Fig. C.1. Probe in panel (c) uses a 3 mm cube, panel (d) uses a 6 mm cube and panel (e) is identical to (d) other than applying an additional 15 mm diameter obstacle on top of the probe tip. Note that after painting it with epoxy the physical dimensions for each probe increased. According to Godyak, the 3 mm probe should measure a larger current comparing to 6 mm, as the latter probe is “blocking” four times more current from passing between the loops.

A XZ data half plane with  $y=0$  is acquired for each probe in H-mode plasma. At this location, the current  $J_y = J_\phi$  and dominates over the other two directions. Fig C.2 shows the current density line-out for radial profile at  $z = 13$  cm and axial profile at  $x = -16$  cm. At 10 mTorr, results from the three probe do not appear to be very different. Plasma current is driven by an electromotive force, which drives a current in the plasma that is proportional to the conductivity around the full  $2\pi$  azimuthal circumference of the current streamlines that connect to the cross-section of the coil. Locally the current cannot flow through the probe. But as long as the probe is small compared to the plasma dimensions, the overall EMF is the same, and loop conductivity is approximately unchanged, so the global current configuration is mostly unchanged. The current finds a path to flow, in this case going around the obstacle. Consequently the signal detected by the Bdot loop stays the same.

One minor note is that in panel (c), the profile shape for 3 mm probe is slightly different comparing to the others above  $z = 11$  cm. We suspect that this is related to the non-ideal loops from 3 mm probe picking up signal due to other field directions. In fact, the 6 mm probe performs better in a test with vacuum field. Work is underway to construct a 3D

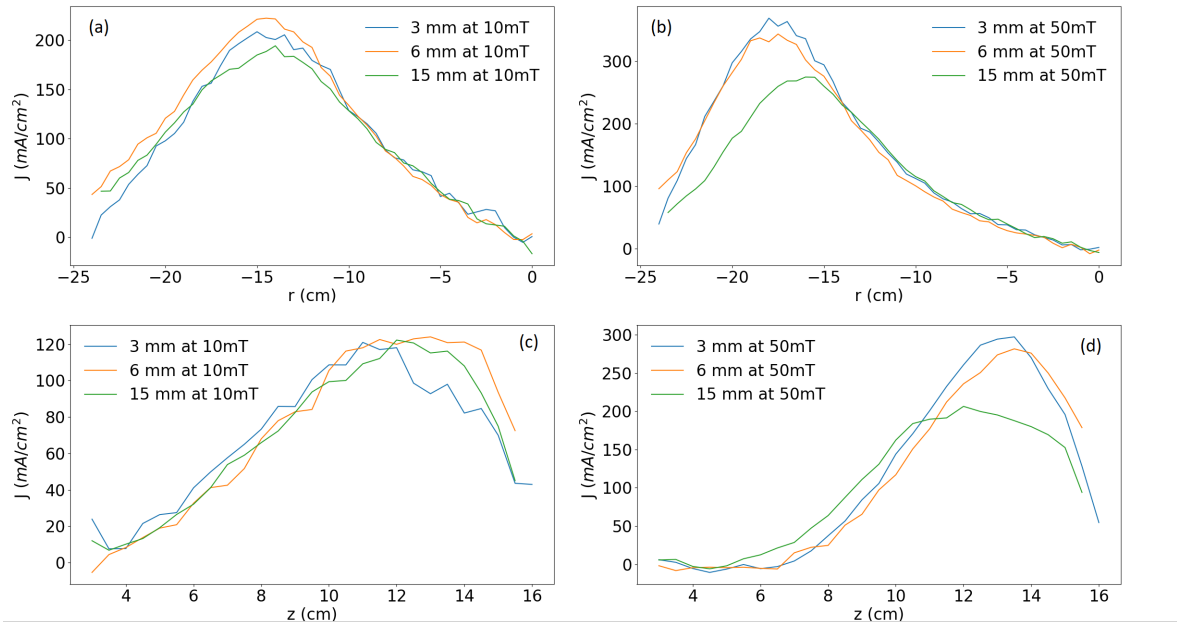


Figure C.2: Line-outs of azimuthal current density profiles at two pressures in steady state H-mode Ar plasma, illustrating the effects of different size Bdot pickups. The time corresponds to the current maximum on the rf antenna. (a) and (b) are radial profile at  $z = 13$  cm; (c) and (d) are axial profile at  $x = -16$  cm. The current profile is distorted when the coil diameter approaches the magnetic field gradient scale length; there is no apparent effect from local blocking of the current.

probe calibration scheme that will produce a 3x3 correction matrix that will multiply the measurement vector to account for this.

At 50 mTorr, the result is significantly different for the 15 mm probe case. This is likely because the probe's pick-up coils diameter approach the magnetic field gradient scale length. The probe also depletes local plasma density which changes the conductivity around the loop. A probe is geometrically "too Large" if 1) the sensor cross section is comparable to the gradient scale length, or 2) the sensor substantially changes the macroscopic characteristics of the plasma. Our conclusion is that a more important aspect of probe design is the orthogonality of individual loops, and from the above test it seems worthwhile to make a slightly bigger sensor if this can be improved.

## APPENDIX D

### Effect of feedstock gas flow rate

As shown in Fig. 2.1, the feedstock gas flows from one side of the chamber a few centimeters above the wafer. This raises the possibility of causing the observed asymmetry in steady state and pulsed plasma. To investigate the effect, a separate gas flow inlet was placed at the top center of the chamber ( $r=0, z=17$  cm).

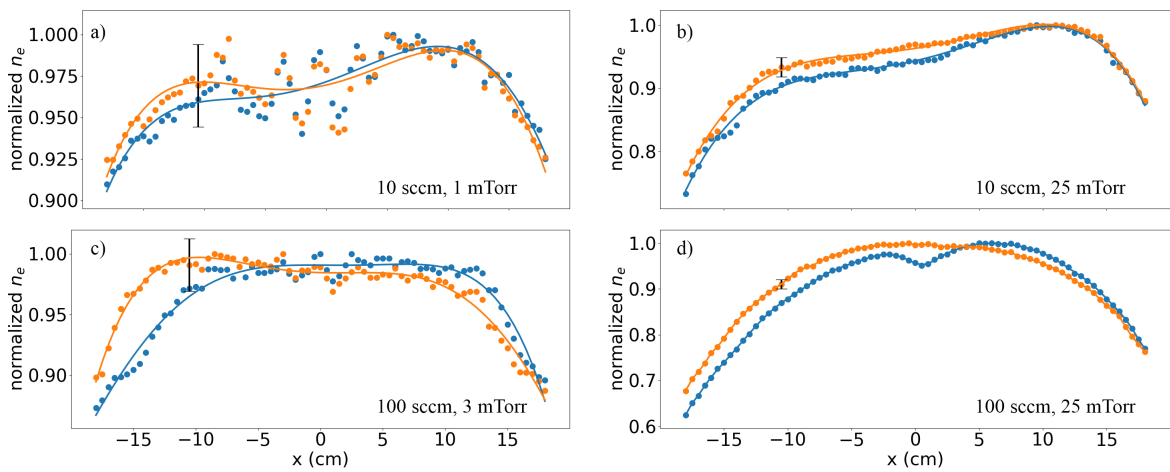


Figure D.1: Flow rate effect on density profile in Argon steady state plasma. The blue curves are acquired with the gas at the top center of the chamber. The orange curves are acquired while gas is pumping in from the left side of the machine. Panels (a) and (b) correspond to 10 sccm flow rate; (c) and (d) correspond to 100 sccm. (a) and (c) are measured at less than 3 mTorr; (b) and (d) are measured at 25 mTorr. Note that at 100 sccm, 3 mTorr is the minimum pressure the chamber is able to achieve with its pump ability. Data are acquired using the hairpin probe moved along radial chords at 12 cm above the wafer.

Fig. D.1 shows the electron density profile (normalized to its maximum) measured using a hairpin probe moved along a diameter of the chamber at  $z=12$  cm. Plasma is sustained in Argon with 500 W rf generator power. Data runs were performed with the gas flowing from the top (blue) and from the side (orange).  $n_e$  at 1 and 3 mTorr, are roughly 3 times smaller than that at 25 mTorr. Lower density causes lower signal to noise ratio for hairpin probes. Changing the location of the flow changes the profile by about 2-3%. The asymmetry in profiles are improved, but still exists.

On the other hand, changing the flow rate changes the density profile. Note that results shown in section 3.1 and 3.2 are acquired using a flow rate of 100 sccm. At a fixed flow rate, increasing the pressure makes the density profile more peaked. At a fixed pressure, increasing the flow rate also makes the profile more peaked. The density profile at 25 mTorr with 10 sccm flow rate in Fig. D.1 (b) looks similar to that at 5 mTorr (with 100 sccm) in Fig. 3.15.

Measurement results from the Bdot probe separately confirmed the profile dependence relation between increasing flow rate and increasing neutral pressure. Fig. D.2 shows the current and power density on a 2D contour for three different flow rates. From 50 to 500 sccm, the current and power deposits closer to the top. This matches the observation in Fig. 3.6 when pressure changes from 10 to 100 mTorr at a constant flow rate.

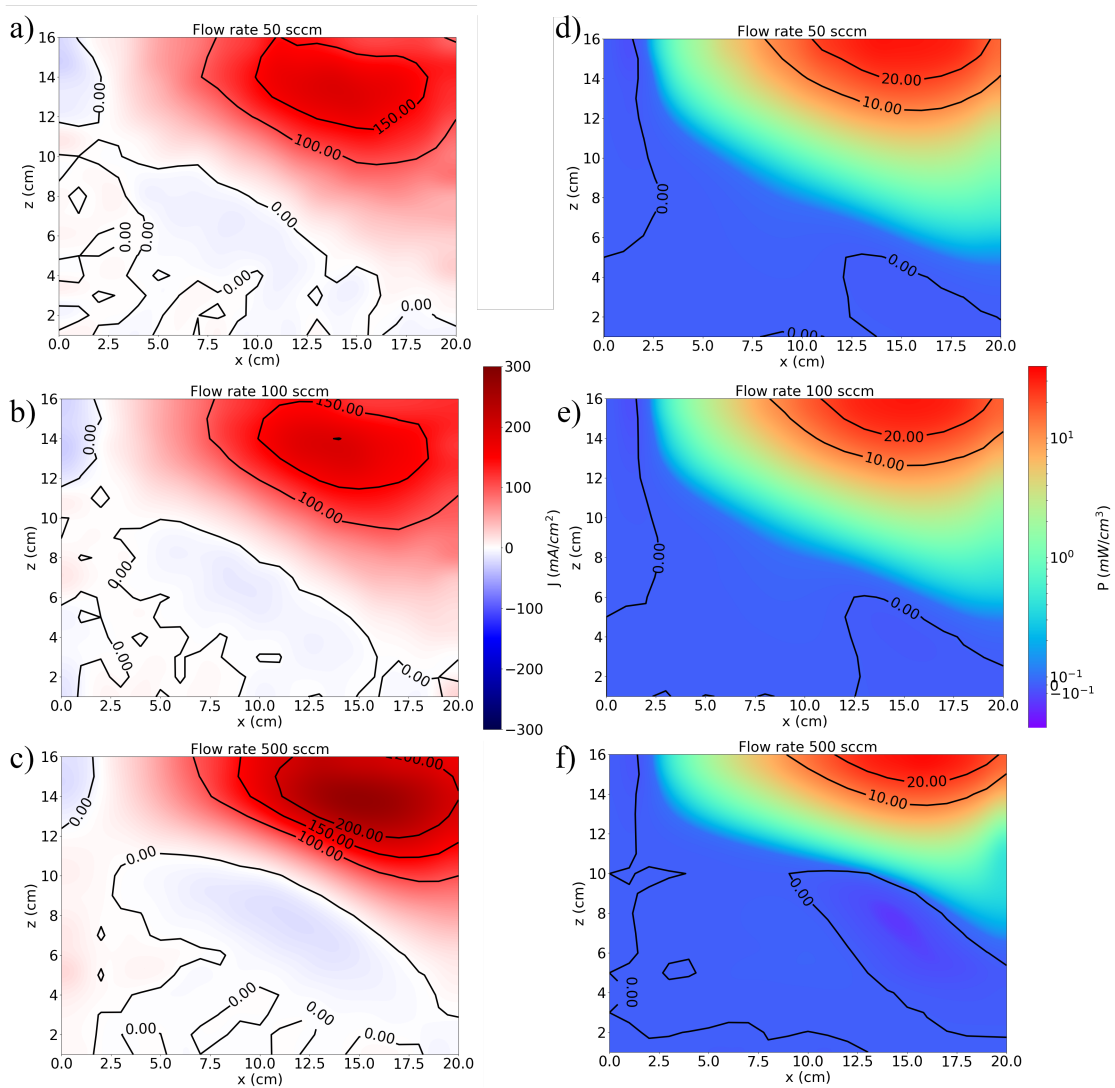


Figure D.2: Flow rate affect on (a, b, c) azimuthal current  $J_\phi$  and (d, e, f) inductive power  $P$ . Plasma operates in steady state Argon with 300 W input power. Pressure is maintained at 25 mTorr by changing the opening of the pendulum value for pump out and varying the inflow mfc.  $J_\phi$  is shown at time of maximum antenna current and  $P$  is shown for average over an rf cycle. Note that  $P$  is drawn on log scale to highlight the differences.

## REFERENCES

- [1] S. M. Irving. *Kodak Photoresist Seminar Proceedings*, book section P26. Eastman Kodak Company, 1968.
- [2] J. W. Coburn. Plasma assisted etching. *Plasma Chem. Plasma Process*, 2(1), 1982.
- [3] H. Abe, M. Yoneda, and N. Fujiwara. Developments of plasma etching technology for fabricating semiconductor devices. *Japanese Journal of Applied Physics*, 47(3):1435–1455, 2008.
- [4] S. Banna and A. Agarwal. Pulsed high density plasmas for advanced dry etching processes. *J. Vac. Sci. Technol*, A 30:040801, 2012.
- [5] J. Pelletier and A. Anders. Plasma-based ion implantation and deposition: A review of physics, technology, and applications. *IEEE Transactions on Plasma Science*, 2005.
- [6] M. A. Lieberman and A. J. Lichtenberg. *Principles of Plasma Discharges and Materials Processing*, chapter 1, pages 1–22. John Wiley & Sons, Ltd, 2005.
- [7] W. McDaniel. *Collision phenomena in ionized gases*. Wiley, 1964.
- [8] M. H. Francombe and J. L. Vossen. *Plasma Sources for Thin Film Deposition and Etching*. Elsevier Science, 2013.
- [9] M. A. Lieberman and A. J. Lichtenberg. *Principles of Plasma Discharges and Materials Processing*, chapter 7, pages 207–233. John Wiley & Sons, Ltd, 2005.
- [10] M. A. Lieberman and A. J. Lichtenberg. *Principles of Plasma Discharges and Materials Processing*, chapter 8, pages 235–283. John Wiley & Sons, Ltd, 2005.
- [11] M. A. Lieberman and A. J. Lichtenberg. *Principles of Plasma Discharges and Materials Processing*, chapter 9, pages 285–325. John Wiley & Sons, Ltd, 2005.
- [12] J. Hopwood. Review of inductively coupled plasmas for plasma processing. *Plasma Sources Sci. Technol*, 1, 1992.
- [13] P. Scheubert, U. Fantz, P. Awakowicz, and H. Paulin. Experimental and theoretical characterization of an inductively coupled plasma source. *Journal of Applied Physics*, 90(2):587–598, 2001.
- [14] T. Hori, M. D. Bowden, K. Uchino, and K. Muraoka. Measurements of electron temperature, electron density, and neutral density in a radio-frequency inductively coupled plasma. *J. Vac. Sci. Technol A*, 14, 1996.
- [15] V. A. Godyak and R. B. Piejak. Electromagnetic field structure in a weakly collisional inductively coupled plasma. *Journal of Applied Physics*, 82, 1997.

- [16] R. Piejak, V. Godyak, and B. Alexandrovich. Magnetic field distribution measurements in a low-pressure inductive discharge. *Journal of Applied Physics*, 78, 1995.
- [17] M. El-Fayoumi and I. R. Jones. Theoretical and experimental investigations of the electromagnetic field within a planar coil, inductively coupled rf plasma source. *Plasma Sources Sci. Technol*, 7, 1998.
- [18] G. A. Hebner. Spatially resolved, excited state densities and neutral and ion temperatures in inductively coupled argon plasmas. *Journal of Applied Physics*, 80(5):2624–2636, 1996.
- [19] P. Subramonium and M. J. Kushner. Two-dimensional modeling of long-term transients in inductively coupled plasmas using moderate computational parallelism. ii. ar/cl<sub>2</sub> pulsed plasmas. *Journal of Vacuum Science & Technology A: Vacuum, Surfaces, and Films*, 20(2):325–334, 2002.
- [20] M. V. Malyshev, V. M. Donnelly, J. I. Colonell, and S. Samukawa. Dynamics of pulsed-power chlorine plasmas. *Journal of Applied Physics*, 86(9):4813–4820, 1999.
- [21] M. V. Malyshev and V. M. Donnelly. Diagnostics of inductively coupled chlorine plasmas: Measurement of electron and total positive ion densities. *Journal of Applied Physics*, 90(3):1130–1137, 2001.
- [22] P. Jiang, D. J. Economou, and C. B. Shin. Effect of power modulation on radical concentration and uniformity in a single-wafer plasma reactor. *Plasma Chem. Plasma Process*, 15(3):383–396, 1995.
- [23] H. Sugai, K. Nakamura, Y. Hikosaka, and M. Nakamura. Diagnostics and control of radicals in an inductively coupled etching reactor. *Journal of Vacuum Science & Technology A: Vacuum, Surfaces, and Films*, 13(3):887–893, 1995.
- [24] S. Samukawa, K. Noguchi, J. I. Colonell, K. H. A. Bogart, M. V. Malyshev, and V. M. Donnelly. Reduction of plasma induced damage in an inductively coupled plasma using pulsed source power. *Journal of Vacuum Science & Technology B: Microelectronics and Nanometer Structures Processing, Measurement, and Phenomena*, 18(2):834–840, 2000.
- [25] P. Subramonium and M. J. Kushner. Pulsed inductively coupled plasmas as a method to recoup uniformity: Three-dimensional modeling study. *Applied Physics Letters*, 85(5):721–723, 2004.
- [26] S. Ashida, M. R. Shim, and M. A. Lieberman. Measurements of pulsed-power modulated argon plasmas in an inductively coupled plasma source. *Journal of Vacuum Science & Technology A: Vacuum, Surfaces, and Films*, 14(2):391–397, 1996.
- [27] B. Ramamurthi and D. J. Economou. Pulsed-power plasma reactors: two-dimensional electropositive discharge simulation in a gec reference cell. *Plasma Sources Sci. Technol*, 11:324, 2002.

- [28] P. Subramonium and M. J. Kushner. Two-dimensional modeling of long-term transients in inductively coupled plasmas using moderate computational parallelism. i. ar pulsed plasmas. *Journal of Vacuum Science & Technology A: Vacuum, Surfaces, and Films*, 20(2):313–324, 2002.
- [29] P. A. Miller, G. A. Hebner, G. E. Greenberg, P. D. Pochan, and B. P. Aragon. An inductively coupled plasma source for the gaseous electronics conference rf reference cell. *J. Res. Natl. Inst. Stand. Technol*, 100(4):427–439, 1995.
- [30] G. A. Hebner and C. B. Fleddermann. Characterization of pulse-modulated inductively coupled plasmas in argon and chlorine. *Journal of Applied Physics*, 82(6):2814–2821, 1997.
- [31] X. Tang and D. M. Manos. Time-resolved electrostatic probe studies of a pulsed inductively-coupled plasma. *Plasma Sources Sci. Technol*, 8:594, 1999.
- [32] F. Gao, X. Lv, Y. Zhang, and Y. Wang. Complex transients of input power and electron density in pulsed inductively coupled discharges. *Journal of Applied Physics*, 126(9), 2019.
- [33] M. Darnon, G. Cunge, and N. St J. Braithwaite. Time-resolved ion flux, electron temperature and plasma density measurements in a pulsed ar plasma using a capacitively coupled planer probe. *Plasma Sources Sci. Technol*, 23:025002, 2014.
- [34] Y. Celik, T. V. Tsankov, M. Aramaki, S. Yoshimura, D. Luggenholscher, and U. Czarnetzki. Recombination and enhanced metastable repopulation in the argon afterglow. *Phys Rev E Stat Nonlin Soft Matter Phys*, 85(5 Pt 2):056401, 2012.
- [35] A. Maresca, K. Orlov, and U. Kortshagen. Experimental study of diffusive cooling of electrons in a pulsed inductively coupled plasma. *Phys Rev E Stat Nonlin Soft Matter Phys*, 65(5 Pt 2):056405, 2002.
- [36] Y. Celik, T. V. Tsankov, M. Aramaki, S. Yoshimura, D. Luggenholscher, and U. Czarnetzki. Electron cooling in decaying low-pressure plasmas. *Phys Rev E Stat Nonlin Soft Matter Phys*, 85(4 Pt 2):046407, 2012.
- [37] F. Liu, X. Guo, and Y. Pu. Electron cooling and plasma density decay in early afterglow of low pressure argon plasmas. *Plasma Sources Science and Technology*, 24(3), 2015.
- [38] J. H. Park, D. H. Kim, Y. S. Kim, and C. W. Chung. Time-resolved spatial distribution measurements of pulse-modulated argon plasmas in an inductively coupled plasma reactor. *Plasma Sources Sci. Technol*, 26:055016, 2017.
- [39] I. S. Park, D. H. Kim, K. H. Kim, and C. W. Chung. Temporal evolution of two-dimensional electron temperature and ion flux on a substrate in a pulsed-power inductively coupled plasma. *Physics of Plasmas*, 24(5), 2017.

- [40] K. A. MacKinnon. On the origin of the electrodeless discharge. *Phil. Mag.*, 8:605, 1929.
- [41] K Chandrakar. The transition from the first to the second stage of the ring discharge. *Journal of Physics D: Applied Physics*, 11(13):1809–1813, sep 1978.
- [42] J. Amorim, H. S. Maciel, and J. P. Sudano. High-density plasma mode of an inductively coupled radio frequency discharge. *Journal of Vacuum Science & Technology B: Microelectronics and Nanometer Structures*, 9(2), 1991.
- [43] John H. Keller, John C. Forster, and Michael S. Barnes. Novel radio-frequency induction plasma processing techniques. *Journal of Vacuum Science & Technology A*, 11(5):2487–2491, 1993.
- [44] U. Kortshagen, N. D. Gibson, and J. E. Lawler. On the e–h mode transition in rf inductive discharges. *J. Phys. D: Appl. Phys.*, 29:1224–1236, 1996.
- [45] Hyo-Chang Lee. Review of inductively coupled plasmas: Nano-applications and bistable hysteresis physics. *Applied Physics Rev*, 5:011108, 2018.
- [46] J. Han, P. Pribyl, W. Gekelman, A. Paterson, S. J. Lanham, C. Qu, and M. J. Kushner. Three-dimensional measurements of plasma parameters in an inductively coupled plasma processing chamber. *Physics of Plasmas*, 26(10):103503, 2019.
- [47] J. Han, P. Pribyl, W. Gekelman, and A. Paterson. Three-dimensional measurements of fundamental plasma parameters in pulsed icp operation. *Physics of Plasmas*, 27(6):063509, 2020.
- [48] D. Leneman and W. Gekelman. A novel angular motion feedthrough. *Rev. Sci. Instrum*, 72:3473, 2001.
- [49] H. M. Mott-Smith and Irving Langmuir. The theory of collectors in gaseous discharges. *Phys. Rev.*, 28:727–763, Oct 1926.
- [50] F. F. Chen. Langmuir probe analysis for high density plasmas. *Physics of Plasmas*, 8(6):3029–3041, 2001.
- [51] F. F. Chen. Langmuir probes in RF plasma: surprising validity of OML theory. *Plasma Sources Science and Technology*, 18(3):035012, may 2009.
- [52] J. E. Allen, R. L. F. Boyd, and P. Reynolds. The collection of positive ions by a probe immersed in a plasma. *Proceedings of the Physical Society. Section B*, 70(3):297–304, mar 1957.
- [53] Ira B. Bernstein and Irving N. Rabinowitz. Theory of electrostatic probes in a low-density plasma. *The Physics of Fluids*, 2(2):112–121, 1959.
- [54] J. G. Laframboise. *Report No. 100*. PhD thesis, University of Toronto Institute of Aerospace Studies, 1966.

- [55] Isaac D. Sudit and R. Claude Woods. A study of the accuracy of various langmuir probe theories. *Journal of Applied Physics*, 76(8):4488–4498, 1994.
- [56] Noah Hershkowitz. How langmuir probes work. In Orlando Auciello and Daniel L. Flamm, editors, *Plasma Diagnostics*, pages 113 – 183. Academic Press, 1989.
- [57] Robert L. Merlino. Understanding langmuir probe current-voltage characteristics. *American Journal of Physics*, 75(12):1078–1085, 2007.
- [58] M. J. Druyvesteyn. Der niedervoltbogen. *Zeitschrift für Physik*, 64(11):781–798, 1930.
- [59] V. A. Godyak and V. I. Demidov. Probe measurements of electron-energy distribution in plasmas: what can we measure and how can we achieve reliable results. *Journal of Physics D: Applied Physics*, 44, 2011.
- [60] S. Knappmiller, S. Robertson, and Z. Sternovsky. Method to find the electron distribution function from cylindrical probe data. *Phys Rev E*, 73:066402, 2006.
- [61] F. F. Chen. Lecture notes on langmuir probe diagnostics, June 2003.
- [62] F. Liu, Z. Wang, and Y. Pu. The ac-coupling between a langmuir probe and a plasma and its effect on the plasma density measurement in the afterglow. *Journal of Physics D: Applied Physics*, 47(7), 2014.
- [63] V. A. Godyak, R. B. Piejak, and B. M. Alexandrovich. Electron energy distribution function measurements and plasma parameters in inductively coupled argon plasma. *Plasma Sources Science and Technology*, 11:525–543, 2002.
- [64] J. R. Smith, N. Hershkowitz, and P. Coakley. Inflection-point method of interpreting emissive probe characteristics. *Review of Scientific Instruments*, 50(2):210–218, 1979.
- [65] M. J. Martin, J. Bonde, W. Gekelman, and P. Pribyl. A resistively heated ceb6 emissive probe. *Review of Scientific Instruments*, 86(5):053507, 2015.
- [66] A. Marek, M. Jílek, I. Picková, P. Kudrna, M. Tichý, R. Schrittwieser, and C. Ionita. Emissive probe diagnostics in low temperature plasma – effect of space charge and variations of electron saturation current. *Contributions to Plasma Physics*, 48(5-7):491–496, 2008.
- [67] R. L. Stenzel. Microwave resonator probe for localized density measurements in weakly magnetized plasmas. *Rev. Sci. Instrum*, 47:603, 1976.
- [68] R. B Piejak, V. A. Godyak, R. Garner, and B. M. Alexandrovich. The hairpin resonator: A plasma density measuring technique revisited. *Journal of Applied Physics*, 95:3785, 2004.
- [69] B. L. Sands, N. S. Siefert, and B. N. Ganguly. Design and measurement considerations of hairpin resonator probes for determining electron number density in collisional plasmas. *Plasma Sources Science and Technology*, 16(4):716–725, 2007.

- [70] X. Fan, Y. Wug, J. Han, P. Pribyl, and T. Carter. Electron density measurement using a partially covered hairpin resonator in an inductively coupled plasma. *Review of Scientific Instruments*, 91(11):113502, 2020.
- [71] F. F. Chen. *Introduction to Plasma Physics and Controlled Fusion*. Springer International Publishing, 2015.
- [72] Y. Wug, X. Fan, S. Mackie, P. Pribyl, and T. Carter. Modified hairpin resonator for electron density measurements. 61st Annual Meeting of the APS Division of Plasma Physics, 2019.
- [73] R. L. Stenzel. Whistler wave propagation in a large magnetoplasma. *Phys. Fluids*, 19:857, 1976.
- [74] J. Hopwood, C. R. Guarnieri, S. J. Whitehair, and J. J. Cuomo. Electromagnetic fields in a radio-frequency induction plasma. *Journal of Vacuum Science & Technology A*, 11(1):147–151, 1993.
- [75] Applied Motion Products, Inc. *Host Command Reference–Q and SCL commands for servo and stepper drives*, 5 edition, 2019.
- [76] Agilent Technologies, Inc. *Agilent 33220A 20 MHz Waveform Generator User’s Guide*, 4 edition, 2007.
- [77] R. P. McEachran and A. D. Stauffer. Momentum transfer cross sections for the heavy noble gases. *The European Physical Journal D*, 68(6):153, 2014.
- [78] M. A. Lieberman and A. J. Lichtenberg. *Principles of Plasma Discharges and Materials Processing*, chapter 5, pages 133–163. John Wiley & Sons, Ltd, 2005.
- [79] S. H. Seo, J. I. Hong, K. H. Bai, and H. Y. Chang. On the heating mode transition in high-frequency inductively coupled argon discharge. *Physics of Plasmas*, 6(2):614–618, 1999.
- [80] H. C. Lee, J. K. Lee, and C. W. Chung. Evolution of the electron energy distribution and e-h mode transition in inductively coupled nitrogen plasma. *Physics of Plasmas*, 17(3), 2010.
- [81] H. C. Lee, M. H. Lee, and C. W. Chung. Effects of rf-bias power on plasma parameters in a low gas pressure inductively coupled plasma. *Applied Physics Letters*, 96(7), 2010.
- [82] M. A. Sobolewski and J. H. Kim. The effects of radio-frequency bias on electron density in an inductively coupled plasma reactor. *Journal of Applied Physics*, 102(11), 2007.
- [83] John A. Thornton. Abrupt intensity transitions in rf generated plasmas. *Journal of Applied Physics*, 40(8):3404–3406, 1969.

- [84] M. Yamashita. Fundamental characteristics of built-in high-frequency coil-type sputtering apparatus. *Journal of Vacuum Science & Technology A*, 7(2):151–158, 1989.
- [85] M.M. Turner Lieberman and M. A. Hysteresis and the e-to-h transition in radiofrequency inductive discharges. *Plasma Sources Sci. Technol*, 8:313–324, 1999.
- [86] American Institute of Physics, D.E. Gray, and A.A. Bennett. *American Institute of Physics Handbook*. McGraw-Hill handbooks. McGraw-Hill, 1957.
- [87] R. R. Arslanbekov Kudryavtsev and A. A. Modeling of nonlocal electron kinetics in a low-pressure afterglow plasma. *Phys Rev E*, 58(6):7785, 1998.
- [88] S. Seo, C. Chung, J. Hong, and H. Chang. Nonlocal electron kinetics in a planar inductive helium discharge. *Phys Rev E*, 62(5):7155, 2000.
- [89] A. Kudryavtsev V. Demidov, C. DeJoseph. Nonlocal effects in a bounded afterglow plasma with fast electrons. *IEEE Transactions on Plasma Science*, 34(3):825–833, 2006.
- [90] H. C. Lee, M. H. Lee, and C. W. Chung. Experimental observation of the transition from nonlocal to local electron kinetics in inductively coupled plasmas. *Applied Physics Letters*, 96(4), 2010.
- [91] I. D. Sudit and F. F. Chen. RF compensated probes for high-density discharges. *Plasma Sources Science and Technology*, 3(2):162–168, may 1994.